FUNCTIONALITY-DRIVEN ARCHITECTURE OF AND PHOTOVOLTAIC CONVERSION IN HIERARCHICAL TREE-LIKE SEMICONDUCTORS

by

Zhengxin Li

A dissertation submitted to the Faculty of the University of Delaware in partial fulfillment of the requirements for the degree of Doctor of Philosophy in Chemistry and Biochemistry

Summer 2019

FUNCTIONALITY-DRIVEN ARCHITECTURE OF AND PHOTOVOLTAIC CONVERSION IN HIERARCHICAL TREE-LIKE SEMICONDUCTORS

by

Zhengxin Li

Approved: _____
Brian J. Bahnson, Ph.D.
Chair of the Department of Chemistry and Biochemistry

Approved: _____
John A. Pelesko, Ph.D.
Interim Dean of the College of Arts and Sciences

Approved: _____
Douglas J. Doren, Ph.D.
Interim Vice Provost for Graduate and Professional Education

I certify that I have read this dissertation and that in my opinion it meets the academic and professional standard required by the University as a dissertation for the degree of Doctor of Philosophy.

Signed: _____

Lars Gundlach, Ph.D.
Professor in charge of dissertation

I certify that I have read this dissertation and that in my opinion it meets the academic and professional standard required by the University as a dissertation for the degree of Doctor of Philosophy.

Signed: _____

Andrew V. Teplyakov, Ph.D.
Member of dissertation committee

I certify that I have read this dissertation and that in my opinion it meets the academic and professional standard required by the University as a dissertation for the degree of Doctor of Philosophy.

Signed: _____

Karl S. Booksh, Ph.D.
Member of dissertation committee

I certify that I have read this dissertation and that in my opinion it meets the academic and professional standard required by the University as a dissertation for the degree of Doctor of Philosophy.

Signed: _____

Joshua M. O. Zide, Ph.D.
Member of dissertation committee

ACKNOWLEDGMENTS

First, I would like to express my sincere gratitude towards my advisor Dr. Lars Gundlach for all the guidance and support during my 6 years PhD program in University of Delaware. He is intelligent, generous, open-minded, patient, and professional. I always feel motivated to work with him and it is my great honor to have him guide me down the path to the doctorate degree. The work and contributions presented in this dissertation would have been impossible to finish without his help.

My recognition also goes to Dr. Andrew Teplyakov, Dr. Karl Booksh, and Dr. Joshua Zide, who offered me valuable advice and insights to my work, and kindly served as my defense committee. I would also like to thank all faculty members and fellow graduate students who have collaborated with me. Despite my passion and effort for chemistry, this work would not have been possible without the financial support from University of Delaware and the Department of Chemistry and Biochemistry, for which I am really grateful.

Finally, I would like to show my best appreciation to my parents for supporting me to study abroad. This dissertation is dedicated to them as well. I am also thankful to my husband Yingxiang Zhou for his love, encouragement and patience. My life becomes much sweeter and easier with him by my side. I must as well give special credits to my adorable corgi Coco and ragdoll Maru for their company and the joy they bring to me.

TABLE OF CONTENTS

LIST OF TABLES

LIST OF FIGURES

ABSTRACT

Vertically-aligned tree-like semiconductor structures have been studied extensively for solar cell construction and optical device fabrication. The inspiration in architecture comes from mimicking natural trees by collecting photons with branches, transferring electrons through stems, and rendering effective charge carriers separation.

ZnO is a promising n-type semiconductor with a wide band gap. It is considered as an alternative material to pristine TiO_2 since ZnO facilitates high electron binding energy, fast electron mobility, morphological diversity, etc. However, ZnO can only absorb UV light, which contributes 4% of the solar spectrum, and high electron-hole recombination rate is also challenging for the efficiency of photovoltaic conversion. These drawbacks limit its application in photocatalysis and solar energy conversion at an industrial scale. Therefore, modification, which could improve the solar energy utilization and photoelectrochemical conversion efficiency, is the key topic regarding the application of ZnO in solar cells and optical devices.

One solution is to modify ZnO with an appropriate semiconductor. CdSSe is a n-type alloy semiconductor made of CdS and CdSe. Its band gap structure can be simply tailored by adjusting the ratio between S and Se. CdSSe shows excellent light emitting performance. CuO and Cu_2O are p-type semiconductors with narrow band gaps. These three semiconductors have narrower band gaps, so this modification would lead to broader solar light absorption range and facilitate separation between electrons and holes.

In this work, design, synthesis methods, characteristics, and applications in photoelectrochemical catalysis of vertically-aligned tree-like semiconductors with ZnO nanorods as stems were demonstrated. ZnO/CdSSe nanotrees with n-n heterojunction, were prepared via chemical vapor deposition technique and unique Z-scheme electron

transfer mode was confirmed via time-correlated single photon counting technique. Next, ZnO/CuO nanotrees were synthesized via two-step hydrothermal technique. The n-p heterojunction between ZnO and CuO was verified to have high photocatalysis performance in ascorbic acid or toluene sensing. ZnO/Au/Cu_xO nanoforest was fabricated with hydrothermal-prepared ZnO, followed by gold coating and electro-deposited Cu_xO growth. With n-m-p heterojunction, ZnO/Au/Cu_xO nanoforest shows not only fast electron transport, but also broad light absorption range.

Chapter 1

INTRODUCTION

1.1 Background and Motivation

1.1.1 Hierarchical Structures in Nature

The surface of a lotus leave has highly-organized features in two levels of dimensional domains, microscale and nanoscale[1, 2]. This kind of surface, shows hierarchical manner which has a great effect on their interfaces[1, 3, 4], shown in Fig. 1.1. This hierarchical micro-/nano-scale surface texturing provides larger surface area to enhance light harvesting in photosynthesis, and self-cleaning function to make the surface clean itself by repelling water and rolling dust off.

The self cleaning property is attributed to superhydrophobicity of the surface. The multi-dimension stacking increases the surface roughness, leading to repelling water drops and a higher water contact angle[1, 2, 3]. The hierarchical structure with a water contact angle of more than 150° and contact angle hysteresis less than 10° is called superhydrophobic surface with extreme water resistance and superior self-cleaning function[1].

Roughness-induced superhydrophobicity and the mechanism of water-repelling have attracted much attention and have been investigated vastly. Wettability is the ability of a liquid phase to maintain contact with a solid surface, which is determined by a force balance between adhesive and cohesive forces. At least two states in gas, liquid, and solid are involved in wetting behaviors. Adhesive forces occur between liquid and solid, causing the liquid to spread on the surface while cohesive forces are defined in the liquid phase which makes the drop to ball up without contacting the surface. The angle at the balance between adhesive and cohesive forces is called the contact angle.

The contact angle is defined as the angle between the liquid–gas interface and the solid-liquid interface. Because contact angle is feasible to measure, instead of adhesive and cohesive forces, it is often used to determine the wettability of a surface. In general, the surface with a contact angle less than 90° is indicated favorable wetting, or termed hydrophilic. Greater than 90° shows unfavorable wetting, or termed hydrophobic[5]. Superhydrophilicity means the contact angle is almost zero and superhydrophobicity means almost no contact between the liquid drop and the surface.[6, 7]

Wenzel model and Cassie-Baxter model are the most popular wetting models[5], shown in Figure 1.2[2]. Wenzel model is also called homogeneous model. This is because the wetting liquid is allowed to penetrate grooves on the surface and the roughness grooves are completely occupied by the wetting liquid. So in Wenzel model, the surface can be wetted easily. Cassie-Baxter composite, which is called heterogeneous model, stands for the wetting mode when air pockets are trapped in grooves to prevent the liquid from immersing the roughness grooves. These two models may switch during surface modifications or both may exist on one uneven surface. Both models can provide hydrophobic surface but only the latter has the potential to be superhydrophobic surface[2].

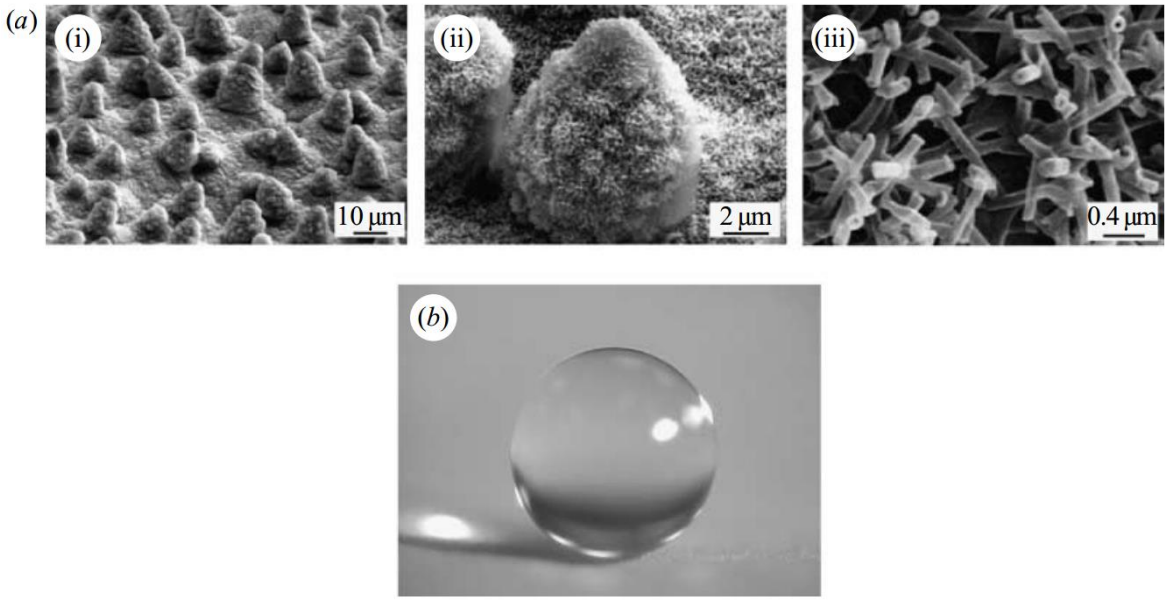

Figure 1.1: SEM images of lotus leaf surface(a) and a water droplet sitting on a lotus leaf(b). Reprinted with permission from [1].

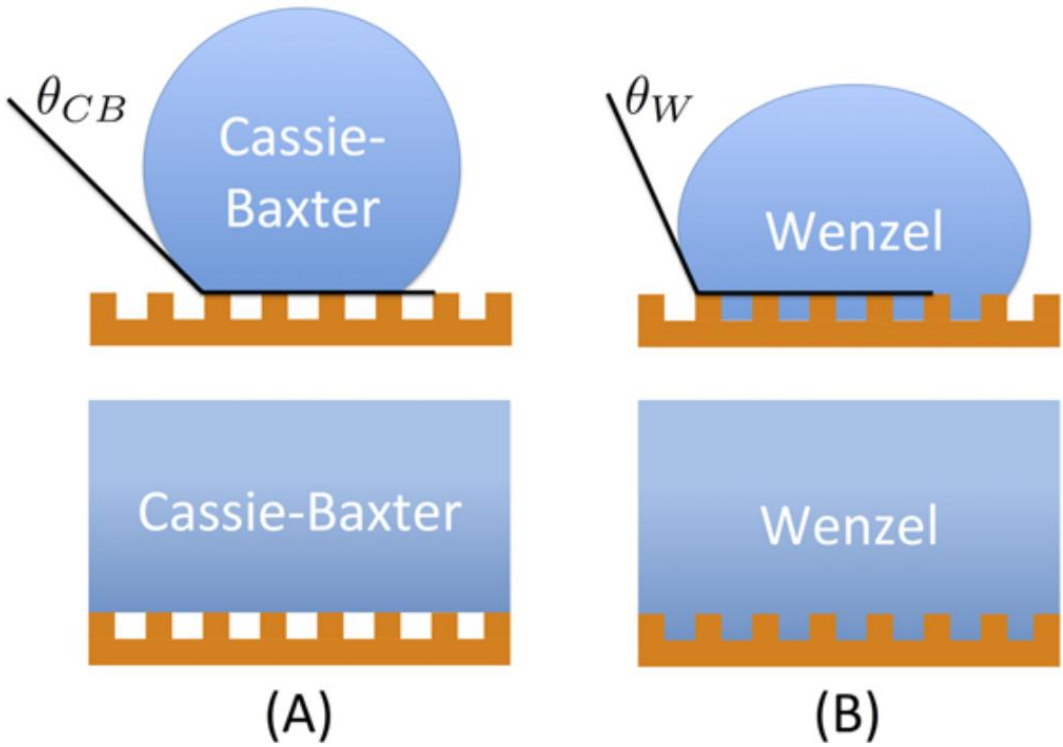

Figure 1.2: Cartoons of the Cassie-Baxter state (A) in a drop (top) and a bulk liquid (bottom). and Same as for the Wenzel state (B) in a drop (top) and a bulk liquid (bottom). Reprinted with permission from [2].

1.1.2 Hierarchical Structures of Semiconductors

To mimic this marvelous design of tree-like structures, artificial hierarchical materials have recently attracted extensive interests [8, 9]. Among them, semiconductors are the most attractive building blocks since they have the ability to absorb and convert solar energy to electricity or other energy forms. The pioneering synthesis of three-dimensional hierarchical semiconductors was reported by Yang et al[10]. In Yang et al.'s article, three medal oxides, porous silica, niobia, and titania, were synthesized in multiple length scales by a combination of micromolding, polystyrene sphere templating, and cooperative assembly. After this, considerable multifunctional semiconductor materials were found to be promising candidates for hierarchical architecture, including metal oxides[11, 12, 13, 14], sulfides[15, 16, 17],III-V semiconductors[18, 19], etc.

Hierarchical semiconductors are referred to the nanostructured semiconductors having at least two dimensional levels of identical or different semiconductors. With proper design and engineering, the morphology of hierarchical structures of semiconductors would have increased surface area[20, 21], and boosted light harvesting[22, 23], and self-cleaning property[24], compared to random nanoparticles and nanorods. Furthermore, the proper junction formation could enhance electron diffusion[25, 26, 22], and accelerate surface reaction[27, 28].

Notably, self-cleaning function is critical for solar cells and optical devices in real environments. Dust accumulation or water spill-induced contamination on device surfaces can affect the power efficiency and performance terribly, so to overcome the problem, integrating a superhydrophobic surface with self-cleaning function is desirable. These outstanding features make hierarchical semiconductors promising materials for heterogeneous photocatalysis and photovoltaic conversion[22, 29, 30].

1.1.3 ZnO-based Hierarchical Structures

Devices based on eco-friendly semiconductors in hierarchical structure have been investigated deeply to enhance the device performance without triggering potential pollution by leftover of retired devices[31]. ZnO is an important II-VI semiconductor with a band gap of 3.3 eV[32], featuring high electron mobility, large exciton binding energy, good stability, biological compatibility, and high abundance[32, 33, 34]. This is a non-toxic "green" material with low cost compared to heavy metal-based semiconductors. Therefore, ZnO is considered a promising material for optical devices, solar cells, and photocatalysts. Compared to TiO_2, ZnO has 10 to 100 times higher electron mobility, lower electrical resistance and higher electron-transfer efficiency.[34] In addition, ZnO can be prepared in a wide range of nanostructured morphologies like nanowires, [35, 36] nanorods, [37] nanohelices, [38] nanocones, [39] and nanotetrapods [40]. The different morphologies can be used as platforms for modifications with functional materials for tailoring the properties of the resulting nanocomposite [41].

The high performance in photocatalysis of ZnO is partly attributed to its electron configuration. Zn has completely filled 3d orbitals and filled 4s orbitals so Zn^{2+} in ZnO has electron configuration of [Ar]$3d^{10}$. Under UV illumination, electrons in the valence band (VB) of ZnO are excited to the conduction band (CB) leaving holes. In this case, the VB of ZnO is contributed by d-states only and the conduction band contributed by s–p hybridized orbitals. Since the dissimilar parity of orbital natures between CB and VB, the transition of electrons from CB to VB is more difficult so the recombination probability would be reduced and the lifetime of carriers can be increased[42, 43, 44, 45]. Longer lifetime of carriers ensures that the excitons can diffuse to the surface and initiate photo-induced reaction. Most transition metal oxide semiconductors have partially filled 3d orbitals, resulting in relatively high recombination rate. ZnO is naturally n-type due to native donor defects such as oxygen vacancies and interstitial zinc atoms in the growth process. Although artificial p-type doping is feasible to obtain as well[46], self compensation effect by native defects is a bottleneck and p-type ZnO is not long-lasting as n-type ZnO[47]. Hence, only natural n-type ZnO was explored in this dissertation.

However, the drawbacks of ZnO cannot be neglected. It does not absorb visible light, which only takes 4% of the solar energy. Furthermore, like other semiconductors, charge carrier recombination is still challenging in bare ZnO materials, which gives rise to low photovoltaic efficiency and poor photocatalytic ability. To broaden the absorption wavelength range to utilize the majority visible lights of solar energy, a variety of materials absorbing visible light have been used as sensitizers to compensate ZnO for solar energy applications, such as narrow-gap semiconductors[48], dye molecules[49], and photosensitive polymers[50].

Among these modifications, narrow-gap semiconductors are of great interest. This is because they can not only expand light absorption spectrum, but also form different types of heterojunctions with ZnO that can be exploited to modify the charge separation process. Another reason is, compared to organic molecules, narrow-gap

semiconductors are stable and durable in real environment, easy to form desired morphologies, heat-resistant and suitable for devices that need to withstand high temperature.

To achieve this objective, a number of narrow-band-gap semiconductors have been reported that can help ZnO make progress. Broadly speaking, the narrow-band-gap engineering with ZnO can be classified into two main categories according the the doping types: n-n heterojunction such as CdS and CdSe[51, 52, 53];p-n heterojunction such as CuO and Cu_2O[54, 13, 55, 12].

The synthesis of two-dimensional hierarchical ZnO-based structures basically requires two steps of processing. The first step is the development of ZnO nanostructures as the base material. ZnO can be synthesized differing in morphology, size and spatial structure with variable techniques. Chemical or physical vapor deposition[56, 57, 58], wet chemical route[59, 60, 61], hydrothermal synthesis[62, 63, 64], the sol-gel process[65, 66, 67], etc have been reported. Subsequently, the deposition of the nanoscale secondary materials should be attached to ZnO nanowires. To ensure the successful electron exchange between two semiconductors, the interface quality is rather important. Thus, the design ensuring efficient electron transfer pattern is the key question that should be addressed carefully for hierarchical structure construction.

1.2 Outline of Dissertation

The thesis is organized in the following order: Chapter 1 introduces the background of hierarchical semiconductors and the basic properties of ZnO.

Chapter 2 focuses on the experimental methods. It discusses chemicals and instruments used in this dissertation, and techniques of synthesis like chemical vapor deposition (CVD), hydrothermal and electrochemical deposition and characterization by microscopy, spectroscopy and electrochemistry.

Chapter 3 presents the background and motivation for fabrication of ZnO/CdSSe

nanotrees and their characterization. Furthermore, time-correlated single photon counting technique is utilized to determine the Z-scheme electron transfer across n-n heterojunction between ZnO and CdSSe. This chapter is reprinted with permission from [68].

Chapter 4 displays synthesis mechanism of ZnO/CuO nanotrees and facilitates a discussion of its photoelectrochemical properties and applications in sensing electrochemically active ascorbic acid and electrochemically inert toluene in aqueous and acetonitrile solutions, respectively. This chapter is reprinted with permission from [69].

Chapter 5 shows superhydrophobicity of ZnO/Au/Cu_xO nanotrees and an investigation of the role that Au plays in the ZnO/Cu_xO heterojunction as well as the mechanism of carrier consumption in water solution under xenon illumination.

Chapter 6 compares ZnO-based heterojunctions in different types of nanotrees and concludes with discussing the key concern in synthesis of hierarchical structures of semiconductor that will guide future processing of hierarchical architecture of semiconductor and the dynamics of carrier transfer in n-n, n-p, and n-m-p heterojunctions.

Chapter 2

EXPERIMENTAL SECTION

2.1 Synthesis of ZnO Vertically-aligned Nanowires

2.1.1 Chemical Vapor Deposition via Thermal Carbon Reaction

ZnO nanopowder and activated carbon were purchased from Sigma-Aldrich, USA and Alpha, USA, respectively. 10-nm-thick gold was coated on sapphire slides using a Cressington 308 coating system.

ZnO nanopowder and activated carbon were mixed with wt%:wt% of 50:50 in ethanol and sonicated in water bath for 30 minutes, then dried at 80°C. The ZnO carbon (ZnO/C) mixture was placed in an alumina boat. Gold-coated sapphire plates were placed on the top of the alumina boat with the gold-coated side facing down. The alumina boat was placed in the center of the quartz tube in a horizontal tube furnace (Lindberg Blue M). The thermal carbon reaction was taken at 900 °C with a slope of 80 °C/min under argon purging with flow rate of 40 sccm for 2 hours and open to the air for the next 3 hours.

2.1.2 Innovative Hydrothermal Technique

2.1.3 Chemicals

Zinc acetate dihydrate ($Zn(CH_3COO)_2 \cdot 2H_2O$, 98.0% -101.0%, Alfa Asear) and copper acetate monohydrate ($Cu(CH_3COO)_2 \cdot H_2O$, 98+%, Acros Organics) were used as ZnO and CuO seeding precursors, respectively. Zinc nitrate hexahydrate ($Zn(NO_3)_2 \cdot 6H_2O$, 99+%, Fisher) and hexamethylenetetramine (HTMA, $(CH_2)_6N_4$, 99+%, Alfa Asear) were used for ZnO hydrothermal growth.

For the formation of the ZnO seed layer, a 5 mM solution of $Zn(CH_3COO)_2$ in ethanol was prepared and sonicated for 5 min. ITO coated glass slides ($2 \times 1 \times 0.1$ cm)

were cleaned and sonicated in ethanol for 5 min. Preparation of the ZnO seed layer involved five cycles of the following procedure: The clean ITO glass was immersed into 10 mL of 5 mM $Zn(CH_3COO)_2$ for 3 s, rinsed with ethanol, and dried under N_2 at room temperature. Subsequently, the seeded sample was annealed in a furnace at 350 °C for 45 min in the air. Two cycles of this procedure were conducted to produce a uniform seed layer on the surface of the ITO slide.

For hydrothermal growth of ZnO nanowires, a 5 mM solution of $Zn(NO_3)_2$ and HTMA in water was prepared with a mole ratio of 1:1. A ZnO-seeded ITO glass was placed on a silica ring with the seed layer facing down in a Teflon liner. The Teflon liner was placed in an autoclave and filled with 10 mL of the $Zn(NO_3)_2$/HTMA solution. Hydrothermal growth was performed in the sealed autoclave at 90 °C. The autoclave was removed after 5 h. The growth procedure was repeated three times to achieve the desired length of the nanowires.

In conventional hydrothermal growth experiments, the substrate was placed with seed face up and submerged in precursor of concentration 20 to 100 mM[70, 71, 72, 73, 74, 75]. Compared to the conventional technique, this work consists of two innovations: First, silica ring support was utilized for placing the seed face down so that nanowires grow vertically without unexpected accumulation. And second, three cycles of less concentrated precursor were used instead of one cycle with normal concentration to grow thin and long wires.

2.2 Chemical Vapor Deposition of CdSSe Alloy Semiconductor

CdS and CdSe powder purchased from Sigma-Aldrich, USA, were mixed with a wt%:wt% of 50:50 and placed in an alumina boat. The alumina boat was placed in the center of the quartz tube, and the ZnO nanowire coated sapphire slide was placed 10 cm downstream from the CdSSe boat. The reaction temperature was 820 °C with a slope of 80 °C/min and an argon flow rate of 40 sccm.

2.3 Hydrothermal Technique of CuO Deposition

2.3.1 Chemicals

Copper acetate monohydrate ($Cu(CH_3COO)_2 \cdot H_2O$, 98+%, Acros Organics) was used as CuO seeding precursor. Copper nitrate trihydrate ($Cu(NO_3)_2 \cdot 3H_2O$, 99%, ACROS Organics) and hexamethylenetetramine (HTMA, $(CH_2)_6N_4$, 99+%, Alfa Asear) were used for CuO hydrothermal growth. In terms of CuO seed layer on ZnO nanowires, the as-prepared ZnO substrate was wetted in 10 mL of 5 mM $Cu(CH_3COOH)_2$ solution for 10 s, rinsed with ethanol, and dried with N_2 at room temperature. This procedure was repeated 4 times followed by annealing in a furnace at 250 °C for 2.5 h in the air.

The precursor for CuO hydrothermal growth is a 2 mM solution of $Cu(NO_3)_2$ and HTMA in water prepared with a mole ratio of 1:1. The CuO-seeded ZnO slide was positioned on the silica support ring with the seeded face down inside a Teflon liner. The liner was placed in an autoclave and filled with the prepared precursor solution. The sealed autoclave was heated at 90 °C for 5 h.

Finally, the sample was annealed for 30 min at 250 °C exposed to the air for converting remaining $Cu(OH)_2$ into CuO[76].

2.4 Cyclic Voltammetric Electrodeposition of Cu_xO

A 5nm-thick layer of gold was coated on as-prepared ZnO substrate by a dual e-beam evaporator, and then the substrate turned to dark blue. Afterward, Cu_xO was electrodeposited via cyclic voltammetric (CV) stripping from 0.4 V to -0.7 V with scan speed of 50 mV/s for 4 cycles in the solution of 0.04 M $CuSO_4$ and 0.3 M lactic acid with pH of 11 at 50 °C. Unlike redish color in bulk Cu_2O, the substrate showed yellowish color, which is due to Cu_xO in nanoscale[77]. As long as the ZnO/Au/Cu_xO nanoforest is formed, water drops cannot expand on the surface of the substrate. The control sample of pure Cu_2O was deposited at -0.5 V for 3 min. The control sample of Cu_xO was deposited with CV from from 0.4 V to -0.7 V with scan speed of 50 mV/s for

4 cycles, and the control sample of ZnO/Cu_xO was deposited with the same technique but the pH was kept at 9 to protect ZnO from dissolving in alkaline.

2.5 Morphology and Composition Characterization

The morphology of the hierarchical structures was characterized by ZEISS Auriga 60 and Hitachi S5700 scanning electron microscope (SEM) at 20 kV and 25 μA with energy dispersive X-Ray spectroscopy (EDS) detector. The crystal structure and composition were measured with Rigaku MiniFlex powder diffractometer using filtered Cu Kα radiation (λ=1.5418 Å), which was operated in a glove-box and Bruker D8 X-Ray powder diffractometer (XRD) using filtered Cu Kα1 radiation coupled with a LynxEye position sensitive detector, and with a Thermo Fisher K-Alpha+X-ray photoelectron spectrometer (XPS). Contact angle measurements were taken with VCA optima, AST Products, Inc.

2.6 Measurements of Optical Properties

Diffuse Reflectance Spectroscopy (DRS) measurements were taken with a Cary 500 Scan UV-Vis spectrophotometer, Varian. UV-Vis transmission measurements were carried out with a photon control fiber probe spectrometer (SPM-002). Nanotrees were scratched and suspended in ethanol, then dropcast onto a glass slide. Nanotree suspension slides were imaged using an Olympus IX70 fluorescence microscope.

A 10kHz 800-nm Ti:sapphire laser (Coherent Mantis, Coherent Legend-Elite) with a full width half maximum (FWHM) of 35 fs was used in transient absorption measurements. 440-nm excitation pulse was generated by a lab-built two-stage non-collinear parametric amplifier (NOPA) via second harmonic generation (SHG) in a 0.2 mm BBO crystal. A pair of BK7 prisms were used to compensate the chirp of the pump beam before the SHG process. A chopper wheel was placed in the pump beam path to block every other pump pulse. The probe beam from 450 nm to 720 nm was generated by focusing 0.1 μJ of the laser on a 3 mm thick sapphire window. A pair of chirped mirrors were used to compress the probe beam. Both pump and probe were focused

on the sample and a stage was placed on the path of the pump beam for time delay. The sample was placed in a vacuum chamber with 1.379×10^{-5} mbar. The Gaussian fit to the cross-correlation signal of the pump and probe gives 50 fs as the FWHM. The power of the pump pulse measured at the sample was 160 nJ.

Photoluminescence (PL) and time-correlated single photon counting (TCSPC) measurements at room temperature were carried out using SHG producing a train of 50 fs pulses centered at 400 nm with an output power of 1.76 mW, by employing a NOPA to generate 580 nm excitation, or using the SHG of the NOPA to generate 290 nm. An ID-100 single photon detection module (ID Quantique) fitted with FGB37 (BG40) colored glass and 550 or 600 nm interference bandpass filter was used for time-resolved measurements. PL spectra were taken with a SPM-002 fiber probe spectrometer with FGB37 (BG40) colored glass filter for excitation and GG (> 495 nm) glass filter for emission.

2.7 Measurements of Electrochemical and Photoelectrochemical Properties

2.7.1 Chemicals

Potassium Chloride (KCl, 99%, Alfa Aesar) and tetrabutylammonium hexafluorophosphate ($BuNF_4$, 99%, Sigma-Aldrich) were used as supporting electrolytes for aqueous solutions and acetonitrile (MeCN) solutions, respectively. Potassium ferricynide(III) ($K_3Fe(CN)_6$, 99+%, Acros Organics), potassium hexacynanoferrate(II) trihydrate ($K_4Fe(CN)_6$, 98+%, Alfa Asear), ferrocene (99%, Alfa Aesar), L-(+)-ascorbic acid (99+%, Alfa Aesar), toluene (99.0%, Sigma-Aldrich) were used to characterize the photo-electrochemical performance of the electrodes. Indium tin oxide (ITO) coated glass slides were purchased from Yingkou Opv Tech New Energy Co. Ltd.

2.7.2 Measurements

All electrochemical and photoelectrochemical measurements were performed using a Biologic SP-300 potentiostat with an electrochemical impedance spectroscopy

(EIS) module. The as-prepared nanotree substrate was used as the working electrode, a platinum wire and an Ag/AgCl (sat. KCl) electrode were used as the counter electrode and the reference electrode, respectively. 0.1 M KCl and 0.1 M $BuNF_4$ were employed as supporting electrolytes in aqueous solutions and in acetonitrile solutions, respectively. Photoelectrochemical measurements were taken under illumination by a 300 W xenon arc solar stimulator or 8-Watt 365 nm UV light source (Thermo Scientific 3UV-38 3UV) that resulted in a fluence of 1020 $\mu W/cm^2$.

Chapter 3

EFFICIENT Z-SCHEME CHARGE SEPARATION IN NOVEL VERTICALLY-ALIGNED ZNO/CDSSE NANOTREES

3.1 Introduction

CdS and CdSe are common narrow-band-gap semiconductors. CdS has a wider band gap ($\approx$ 2.43 eV) compared to CdSe ($\approx$ 1.76 eV). CdSe has larger lattice mismatch with ZnO so the larger barrier height leads to lower electron injection efficiency in CdSe/ZnO heterostructures[78]. Ternary alloys of CdS and CdSe allow the band gap to be adjusted by changing the ratio[79]. It has been shown that the combination of ZnO and CdSSe can improve the efficiency of solar energy conversion in ZnO/CdSSe composites[80, 81].

The definition of exciton binding energy is similar to that of electron binding energy, which is the energy that is required to remove an exciton from semiconductors[82]. It varies depending on different energy bands from a few meV to 100 meV[83]. If this value of the semiconductor is smaller than 25.7 meV that is k_BT value with k_B as Boltzmann constant and T as room temperature, 300 K, excitons will be dissociated in the air and no fluorescence can be generated at room temperature. Exciton binding energies of ZnO, CdS, and CdSe are about 60 meV[82, 83], 28 meV[84, 85], and 10-100 meV [86, 87], respectively, so they may have the ability in photoluminescence at room temperature.

Vertically aligned structures of ZnO nanowires can give rise to more efficient electron transport when compared to spherical nanoparticles[22]. Accordingly, a combination of CdSSe branches and vertically aligned ZnO nanowires can increase visible light absorption and charge transport efficiency at the same time[81, 22]. Such heterostructures are potential materials for photovoltaic applications, and other optical

devices. However, so far vertically-aligned tree-like nanostructure with CdSSe branches attached to a ZnO stem, comparable to those presented in this paper, have not been reported.

The efficiency of the so-called Z-scheme mechanism of light conversion in natural photosynthetic systems triggered many attempts to mimic its general features in artificial systems. Z-scheme charge transfer in semiconductors means the electrons excited transfer to the VB of other semiconductors rather than recombine with their own holes [88, 89]. For this purpose, numerous semiconductor systems, most of them a combination of nanomaterials, have been presented in recent years [90, 91, 88, 89]. The tree-like structures comprising CdSSe light absorbing branches and ZnO stems present in this paper show promising properties for efficient Z-scheme charge transfer.

In this chapter, we applied a new method to prepare 30 μm long ZnO nanowire arrays *via* solvent-free one-step chemical vapor deposition (CVD) from ZnO nanopowder and activated carbon that is based on a method first published by Zhu et al.[92] The nanotrees were synthesized by depositing CdSSe branches on ZnO nanowires *via* a second CVD step. SEM, EDS, and XRD were used to verify the morphology, composition and crystal structures of ZnO/CdSSe nanotrees. DRS, fluorescence microscopy, and time-resolved photoluminescence measurements were employed to investigate optical properties and electron transfer mechanism.

3.2 Synthesis of ZnO/CdSSe Nanotrees

The procedure for ZnO/CdSSe nanotree preparation is illustrated in Figure 3.1. The growth mechanism is a catalytic vapor-liquid-solid (VLS) process combined with a non-catalytic vapor-solid (VS) process where ZnO was reduced to Zn by activated carbon and alloyed with gold on a sapphire substrate in argon atmosphere. Short and thick ZnO nanorods were grown underneath the catalyst in the first step. Subsequently, the sample was exposed to air and long ZnO wires grew on top of the short ZnO seeds in VS growth. Details of this VLS-VS mechanism have been discussed previously[92, 93]. CdSSe branches were grown on the ZnO nanowire without an additional catalyst.

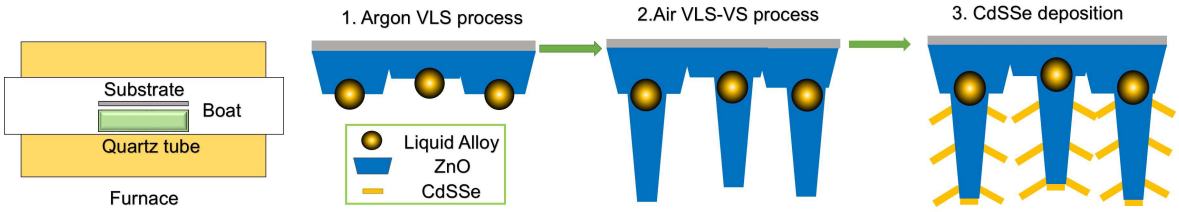

Figure 3.1: Schematic representation of ZnO/CdSSe nanotree preparation *via* two-step CVD.

In literature, the vertical alignment of ZnO nanowires is attributed to two facts, the guidance of sapphire crystal and the formation of ZnO/Au alloy droplets[92, 93]. To determine which is the primary reason, ZnO/CdSSe nanotrees were synthesized in addition on silicon, fused silica, and FTO substrates. All substrates resulted in similar structures under identical preparation conditions shown in Fig 3.2. This shows that the nanotrees can grow on different optical or electrical platforms regardless of the material type of substrates.

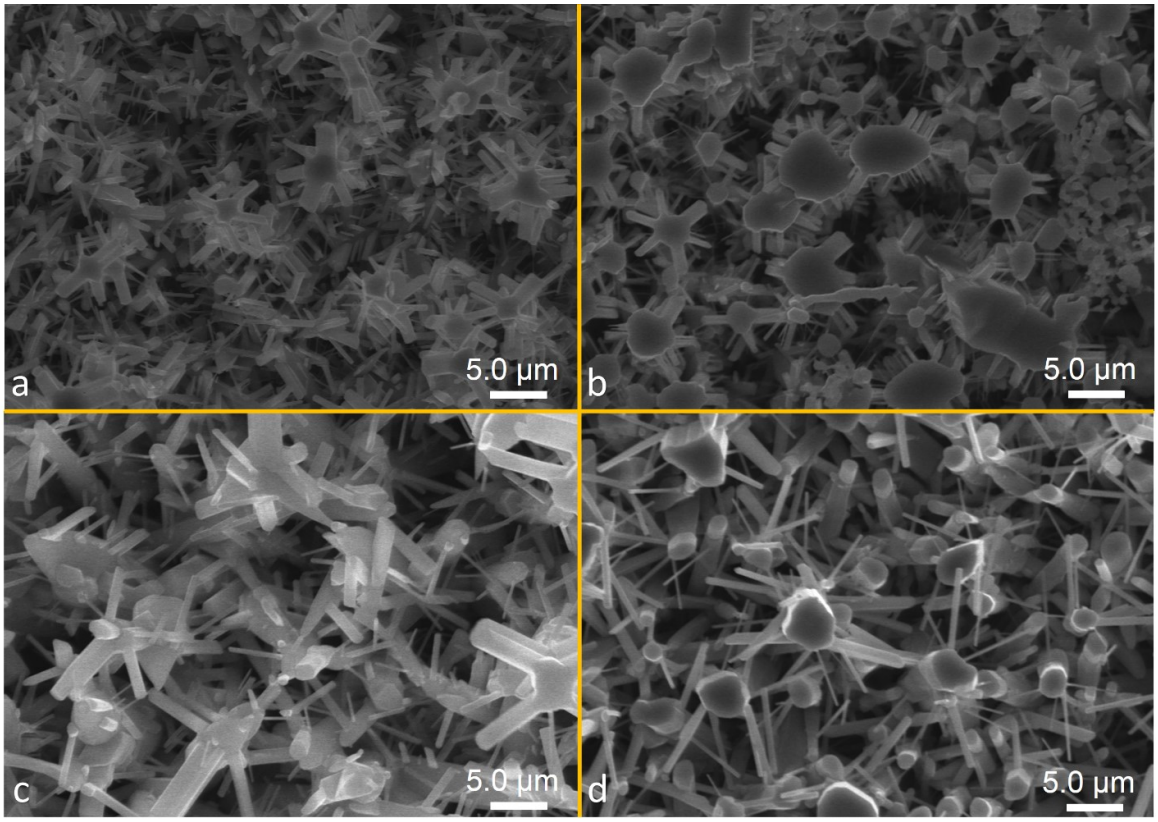

Figure 3.2: SEM images of ZnO/CdSSe nanotrees grown on Sapphire (a), Silicon (b), FTO (c), and Silica (d).

For reference measurements, bare ZnO samples were prepared without addition of CdSSe branches. Reference measurements on pure CdSSe wires were performed on ZnO free areas of the substrate, ensuring identical growth conditions for wires and branches.

3.3 Morphology and Crystallographic Characterization of ZnO/CdSSe Nanotrees

Figure 3.3 shows the SEM images of ZnO nanowires and ZnO/CdSSe nanotrees. From Fig. 3.3 (a) and Figure 3.4, the length and diameter of ZnO nanowires were estimated to be around 30 μm and 500 nm, respectively. Tree-like nanostructures are shown in Figure 3.3 (b), and (c). EDS confirmed that the branches contain S and

Se with a ratio of around 0.53:0.47 atomic % shown in Figure 3.5). The same ratio was extracted from thewoz luminescence spectra as discussed below. EDS element scans from three different parts of the NT in Figure 3.3 (c) are shown in Figures 3.3 (d),(e),and (f) together with a line scan element mapping in 3.3 (g), and (h). The element scans show that branches and caps contained Cd, S, and Se while the stem only showed contributions from Zn and O. The Zn and O signal from the cap and branch branch region are due to background from the underlying material. Intermixing of Zn into CdSSe is expected to be negligible as discussed in the following paragraphs.

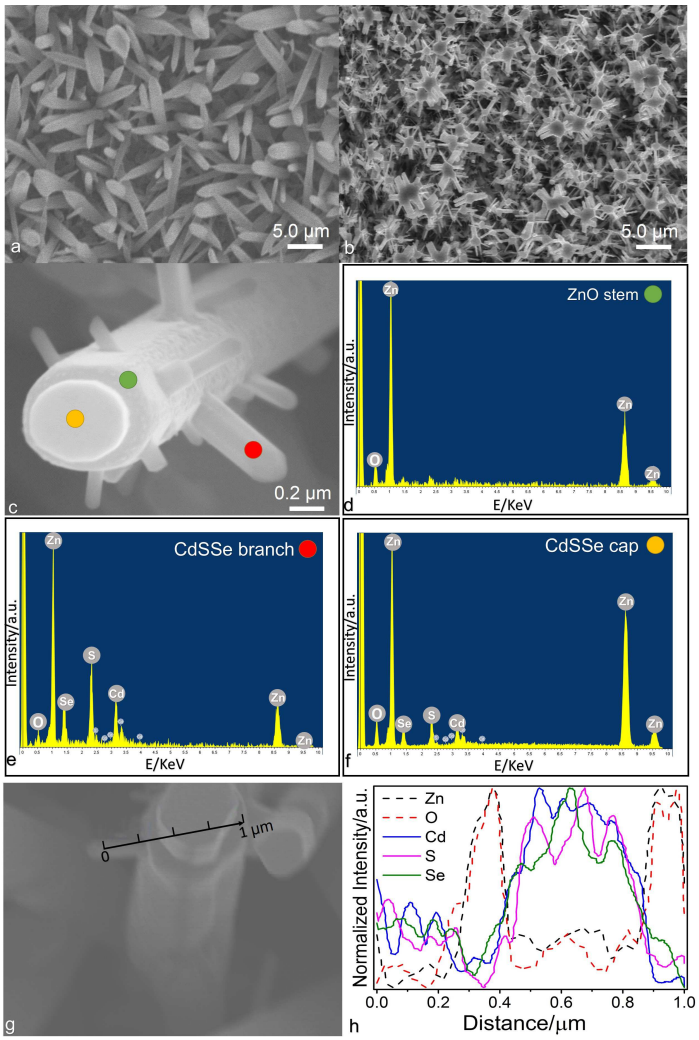

Figure 3.3: (a) SEM image of ZnO nanowires prepared *via* CVD. (b) and (c) SEM images of ZnO/CdSSe nanotrees prepared *via* CVD. EDS spectra of ZnO stem, CdSSe cap, and CdSSe branch of ZnO/CdSSe nanotrees are shown in (d), (e), and (f), respectively. (h) shows an element line scan along the line shown in (g).

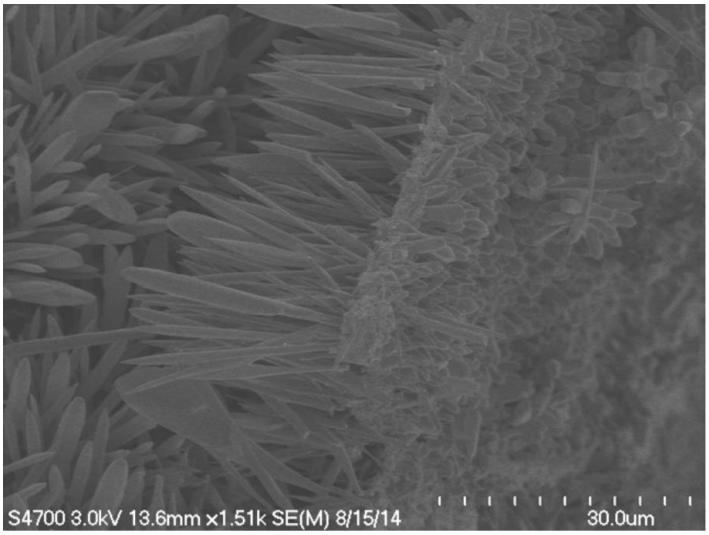

Figure 3.4: Tilted SEM image of 30-μm-long ZnO nanowires.

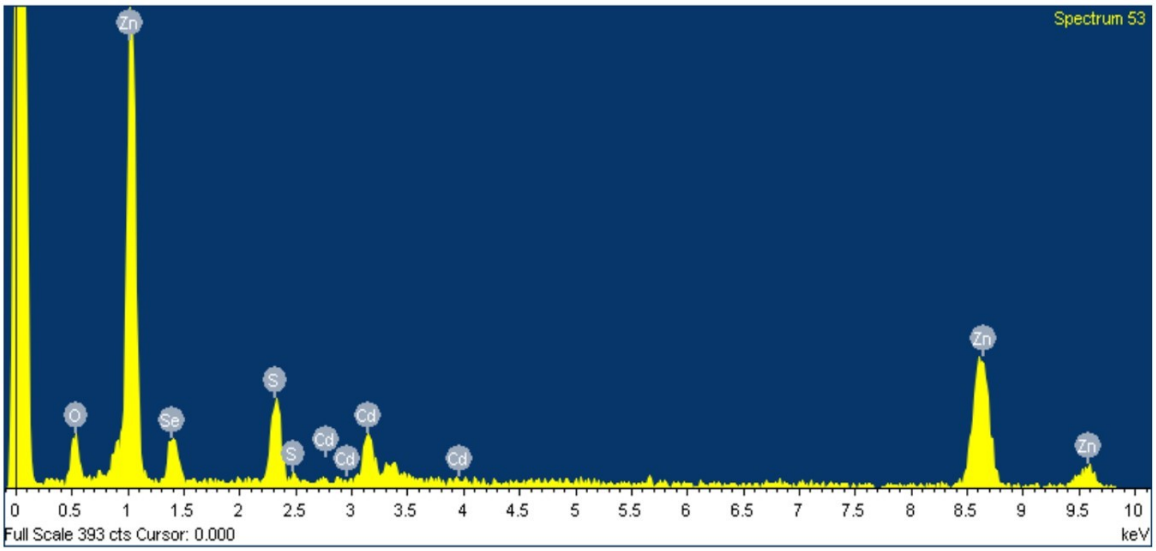

Figure 3.5: EDS element spectra of the whole slide of ZnO/CdSSe nanotrees.

Table 3.1: Average Element Composition Percentage of ZnO/CdSSe Nanotrees

Element	Weight%	Atomic%
O K	22.01	53.96
S K	3.70	4.52
Zn K	57.36	34.41
Se K	8.12	4.03
Cd L	8.81	3.08

XRD patterns of ZnO/CdSSe nanotrees with the signal from the sapphire substrate subtracted are shown in Figure 3.6. Bare ZnO nanowires show the typical wurtzite structure, with peaks at (100), (002), (101), and (102). The strong and narrow peak at (002) that refers to (0001) in (hkil) hexagonal indexing indicates one-directional growth of ZnO wires, which is in agreement with previous measurements[92, 93, 94, 95]. Pure CdSSe nanowires shows peaks at (100), (002), (101), (102), (110), and (103) indicating that CdSSe nanowires have wurtzite structure as well[96, 97]. CdSSe/ZnO nanotrees, on the other hand, show a mixture of CdSSe phases, best observed in the

region between 25° and 30 °. The shoulder at 26.5° is indicative of the zinc-blend phase of CdSSe (111)[98] or imperfect (0001) of wurtzite CdSSe, which have similar stacking sequence. The occurrence of transition phase can be explained by the lattice mismatch between CdSSe and ZnO that favors the cubic structure at the interface between the (1010) surface of hexagonal ZnO and the (0001) surface of hexagonal CdSSe. The extent of this transition region cannot be deduced from our measurements. However, the SEM image in Figure 3.3 (c) shows clearly a hexagonal system for caps and branches and indicates that the wurtzite structure prevails.

It should be noted that CdSSe phases in both bare CdSSe and ZnO/CdSSe have almost identical band gaps. The position of the (002) peak confirms the composition of the CdSSe branches[99]. According to Vegard's law, S:Se in ZnO/CdSSe is estimated as 0.54:0.46, and 0.56:0.44 in CdSSe. Comparison with measurements published by Pan et al. shows that the composition is close to S:Se 0.54:0.46 in good agreement with the EDS results [100]. Intermixing of Zn into the CdSSe lattice would lead to a substantial shift of the (002) peak towards larger angles. The measured angle for the (002) peak in the nanocomposite is 26.1°, considerably smaller than that of ZnS or ZnSe with 27.7° and 27.0°, respectively. This result is supported by optical band gap measurements.

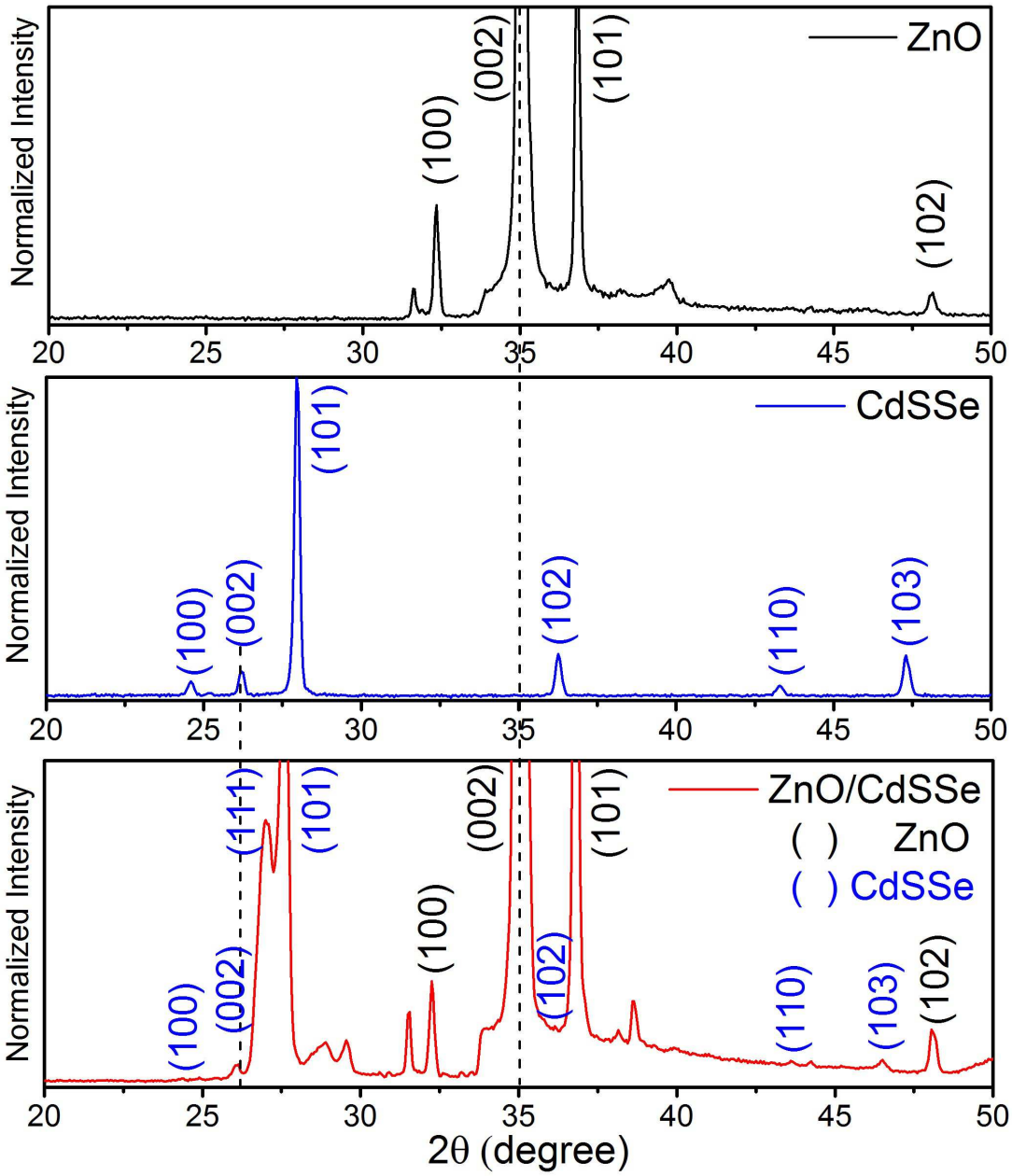

Figure 3.6: XRD spectra of ZnO, CdSSe, and ZnO/CdSSe nanotrees.

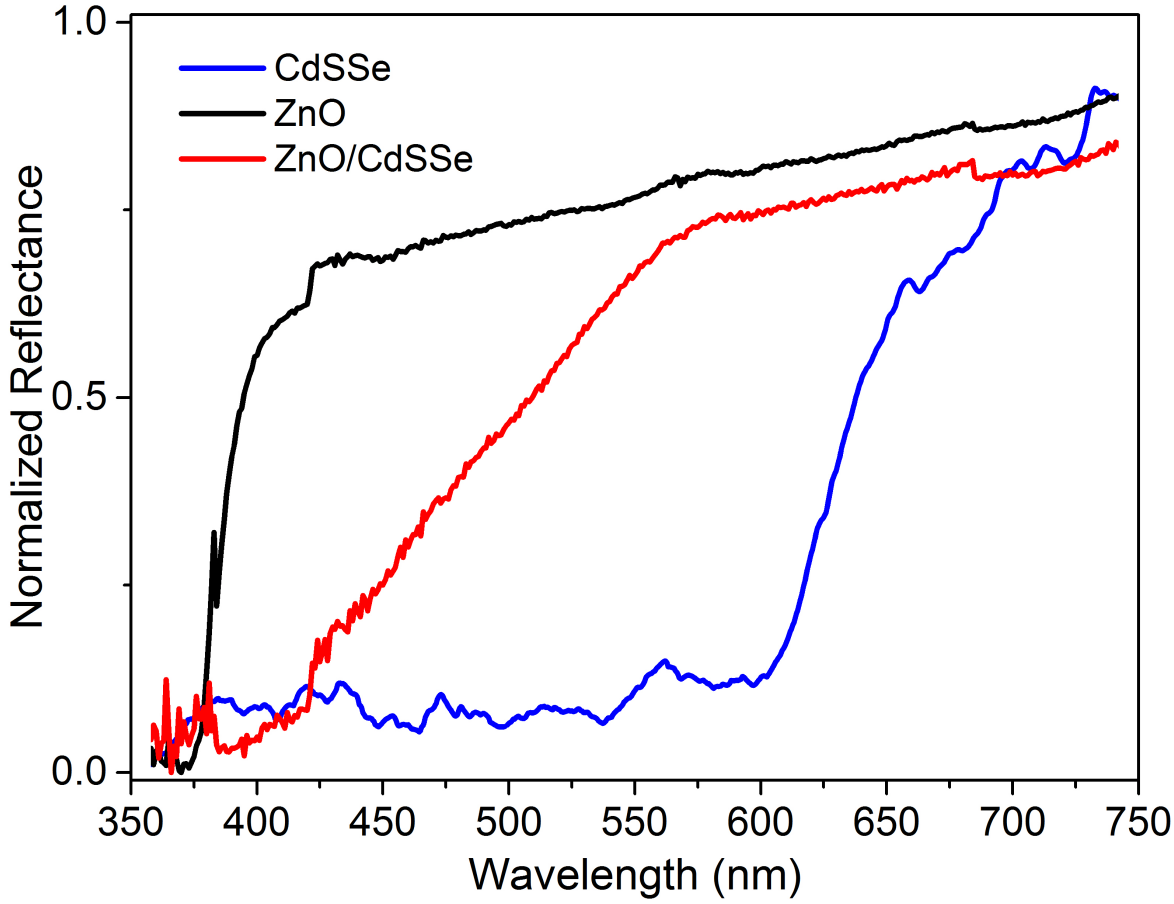

Figure 3.7: Reflectance spectra of ZnO, CdSSe, and ZnO/CdSSe nanotrees.

3.4 UV-Vis Reflectance of ZnO/CdSSe Nanotrees

Diffuse reflectance spectra (DRS) spectra are shown in Figure 3.7. Bare ZnO nanowires absorb light at wavelengths below 390 nm corresponding to a band gap of 3.21 eV which is smaller than the bulk value and comparable to values reported for other ZnO nanowires[97].

The CdSSe/ZnO nanotrees showed a gradual increase in absorption starting around 420 nm. This gradual increase results from a mixture of ZnO and CdSSe at the surface of the sample (Figure 3.3 (b) and (c)). Pure CdSSe nanowires that were grown simultaneously on the same substrate in an area without ZnO coverage showed absorption onset at 1.98 eV. Band gap energies (Eg) were determined from the

spectra by applying the Kubelka-Munk (K-M) method[101]. In K–M method, F(R) is a function of reflectance (R) in eq. 3.1, and Ea is energy in eV derived from eq. 3.2.

$$F = \frac{(1-R)^2}{2R} \tag{3.1}$$

$$Ea(energy\ in\ eV) = \frac{1240}{\lambda} \tag{3.2}$$

The plot, $\sqrt{F \times Ea}$ vs. Ea was made shown in Figure 3.8. The band gap value is the intercepting point of the x axis and the tangent along with most sharply increasing $\sqrt{F \times Ea}$. Therefore, the band gap value of CdSSe is 1.98 eV, and the band gap value of ZnO is 3.21 eV. From the graph, it can be seen that K-M curve of ZnO/CdSSe does not increase sharply but consists of curves with different slopes. The lower energy part has similar band gap value with that of CdSSe, and the higher energy part is due to ZnO, so CdSSe in ZnO/CdSSe nanotrees is supposed to have the same S:Se ratio with CdSSe sample.

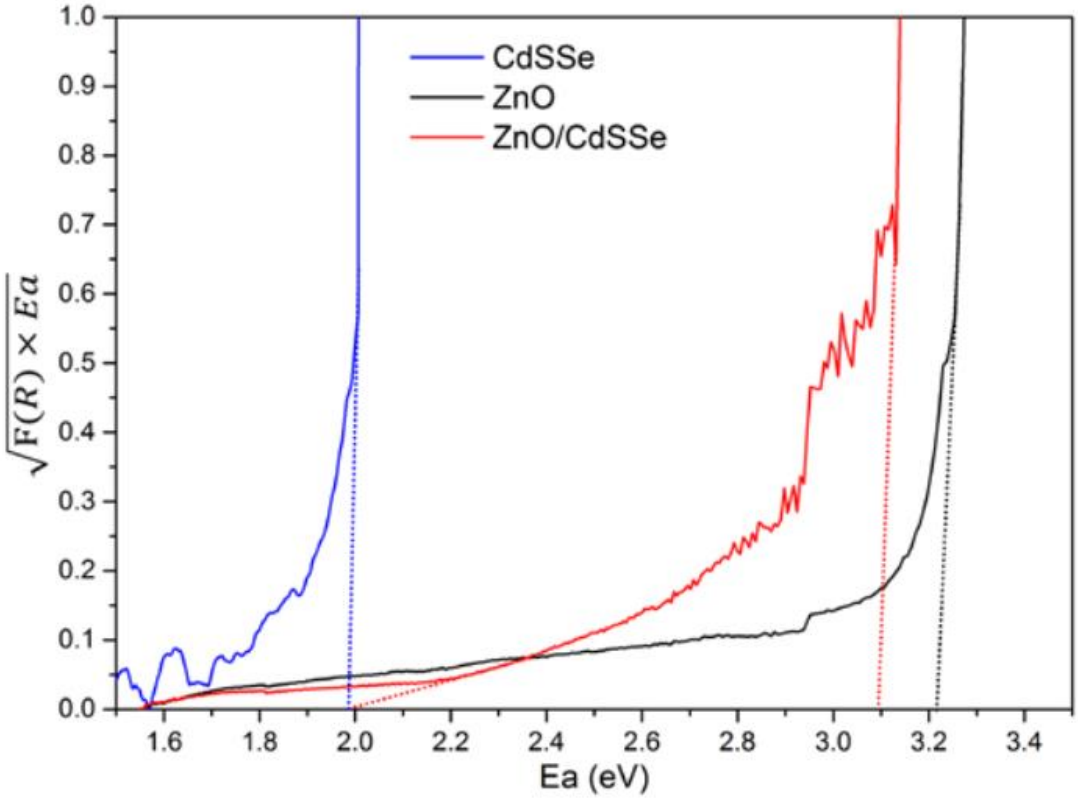

Figure 3.8: K-M plots of ZnO, CdSSe, and ZnO/CdSSe nanotrees.

The band gap of CdSSe can be used to estimate the S:Se ratio with the empirical optical bowing model in eq. 3.3[102].

$$Ea_{CdSSe} = Ea_{CdS} \times x + Ea_{CdSe} \times (1 - x) - bx(1 - x) \tag{3.3}$$

Here, x is the percentage of S and b is the direct band gap bowing parameter for nanowires with a value of (0.59 ± 0.09) eV[102]. Ea_{CdS} has a value of 2.43 ± 0.02 eV and Ea_{CdSe} has a value of 1.76 ± 0.02 eV. The measured band gap energy of CdSSe (1.97 ± 0.04) eV results in a S:Se ratio of 0.53:0.47 that agrees very well with EDS and XRD measurements. DRS also supports that the concentration of Zn in the branches is negligible. Band gap values for pure ZnS and ZnSe range between 3.91 eV and 2.70 eV, respectively [103, 104]. However, no blue shift was observed between pure CdSSe wires and CdSSe/ZnO nanotrees. DRS spectra of the same sample under the same conditions were taken again after three months. No differences were observed confirming long-term stability of the nanotrees.

3.5 PL Measurements of ZnO/CdSSe Nanotrees

Luminescence images of the nanotrees with 385 nm short-pass excitation filter and 400 nm long-pass emission filter are shown in Figure 3.9. Both ZnO and CdSSe were excited in this measurement; however, only the green defect luminescence from ZnO was detected. Figure 3.9 (a) shows a top view of a number of fluorescent ZnO/CdSSe nanotrees. The tips of the branches emit stronger than the base that is attached to the stem. In addition, emission from the top of the stem is much weaker. Since the stem is covered with a thin CdSSe cap at the top, it is likely that luminescence of the branch base and the cap is quenched more efficiently due to the smaller distance to the ZnO stem. Quenching of CdSSe emission is indicative of charge transfer from CdSSe to ZnO. Since ZnO has the larger band gap, this implies a type II heterojunction that can give rise to Z-scheme charge transfer[91, 105] .

In color space analysis, the nanotrees were removed from the substrate, suspended in ethanol and deposited on fused silica substrate. Unfortunately, this procedure results in damage to the branches. The single CdSSe nanowire in the left corner in Figure 3.9 (b) emits stronger than the CdSSe branches attached to ZnO stems. This supports that luminescence is quenched by charge transfer to ZnO. The bare ZnO shows the well-known green emission from defect states. A single ZnO/CdSSe NT was selected in 3.9 (c) for color space analysis shown in Figure 3.9 (d). The color space analysis shows ZnO emission below 520 nm and CdSSe emission above 570 nm and confirms the results from SEM EDS measurements.

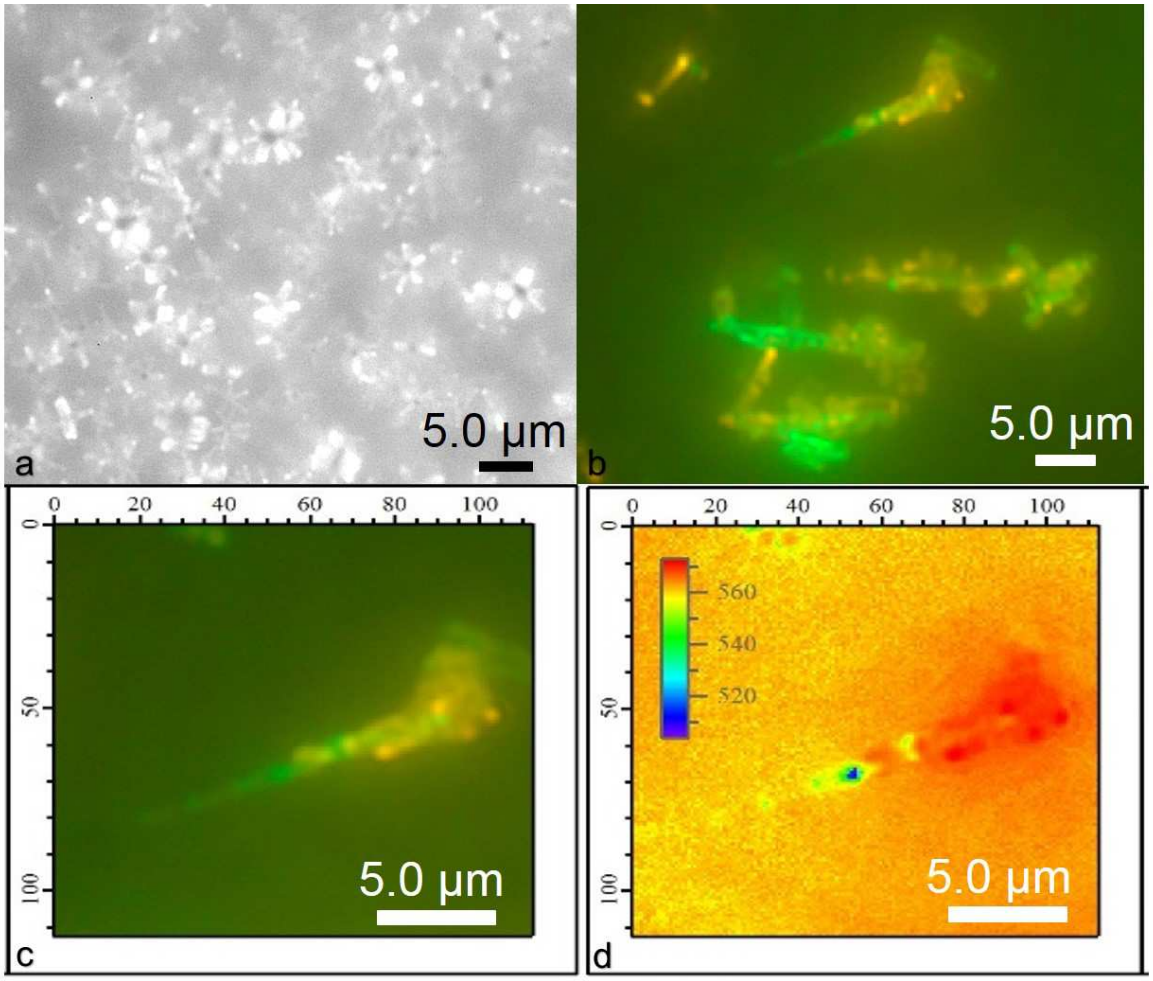

Figure 3.9: Luminescence of ZnO/CdSSe nanotrees in (a) RGB-mode fluorescence emission image of ZnO/CdSSe nanotrees suspension in ethanol in (b) and a selected tree in (c), and color space analysis of (c) in (d).

PL spectra of bare CdSSe nanobelts and CdSSe/ZnO nanotrees are shown in Figure 3.10. The control samples, CdSSe and ZnO, were prepared under the same conditions as stated above. The emission of CdSSe (blue line) shows a maximum at around 650 nm. According to Pan et al. [100] the ratio of 0.51:0.49 gives rise to emission at a wavelength of 650 nm, which agrees well to our result for a 0.53:0.47 ratio. The emission maximum of ZnO is around 514 nm which agrees with defect fluorescence. ZnO/CdSSe nanotrees show a much broader emission between 550 and 750 nm when compared to bare CdSSe. This is a first indication for band-to-band were radiative recombination can occur between the CB of ZnO and the valence band of CdSSe at the interface and result in emission at energies lower than the band gap of CdSSe (see Figure 3.13 (a) and (d)). As explained above, addition of Zn to either CdS or CdSe leads to a blue shift of the luminescence and cannot explain the extension of the PL spectrum from the nanotrees into the red spectral region[106] . Another explanation could be the formation of deep trap states at the interface between ZnO and CdSSe. TCSPC measurements were performed to distinguish between slow emission from trap states and fast band-to-band PL that can give rise to Z-scheme charge transfer.

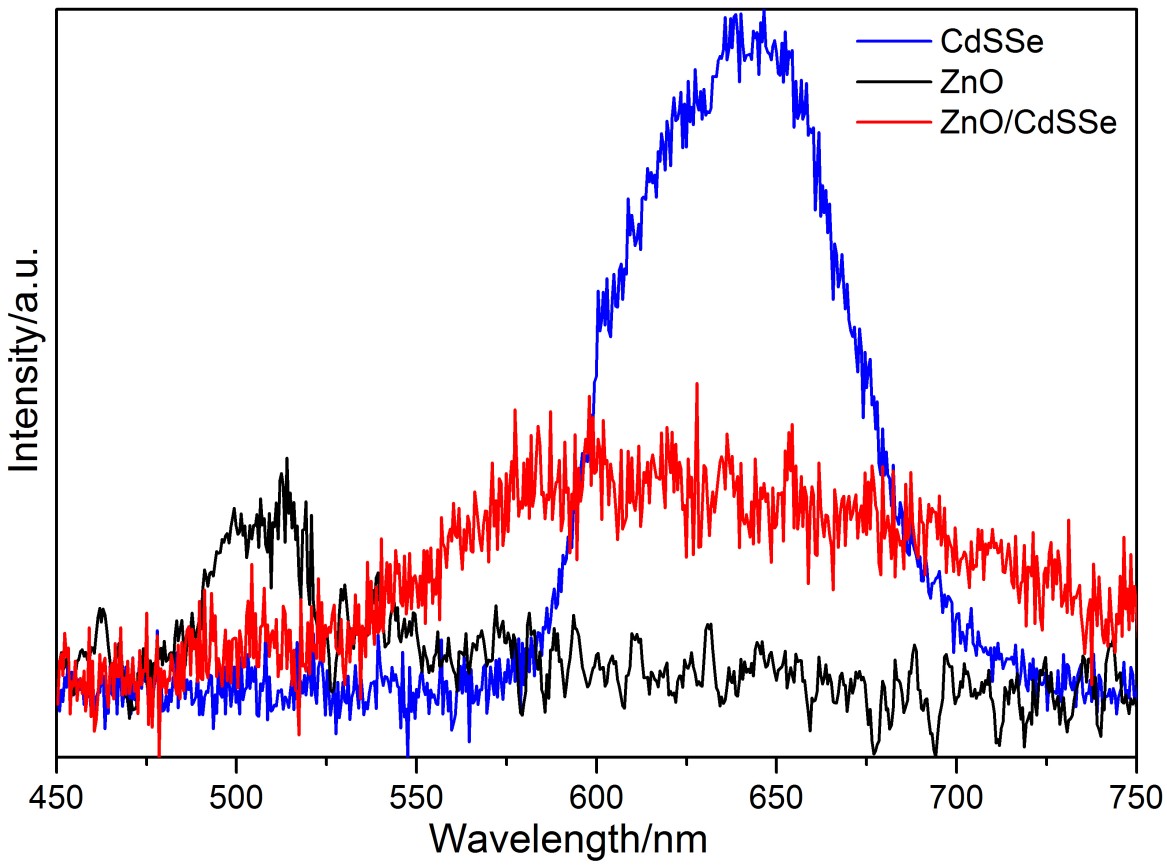

Figure 3.10: PL spectra of ZnO, CdSSe, and ZnO/CdSSe nanotrees.

3.6 Time-resolved Fluorescence Lifetime Measurements

Time-resolved fluorescence measurements employing TCSPC are shown in Figure 3.12. PL lifetimes of nanotrees were measured at 600 nm, 650 nm, and 700 nm emission wavelength selectively measuring emission from CdSSe branches and caps. Lifetime of bare CdSSe and ZnO wires was measured at 650 nm and 500 nm, respectively, after excitation at 400 nm.

The inset in Figure 3.12 shows lifetimes for the three samples. Lifetimes of bare ZnO and bare CdSSe agree well with previously reported values[107, 108, 109, 110, 111]. ZnO shows single exponential decay while CdSSe shows bi-exponential decay that has been observed for CdSSe nanowires earlier and can be associated to trap and surface-state recombination at later times[112, 109, 110, 113, 114].

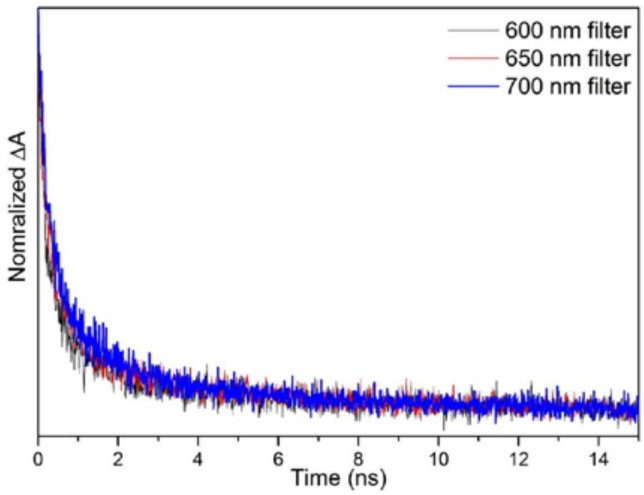

Fitting parameters of double decay curves

	A1	τ1	A2	τ2
600 nm	0.51	0.13	0.49	1.30
650 nm	0.58	0.11	0.42	1.33
700 nm	0.54	0.14	0.46	1.32

Figure 3.11: Comparison of lifetime measurements of ZnO/CdSSe nanotrees with 600 nm, 650 nm, and 700 nm emission filters. The same ZnO/CdSSe nanotree samples were measured with 600 nm, 650 nm, and 700 nm emission filters. Fitting parameters are shown at the right.

PL lifetimes for the nanotrees are identical at 600 nm, 650 nm, and 700 nm shown in Figure 3.11. PL lifetime from the nanotrees are much faster compared to lifetimes from either the bare ZnO or the bare CdSSe nanowires. The latter explains the efficient luminescence quenching in the composite material observed in the PL micrographs (Figure 3.9).

The fact that the emission at 700 nm shows the same rapid decay indicates that emission at this wavelength is due to band-to-band PL rather than deep interface trap states. Comparing the fast component for the three different systems allows us to calculate the rate of charge transfer from CdSSe branches to the ZnO stem in the nanotrees using Equation 5.2[114, 115].

$$k_{ET} = 1/\tau_{ZnO/CdSSe} - 1/\tau_{CdSSe} \tag{3.4}$$

At 400 nm excitation, the fast component of the PL lifetime for nanotrees is 0.11 ns, much shorter than that of ZnO (3.67 ns) and CdSSe (1.06 ns). Using these lifetimes, Equation 5.2 results in an electron transfer rate of $0.37 \times 10^9\ s^{-1}$. PL lifetimes have also been measured with 290 nm and 580 nm excitation. At 580 nm excitation and 650 nm detection the PL lifetime of the trees is even shorter and approaches the intensity of the Rayleigh scattering (IRS) that is measured with an N-BK7 glass diffuser used as a blank sample. This can be explained by trap states in the ZnO nanowires or at the interface that can be excited at 400 nm but are not accessible with 580 nm and show a longer lifetime (Figure 3.13 (c)). The lifetime for pure CdSSe nanowires is almost identical for 290 nm and 400 nm excitation. At 290 nm excitation the PL lifetime of the nanotrees is around 0.65 ns, a factor of 5 slower compared to 400 nm excitation and a factor of 10 slower compared to 580 nm excitation. This can be explained by a simultaneous population of CB states in ZnO that partially blocked electron transfer from CdSSe to ZnO (Figure 3.13 (b)). The PL lifetime measurements support that the nanotrees are promising candidates for Z-scheme charge transfer (Figure 3.13 (a)).

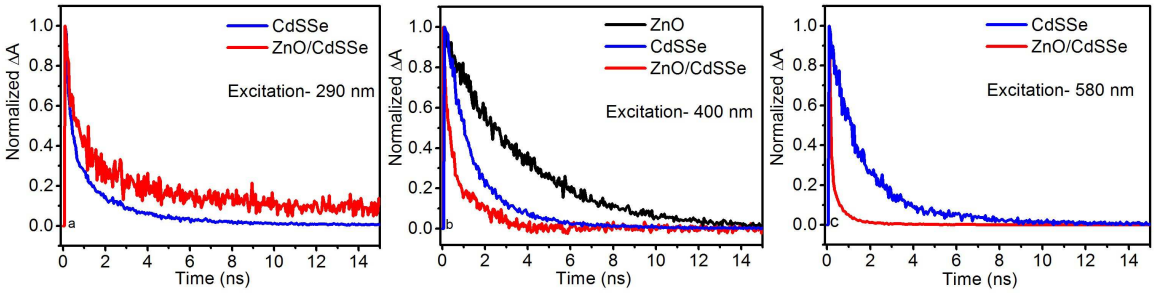

Figure 3.12: Time-resolved fluorescence measurements of ZnO, CdSSe, and ZnO/CdSSe nanotrees for different excitation wavelength.

The band alignment at the interface between CdSSe and ZnO shown in Figure 3.13 can be deduced by combining the results from time and spectrally resolved PL measurements. Our results indicate that CdSSe/ZnO nanotrees form an n-n Type II heterojunction. Comparison of the PL spectra shows that the CB of CdSSe is located about 300 meV above the CB of ZnO. Fast luminescence quenching at the maximum emission wavelength of CdSSe as well as at wavelengths that are associated with type-II band-to-band transitions above 700 nm indicate that the interfacial charge transfer is not dominated by defect or trap states.

Comparison of PL dynamics at different excitation energies confirm charge transfer from CdSSe to ZnO and suggest that Z-scheme charge transfer should be observable in the present material.

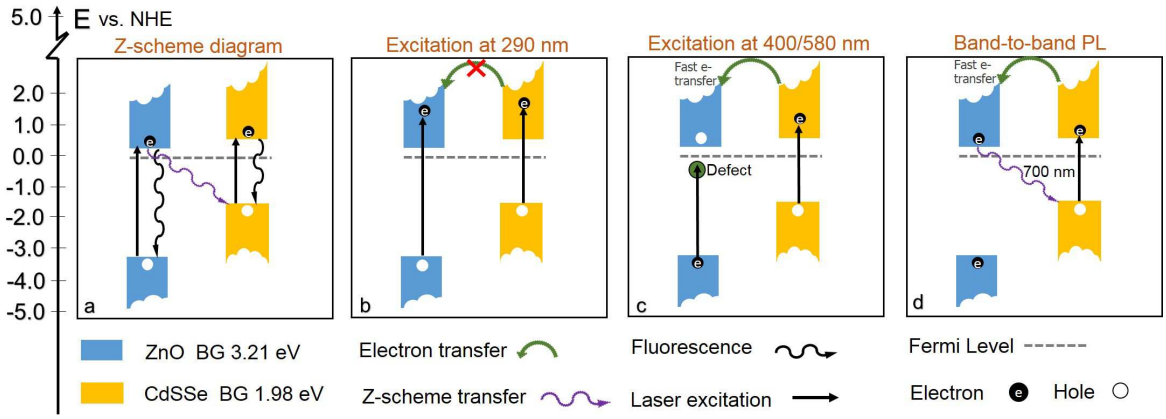

Figure 3.13: Band gap diagram and scheme of electron transfer reactions; (a) Z-scheme proposed for the nanotrees: After two photon absorption the hole resides in the ZnO stem and the electron in the CdSSe branch. (b) Experiments performed with 290 nm: the simultaneous excitation of ZnO reduces density of acceptor states and restricts ET from CdSSe. (c) Excitation below the bandgap of ZnO: Only CdSSe is directly exited. ET to ZnO leads to short PL lifetime. At 400 nm long-lived defect states in ZnO are also excited, explaining the difference in PL response at 650 nm. (d) Short-lived emission at 700 nm after excitation of CdSSe indicates efficient band-to-band PL at the type II hetero-interface.

3.7 Conclusion

A novel vertically aligned tree-like nanostructures composed of CdSSe branches attached to ZnO stems was presented in this chapter. Both materials show predominantly wurtzite structure in the nanotrees. Nanotrees were prepared on different substrates and show long-term photo-stability. We have presented experimental evidence for type II band alignment and fast charge transfer from CdSSe branches to ZnO stems. Band-to-band photoluminescence following charge transfer suggest that this material combination can be used for Z-scheme charge transfer. ZnO/CdSSe nanotrees feature efficient charge transfer, tunable band gap of the CdSSe branches, and substrate-independent vertically-aligned growth, so they are promising nanomaterials for optical, photovoltaic, and photoelectrochemical applications.

Chapter 4

SYNTHESIS AND CHARACTERIZATION OF ZNO/CUO VERTICALLY-ALIGNED HIERARCHICAL TREE-LIKE NANOSTRUCTURE

4.1 Introduction

Ordered arrays of semiconducting tree-like hierarchical nanostructures are of considerable interest in photo-catalysis, photo-electrochemical catalysis, energy storage and photovoltaic conversion because of their larger surface area to volume ratio, more efficient photocurrent conversion, and enhanced quantum efficiency[8, 116, 14, 117]. The photocatalytic activity of heterogeneous hierarchical semiconductors depends strongly on the composition, the structural design, and the electronic properties of the interface[116]. A heterojunction formed at the interface between a p-type and n-type semiconductor nanoparticle can facilitate charge separation and reduce electron/hole recombination dramatically by spatially separating the charge carriers[117].

The combination between ZnO and a narrow band-gap p-type semiconductor is a promising approach to extend the light absorption range of ZnO and increase charge carrier lifetimes at the same time. CuO is a p-type semiconductor with a tunable band-gap between 1.2 eV - 2.1 eV[118]. It shares the low cost, earth abundance and high stability with ZnO. Numerous studies showed that photo-electrochemical efficiency can be improved by the formation of a p-n heterojunction between ZnO and CuO[11, 119, 117].

Several studies reported on the synthesis of ZnO/CuO nanocomposites [120], decoration of ZnO nanostructures with CuO nanoparticles [55], synthesis of ZnO/CuO

core-shell nanowire arrays [121], and ZnO/CuO nanotrees[117]. The later morphology with ZnO branches exposed from the CuO stem, has advantages for solar energy conversion and hydrogen production. The inverse morphology with exposed CuO branches allows to utilize the photocatalytic properties of CuO. Epitaxial growth of CuO (100) on ZnO (0001) has been observed as a strain reducing layer at the Cu_2O/ZnO interface[122]. Generally, ZnO nanowires grow along the [0001] direction while CuO nanowires show growth along [010][123]. Comparing the lattice parameters at the ZnO $(1\,0\,\bar{1}\,0)$ facet and at the CuO (010) facet suggests that CuO nanowires can grow as branches attached to ZnO nanowire stems[124, 125, 126].

ZnO nanowires were synthesized by modifying an established hydrothermal procedure[127]. Reducing the starting concentration and growing the wires upside down resulted in long and straight wires. Subsequently, a seed-growth sequence was applied to grow CuO branches attached to the ZnO wires. The conditions for CuO nanowire synthesis were modified from known hydrothermal procedures[128] and optimized for achieving controlled growth of wire-like branches instead of core-shell structures.

The resulting nanotrees were characterized by UV-Vis, SEM and XRD for electronic and structural properties. CV and EIS in the dark and under illumination were applied to characterize electrochemical and photo-electrochemical properties. Finally, the photocatalytic properties were investigated by photo-degradation of toluene and acetic acid.

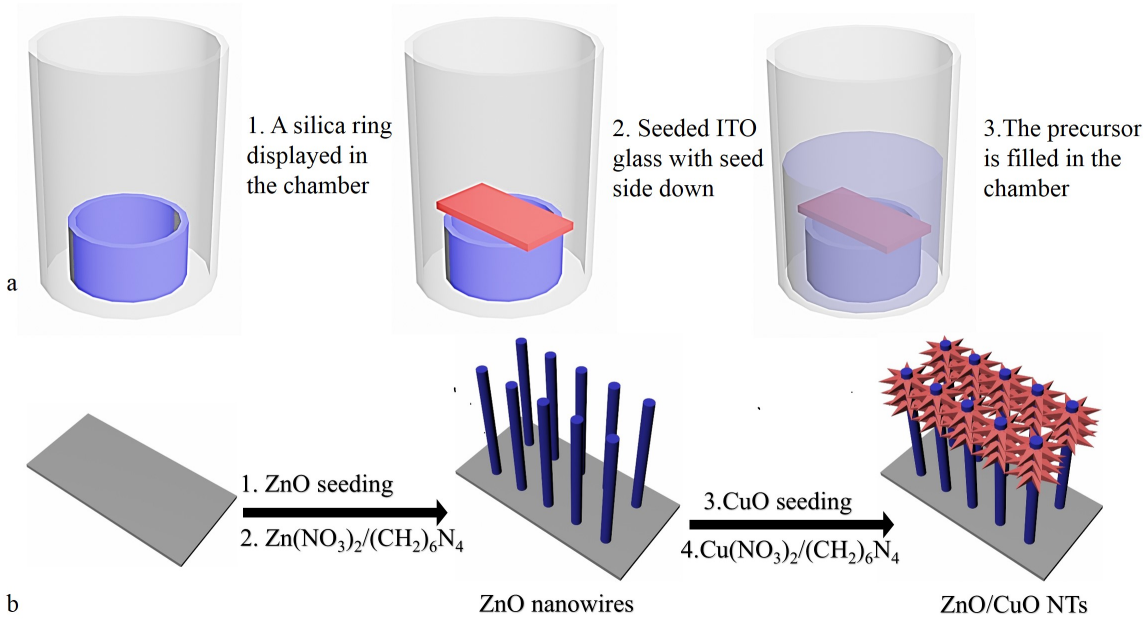

Figure 4.1: The set-up of the autoclave liner for ZnO and CuO hydrothermal growth is shown in (a). The sequence for ZnO/CuO nanotrees synthesis is shown in (b).

4.2 Hydrothermolysis Mechanism of ZnO/CuO Nanotrees

The schematic diagram of the experimental set-up for the synthesis and the steps involved in the synthesis of ZnO/CuO nanotrees are shown in Figure 4.1 (a) and (b), respectively. The reactions leading to ZnO nanowires are shown in eq. 4.1, 4.2, and 4.3[72]. To reduce the formation of random ZnO deposition, the sample was placed with the seed layer facing down on a silica ring as a support.

For the same reason, the synthesis was performed with lower concentration of precursors compared to other established procedures. To obtain the desired nanowire length, the low concentration growth was repeated three times. During the hydrothermal growth, $(CH_2)_6N_4$ releases OH^- and precipitates Zn^{2+} as $Zn(OH)_2$.

$Zn(OH)_2$ is deposited on the ZnO seed layer and is partly converted to ZnO. However, it is well known that the conversion is not complete and residual zinc hydroxide is converted into ZnO by a subsequent annealing step in air[72]. This step can be combined with the annealing of the first CuO seed layer.

$$(CH_2)_6N_4 + 10H_2O \rightarrow 6HCHO + 4NH_4^+ + 4OH^- \tag{4.1}$$

$$Zn^{2+} + 2OH^- \rightarrow Zn(OH)_2 \tag{4.2}$$

$$Zn(OH)_2 \rightarrow ZnO + H_2O \tag{4.3}$$

Figure 4.4 shows a comparison between SEM images of wires prepared with the new approach and an established method with higher concentration precursors and the seed layer facing up during hydrothermal growth. Figure 4.4 (a), 4.4 (b), and 4.4 (c) show images after the first, the second and the third cycle of hydrothermal growth with 5 mM precursor solution. It can be seen that the wires retain their ordered vertical alignment on the substrate during the synthesis and grow in length.

ZnO nanowires prepared with the seed layer facing up and 20 mM precursor solution are shown in Figure 4.4 (d). In addition to thin and vertically-aligned wires the sample shows much thicker and randomly-oriented wires. A sample grown with 3 cycles of low concentration (5 mM) and seed layer facing up is shown as some randomly oriented nanowires in Figure 4.4 (e). The new procedure resulted in the highest density of ordered nanowires and a high degree of homogeneity. The wires from this procedure were around 5 μm in length compared to 2 μm obtained by the established method

(see Figure 4.2).

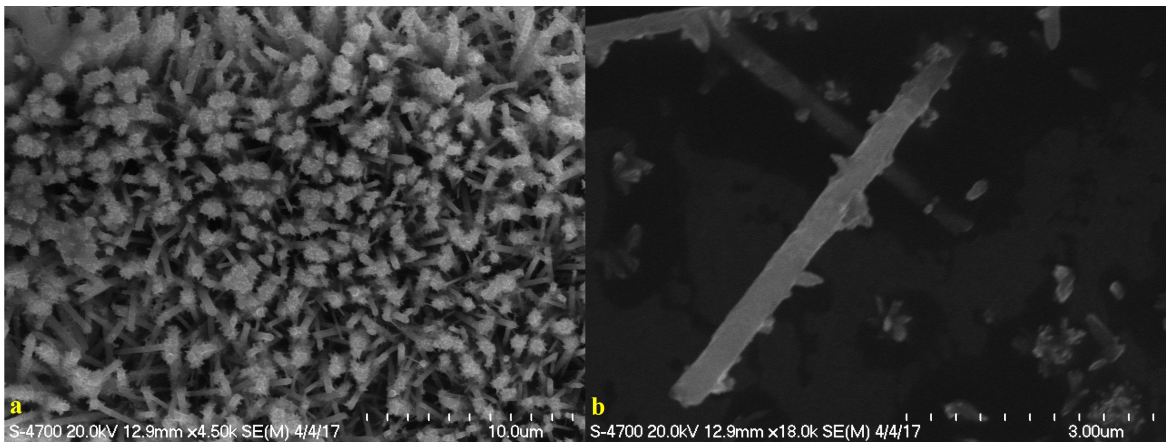

Figure 4.2: SEM images of ZnO/CuO nanotrees (a) and a single ZnO/CuO nanotree (b).

The possible reasons why ZnO nanowires on the silica ring with seed face down were grown in vertically-aligned array without unexpected precipitation may be: 1. less concentrated and no precipitate exist in upper layer of precursor; 2. The ring stabilized and confined the molecule movements in the solution at high temperature; 3. Gravity assisted the growth and precipitate could not stick onto the substrate with the seeded face down. In order to determine the role of the silica ring in the process, the following setups were tested shown in Figure 4.3. In Figure 4.3 (a) and (b), the substrate was displayed with seed face up on the silica ring and under the silica ring, respectively. Huge wire accumulation always happened no matter if the substrate was in the upper layer or lower layer of precursor. Figure 4.3 (c) and (d) show the ZnO nanowires prepared with the method mentioned in the previous section, which allowed the substrate display on the top of the glass ring with seed face down. From 4.3 (c), it is clear that nanowires are vertically-aligned and no precipitate of huge wires showed up in 4.3 (d) that was taken under low magnification. In Figure 4.3 (d) and (f), the substrate stood in the silica ring. It can be seen that array in Figure 4.3 (d) was not as vertically-aligned as in Figure 4.3 (c) and in Figure 4.3 (f), unexpected accumulation is still not avoidable.

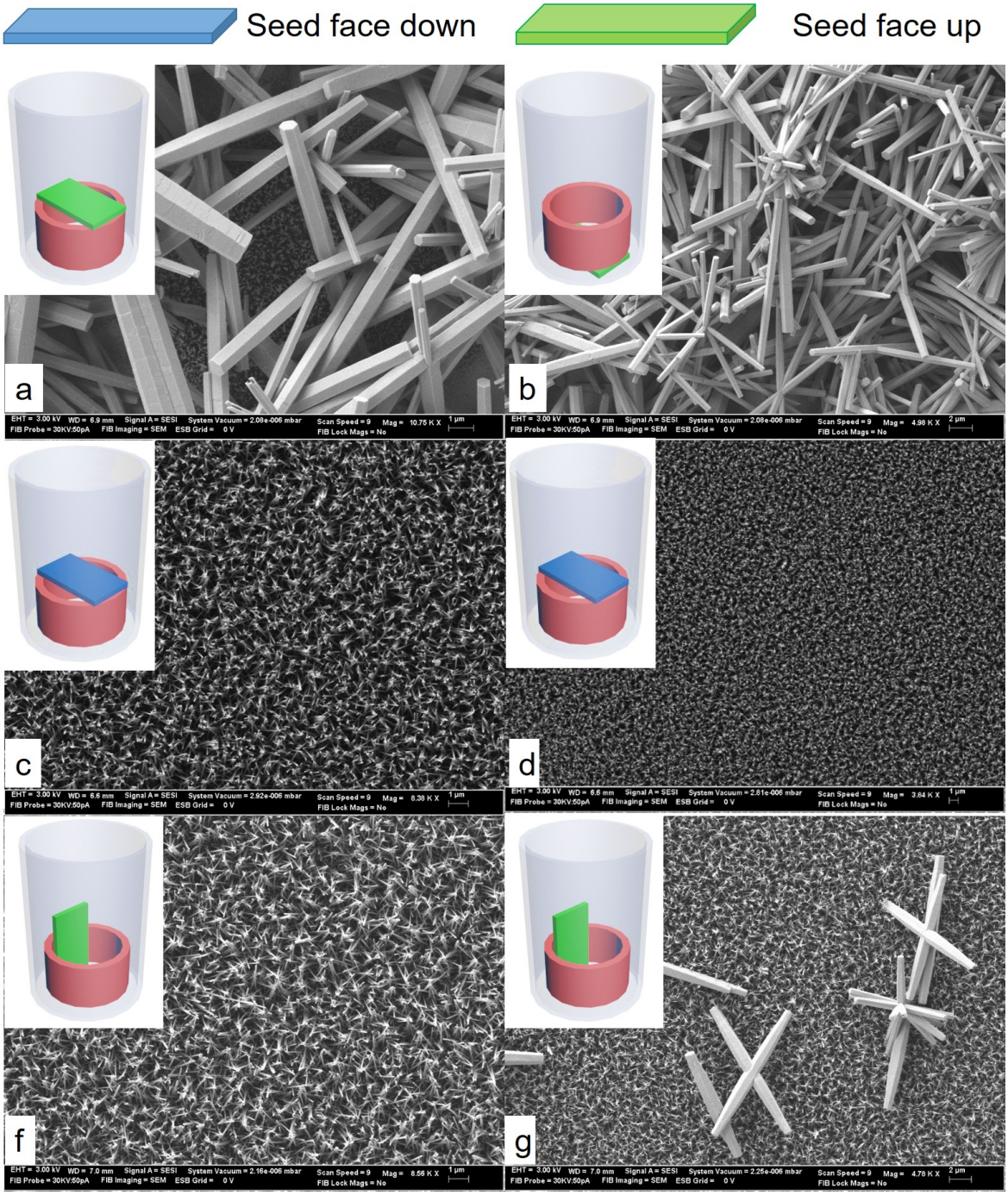

Figure 4.3: SEM images of ZnO nanowires grown with seed face up on the silica ring (a), seed face up under the silica ring (b), seed face down on the silica ring (c, d), and seed face vertically standing in the silica ring (f, g).

After preparation of the ZnO nanowires that represent the stems for the nanotrees, the CuO branches are grown following the reaction steps in the following equations

$$NH_3 + H_2O \rightarrow NH_4^+ + OH^- \tag{4.4}$$

$$Cu^{2+} + 4NH_4^+ \rightarrow [Cu(NH_3)_4]^{2+} + 4H^+ \tag{4.5}$$

$$[Cu(NH_3)_4]^{2+} + 4OH^- \rightarrow [Cu(OH)_4]^{2-} + 4NH_3 \tag{4.6}$$

$$[Cu(OH)_4]^{2-} \rightarrow Cu(OH)_2 + 2OH^- \tag{4.7}$$

$$Cu(OH)_2 \rightarrow CuO + H_2O \tag{4.8}$$

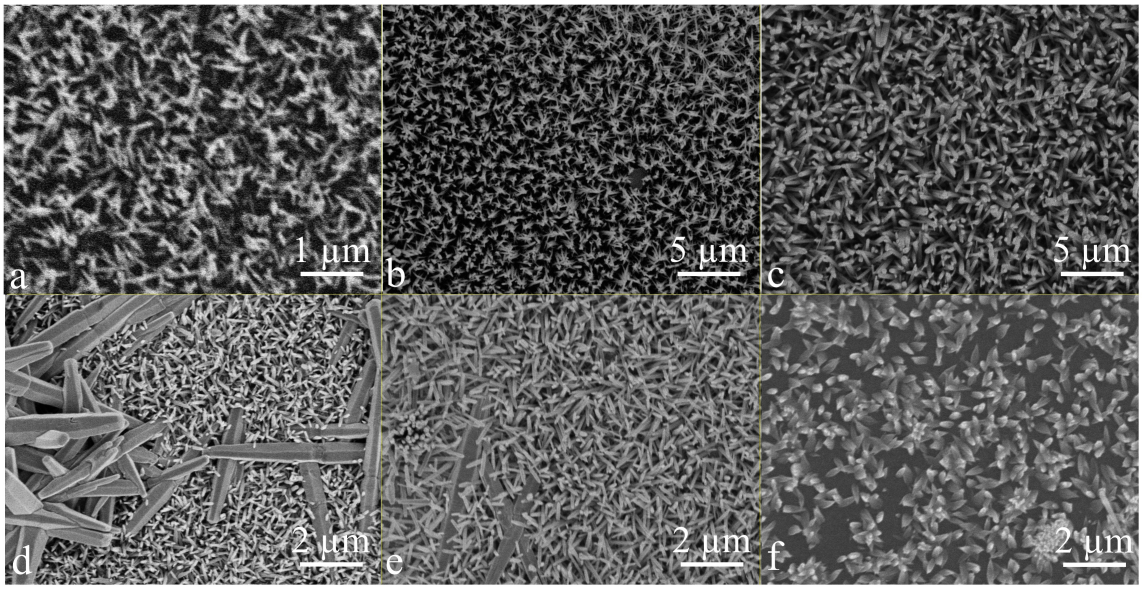

Figure 4.4: SEM images after 1st (a), 2nd (b), and 3rd (c) cycle of hydrothermal growth of ZnO nanowires with seeded side facing down, (d) traditional high concentration hydrothermal growth of ZnO with seeded side facing up, (e) three cycles of low concentration hydrothermal growth of ZnO nanowires with seeded side facing up, and (f) hydrothermal growth of CuO nanorods prepared with the same amount of precursors used in ZnO/CuO nanotrees.

4.3 Structural Characterizations of ZnO/CuO Nanotrees

SEM images of ZnO nanowires and ZnO/CuO nanotrees with different magnifications are shown in Figure 4.5 and Figure 4.2. CuO branches show the parallelepipedal shape that is compatible with a monoclinic crystal structure. The branches are about 200 nm in length. Figure 4.5 (b) suggests that the ZnO stems are not fully covered by CuO branches. The majority of branches are attached to the upper part of the ZnO wires. This can be explained by the limited wettability and precursor diffusion in the ZnO nanowire array during the hydrothermal growth.

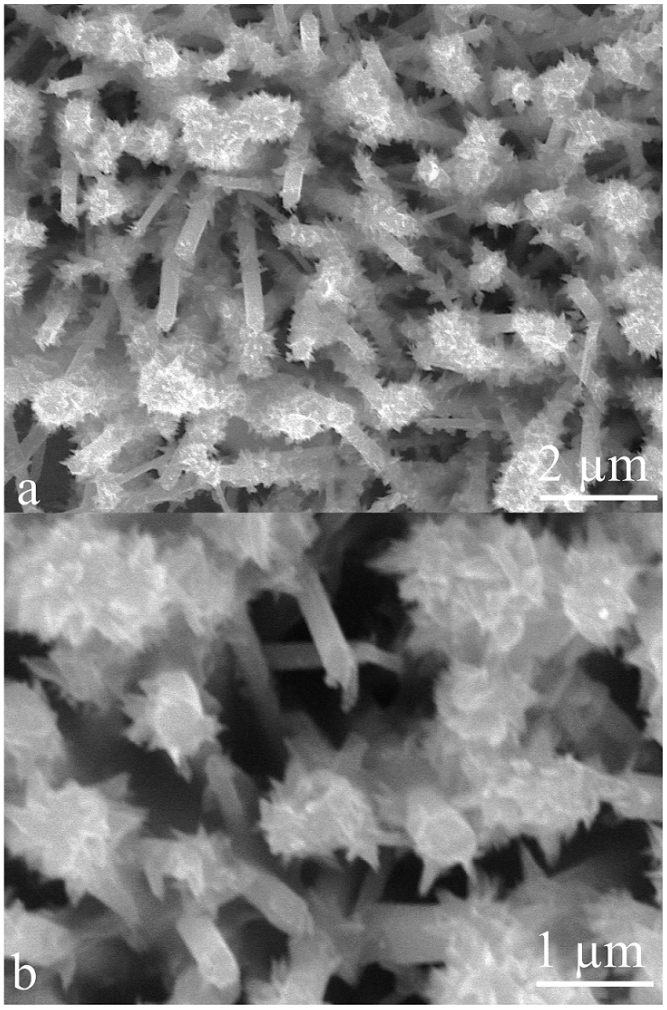

Figure 4.5: SEM images of ZnO/CuO nanotrees with different magnifications.

XPS was used to measure the surface composition of the ZnO/CuO nanotrees sample shown in Figure 4.6 with C 1s (C-C binding energy: 284.5 eV)[129] as charge correction reference. As expected, the main components of the nanotrees are Zn, O, and Cu (Figure 4.6 (a)).

The contribution from carbon is contaminants in the form of adventitious carbon due to benchtop synthesis and exposure to laboratory air. This assignment is confirmed by the structure of the O 1s contribution that can be fitted by three Gaussian peaks (Figure 4.6 (b) red, yellow, and blue curve).

Contributions at 531.1 eV can be attributed to mostly chemisorbed and dissociated O_2^{2-}, O^-, and OH^-. This specific adsorbed O cannot be completely removed at temperature of 250 °C[130, 131]. The peaks at 530.0 eV, and 528.9 eV can be assigned to O^{2-} in ZnO lattice and in CuO, respectively[55, 132, 133, 134, 130, 131].

The Zn 2p region shown in Figure 4.6 (c) reveals peaks at 1044.6 eV and 1021.4 eV that are assigned to Zn $2p_{1/2}$ and Zn $2p_{3/2}$ levels in Zn^{2+} in the wurtzite ZnO structure, respectively[129]. The Cu 2p region in Figure 4.6 (d) shows the expected Cu^{2+} peaks and satellites of CuO: Cu $2p_{1/2}$(s) (963.3 eV), Cu $2p_{1/2}$ (953.4 eV), Cu $2p_{3/2}$(s) (941.7 eV), and Cu $2p_{3/2}$ (932.8 eV)[55, 135]. Cu^{1+} in Cu_2O peaks, on the other hand, would be expected to show much weaker satellites[136] and an overall shift to lower energies[129].

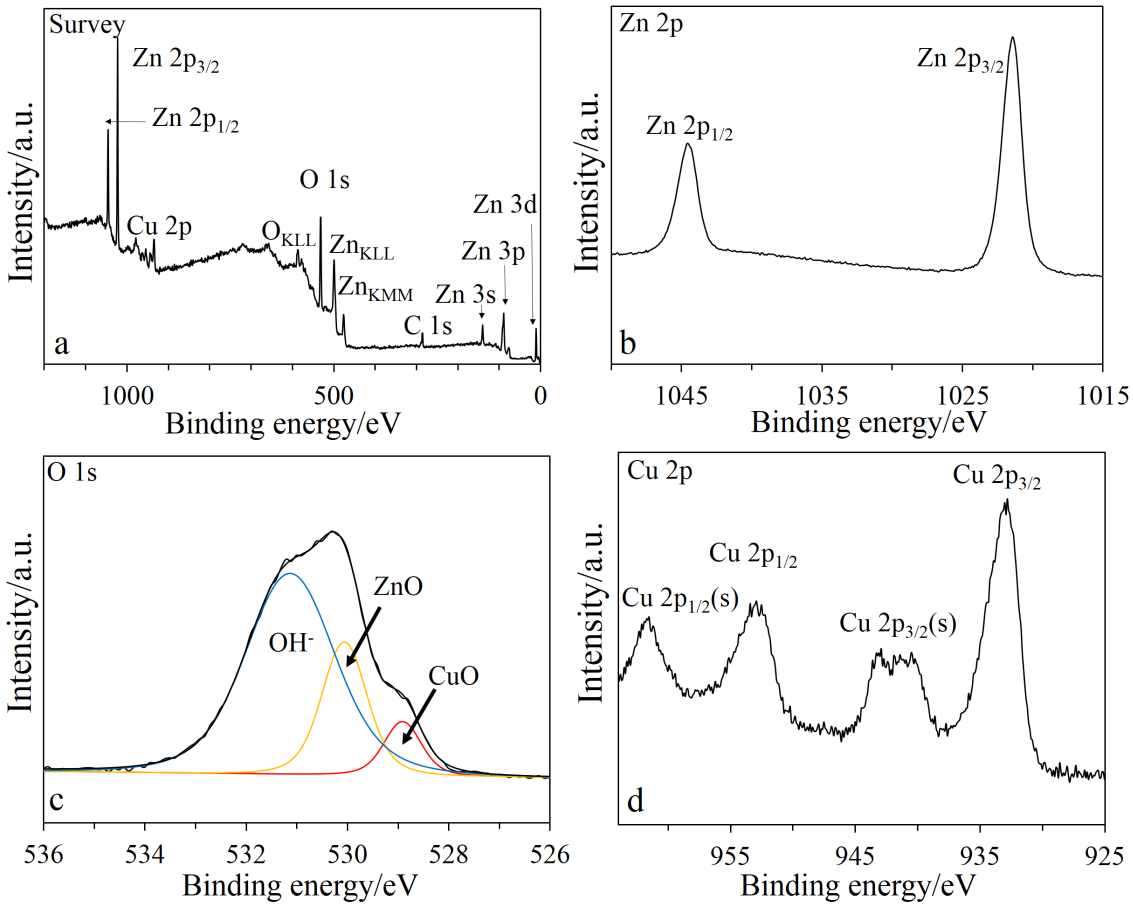

Figure 4.6: XPS spectrum of ZnO/CuO nanotrees (a) and high-resolution spectrum of Zn 2p, O 1s, and Cu 2p peaks, respectively(b-d).

SEM images of the trees suggest that CuO branches are attached preliminary to the top of the stems. To confirm this morphology we compared standard XRD and high-resolution thin-film pattern. Standard $2\theta/\theta$ XRD mode shown in Figure 4.7 probes the whole depth of the ZnO/CuO nanotree film. Consequently, the signal is dominated by contributions from wurtzite ZnO involving (100), (002), (101), and (102) peaks [JCPDS file No.36-1451] and sapphire involving (006) [JCPDS file No. 46-1212].

In high-resolution thin-film mode (Figure 4.7 inset), the detection depth can be estimated to be 1 μm and the XRD pattern shows (111) and $(11\bar{1})$ peaks from the monoclinic CuO branches in addition to the ZnO peaks [JCPDS file No. 45-0937]. The XRD measurements confirm that the nanotrees consist of wurtzite ZnO nanowire stems decorated on the top with monoclinic CuO branches. The cubic structure of Cu_2O is not observed.

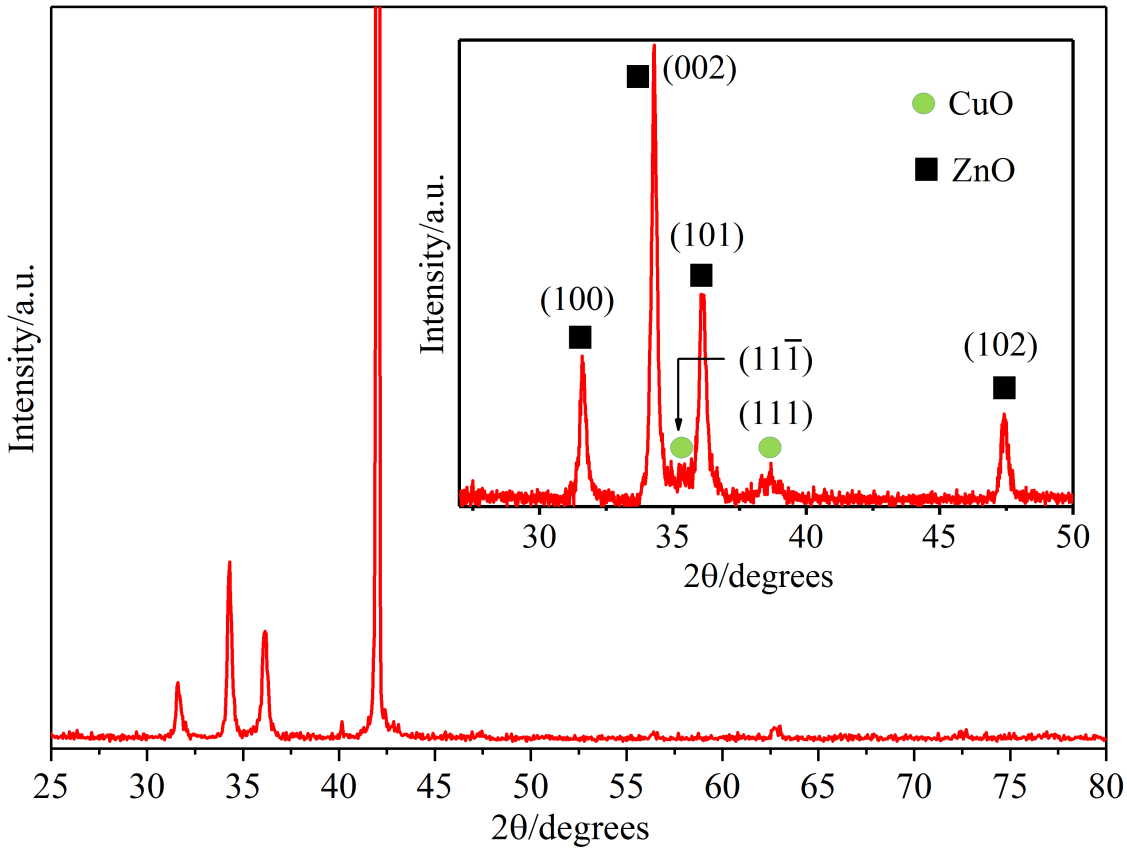

Figure 4.7: XRD spectrum of ZnO/CuO nanotrees in coupled $2\theta/\theta$ mode, inset: XRD spectrum of ZnO/CuO nanotrees in high-resolution mode.

4.4 Optical Characterizations of ZnO/CuO Nanotrees

UV-Vis absorption spectroscopy was employed to determine the band gap of the pure ZnO sample, the pure CuO sample and the ZnO/CuO nanotrees (Figure 4.8). Band gap values were calculated via the K-M method[101] which has been discussed in Chapter 3 but in this chapter, UV-Vis spectra were in T, so the conversion from T to R was done with eq. 4.9 and 4.10.

$$A = 2 - log(\%T) \tag{4.9}$$

$$A = log(1/R) \tag{4.10}$$

The K-M plot was shown in inset in Figure 4.8. The resulting band gaps are 3.36 eV for pure ZnO and 1.21 eV for pure CuO. These band gaps agree well with reported bulk values[137, 138]. For the nanotrees the corresponding band gaps are very similar, 3.25 eV for ZnO stems and 1.21 eV for CuO branches as shown in the inset in Figure 4.8. This confirms that the nanotrees are bi-material structures and the synthesis of the CuO branches does not lead to major doping of the ZnO stems, since Cu doping has been reported to shift the absorption onset of ZnO nanoparticles to 3.55 eV upon 5% doping[139].

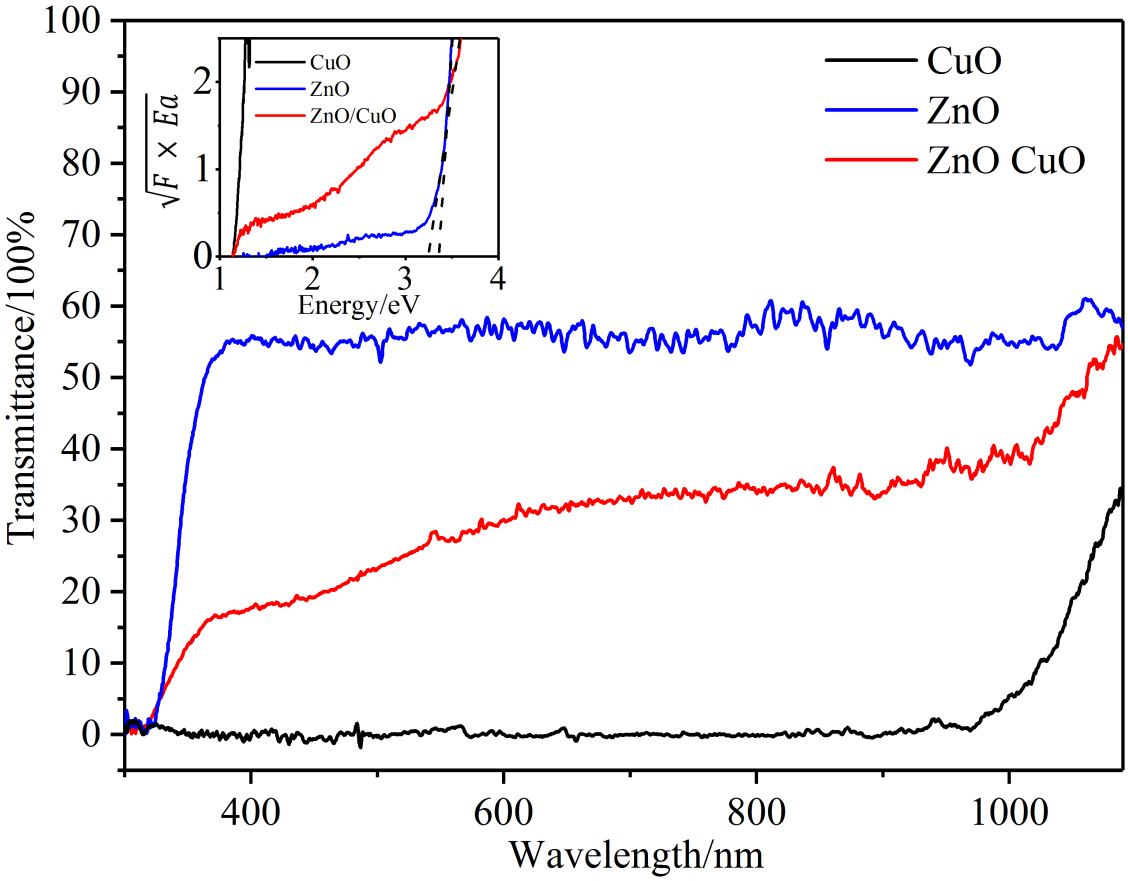

Figure 4.8: UV-Vis transmittance spectra of CuO, ZnO, and ZnO/CuO nanotrees (inset: K-M analysis with normalized UV-Vis transmittance spectra).

4.5 Electrochemical and Photoelectrochemical Properties of ZnO/CuO Nanotrees

Cyclic voltammetry measurements were carried out in the dark with a scan rate of 40 mV/s on ZnO, CuO, and ZnO/CuO nanotrees in 1 mM $Fe(CN)_6^{3-}/Fe(CN)_6^{4-}$ in 0.1 M KCl aqueous solution (Figure 4.9 a) and in 1 mM ferrocene in 0.1 M $BuNF_4$ acetonitrile solution (Figure 4.9 b). In both systems the nanotrees displayed the highest oxidation and reduction peak currents. This indicates that the interfacial charge transfer is more efficient for ZnO/CuO nanotrees compared with pure ZnO and CuO nanowires and the addition of the CuO branches did not decrease the conductivity.

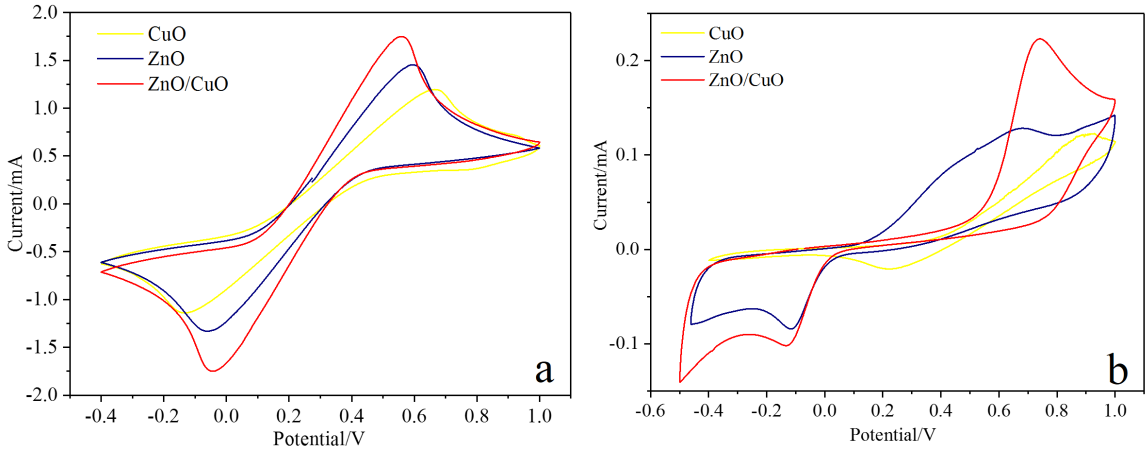

Figure 4.9: CV curves of CuO, ZnO, and ZnO/CuO nanotrees in 1 mM $Fe(CN)_6^{3-}/Fe(CN)_6^{4-}$ in 0.1 M KCl aqueous solution (a), and 1 mM ferrocene in 0.1 M $BuNF_4$ in acetonitrile (b).

This can either be explained by the increase in surface area in the hierarchical nanotrees and/or by charge separation at the p-n heterojunction between CuO and ZnO resulting in an increase in carrier lifetime.

Scan rate dependent cyclic voltammograms were collected for the ZnO/CuO nanotrees in 1 mM $Fe(CN)_6^{3-}/Fe(CN)_6^{4-}$ in 0.1 M KCl aqueous solution (Figure 4.10 (a)), and in 1 mM ferrocene in 0.1 M $BuNF_4$ acetonitrile solution (Figure 4.10 (b)). The inset in Figure 4.10 (a) and (b) show the shift of anodic and cathodic peak currents with the square root of scan rate. The peaks shift linearly with a fitted R^2 of 0.9987 (oxidation) and 0.9972 (reduction) for water, and 0.9976 (oxidation) and 0.9869 (reduction) for acetonitrile. This indicates that the reaction is diffusion-controlled and that charge transfer across the ZnO/CuO interface is not the rate-limiting step[140, 141, 142].

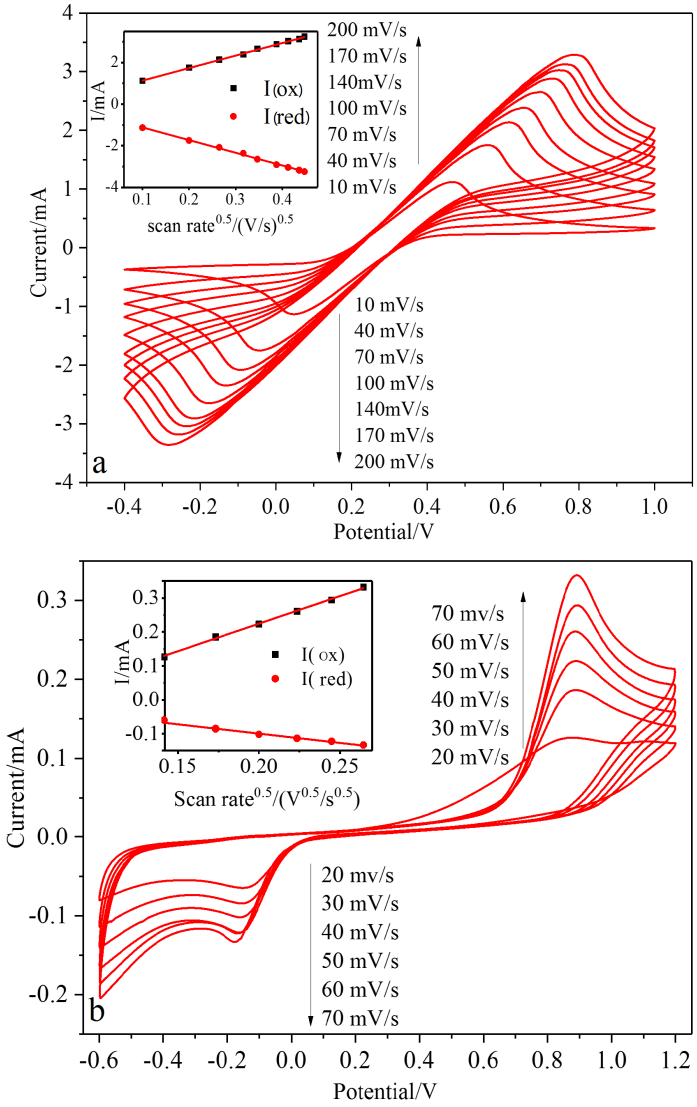

Figure 4.10: Scan rate-resolved CV curves of ZnO/CuO nanotrees in 1 mM $Fe(CN)_6^{3-}/Fe(CN)_6^{4-}$ in 0.1 M KCl aqueous solution, and in 1 mM ferrocene in 0.1 M $BuNF_4$ in acetonitrile. (insets: current vs square root of scan rate).

EIS was performed in the dark and under illumination in $Fe(CN)_6^{3-}/Fe(CN)_6^{4-}$ at the open circuit voltage. Nyquist plots of the measurements on pristine ZnO nanowires and CuO/ZnO nanotrees in the two solvents are shown in Figure 4.12 (a) and Figure 4.11 (a). The diameter of the semicircle along the real axis corresponds to the charge transfer resistance and serves as an indicator for the electrochemical activity of the electrode. ZnO/CuO nanotrees have smaller arc radius corresponding to smaller charge transfer resistance at the interface compared to pristine ZnO in both solvents. The charge transfer resistance is a complex quantity that includes interface and bulk properties. However, since CuO is not in direct contact with the ITO electrode in the NT samples, it can be concluded that the interface between ZnO and CuO does not deteriorate the electrochemical activity of the sample. Under illumination the radii of the semicircle are smaller for the nanotree samples compared to the nanowire samples. This is an indication for the formation of a p-n hetero-junction that induces an additional potential under illumination and reduces the charge transfer resistance[143, 144].

Mott-Schottky (MS) analysis was performed to investigate the semiconducting properties of the nanotrees. MS analysis gives qualitative and quantitative information about the type of semiconductor, the donor concentration, and the flat band potentials. The Mott-Schottky equation has been used to analyze the data[145].

The variation of the capacitance of the space charge region versus the applied bias potential (MS plot) for the nanotrees is shown in Figure 4.11 (b) and 4.12(b) for pristine CuO, pristine ZnO, and ZnO/CuO nanotrees in the dark at 1 kHz with 0.1 M KCl and 0.1 M $BuNF_4$ in water and acetonitrile, respectively.

The positive slope of pristine ZnO is characteristic for the intrinsic n-type character of ZnO. MS analysis results in a donor density of $7.31 \times 10^{19}\ cm^{-3}$ in water which is comparable to previously reported values[139], and a flat band potential of -0.7417 V. The corresponding values for pristine CuO in water are $1.34 \times 10^{19}\ cm^{-3}$ which again compares well to published values[146], and the flat band potential is +0.3373 V.

The MS plot for the hetero-structured nanotrees shows the characteristic feature of a p-n junction with positive and negative slopes. It should be noted that in the

nanotrees the electrolyte is in contact with the CuO branches, as well as with the ZnO stem, which makes further analysis of the MS plot complicated. Values for the flat band potential are +0.4629 V and -0.5583 V. However, a direct comparison with the band gaps of the two materials would suggest that CuO and ZnO form a type II heterojunction at the interface.

In Figure 4.11 (c) and 4.12 (c), transient photocurrents of ZnO, CuO, and ZnO/CuO nanotrees in in 0.1 M KCl under 365-nm illumination at 0-V bias potential are shown. Photocurrents of pristine CuO and ZnO show the expected negative and positive photocurrent, respectively, according to their majority charge carriers. The addition of CuO branches to the ZnO nanowire stems leads to a two-fold increase of the photocurrent that is another strong indication for the formation of a p-n heterojunction between ZnO and CuO that leads to enhanced absorption and to the formation of spatially separated electrons and holes. Comparison of EIS measurements in the dark and under illumination supports this finding.

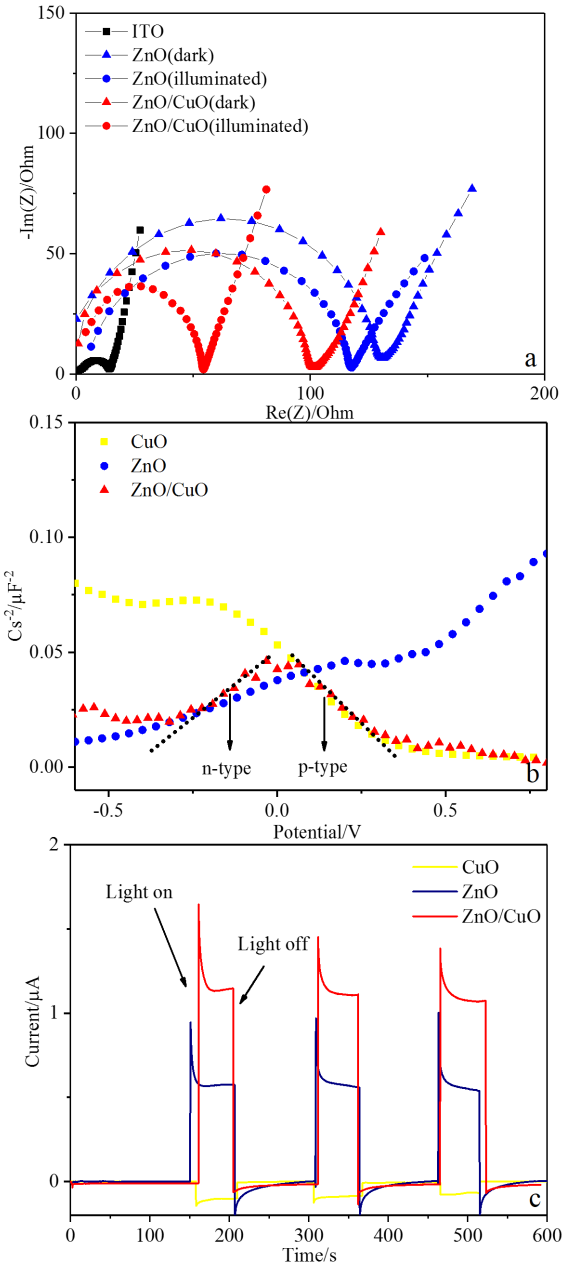

Figure 4.11: Nyquist plots measured in 1 mM $Fe(CN)_6^{3-}/Fe(CN)_6^{4-}$ in 0.1 M KCl aqueous solution (a), Mott-Schottky plots measured under dark condition in 0.1 M KCl aqueous solution at 1 kHz (b), transient photocurrents at 0-V bias potential in 0.1 M KCl aqueous solution under illumination in (c).

The stability of ZnO/CuO nanotrees was monitored by storing a sample in a glass bottle exposed to air and repeatedly recording the photocurrent in 0.1 M KCl aqueous solution under identical conditions (Figure 4.13). After 6-month the photocurrent decreased less than 5% with relative standard deviation (RSD) as 2.37%.

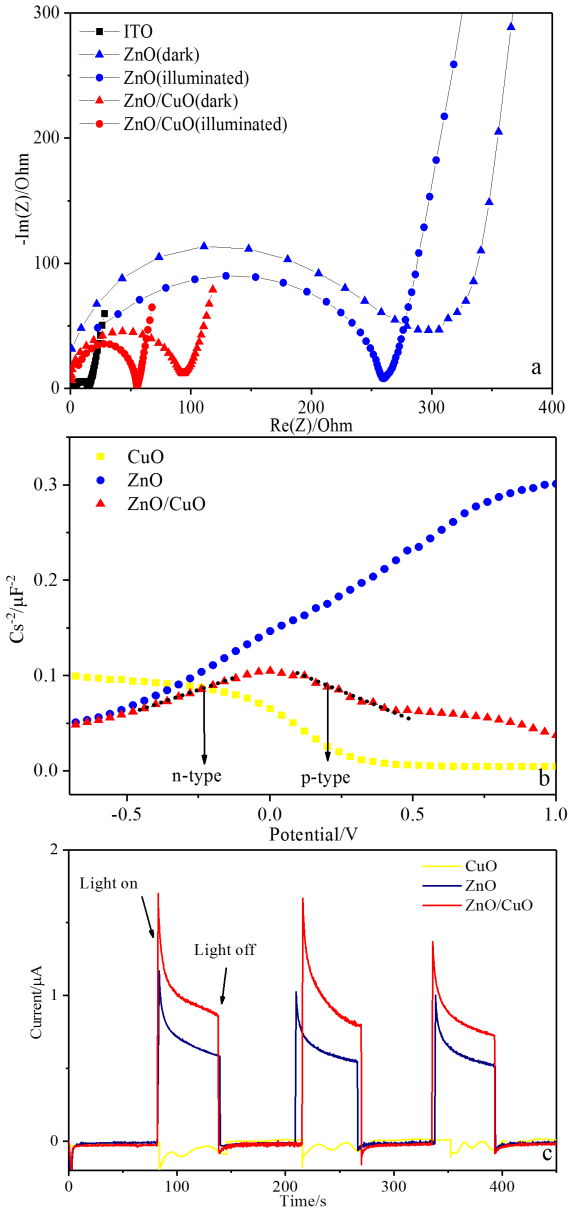

Figure 4.12: Nyquist plots measured in 1 mM ferrocene in 0.1 M $BuNF_4$ in acetonitrile (a), Mott-schottky plots measured under dark condition in 0.1 M $BuNF_4$ in acetonitrile at 1 kHz in (b), transient photocurrents at 0-V bias potential in 0.1 M $BuNF_4$ in acetonitrile under illumination in (c).

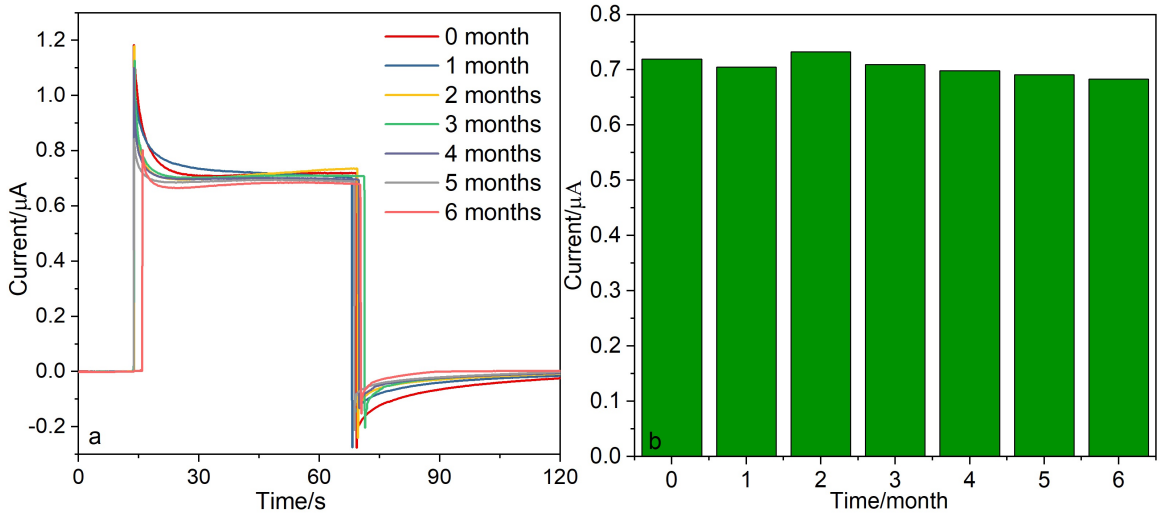

Figure 4.13: Transient photocurrent curves (a) and photocurrents (b) in 0.1 M KCl aqueous solution recorded in continuous months.

4.6 Photocatalytic Activity of ZnO/CuO Nanotrees

Toluene and acetic acid were used as model compounds in evaluating photocatalytic activity of ZnO/CuO nanotrees. Toluene has a high oxidation potential of 2.26 eV and it is hard to be oxidized in aqueous solution with electrochemical methods[147]. However, degradation of toluene has been shown to be very efficient in the presence of photo-generated electrons and holes[148, 149]. Acetic acid, on the other hand, is a common electrochemical active acid that has served as a model system for photodegradation. Therefore, toluene and acetic acid are used for evaluating photocatalytic activity of ZnO/CuO nanotrees.

The CV curve of acetic acid in 0.1 M KCl aqueous solution and toluene in 0.1 M $BuNF_4$/MeCN in the dark are shown in Figure 4.14 and 4.15. Both systems show very small dark current that was subtracted in the following measurements under illumination and no degradation of acetic acid or toluene in the dark is expected. Transient photocurrent measurements were taken at a series of concentrations of acetic acid in 0.1 M KCl aqueous solution with 0-V bias potential and with the background current subtracted (Figure 4.16 (a)).

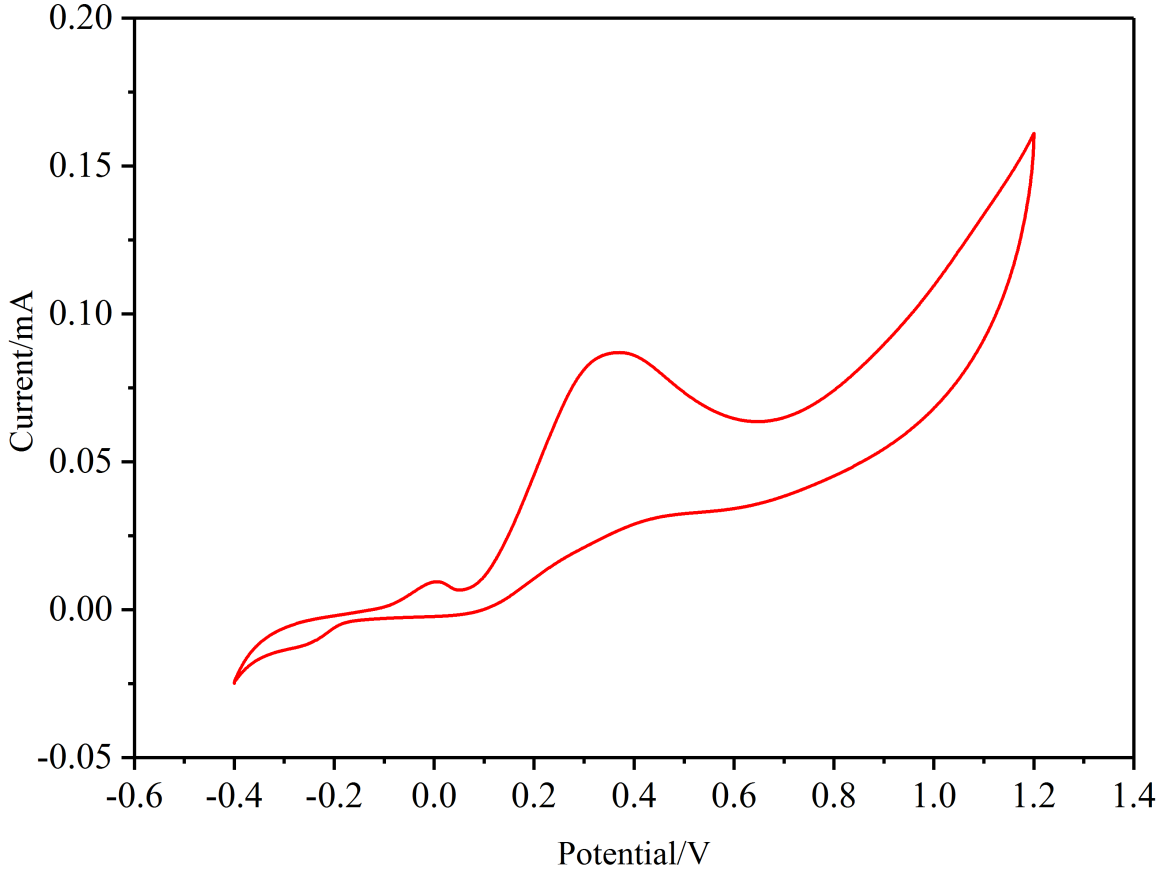

Figure 4.14: CV curve of 1 mM acetic acid in 0.1 M KCl aqueous solution.

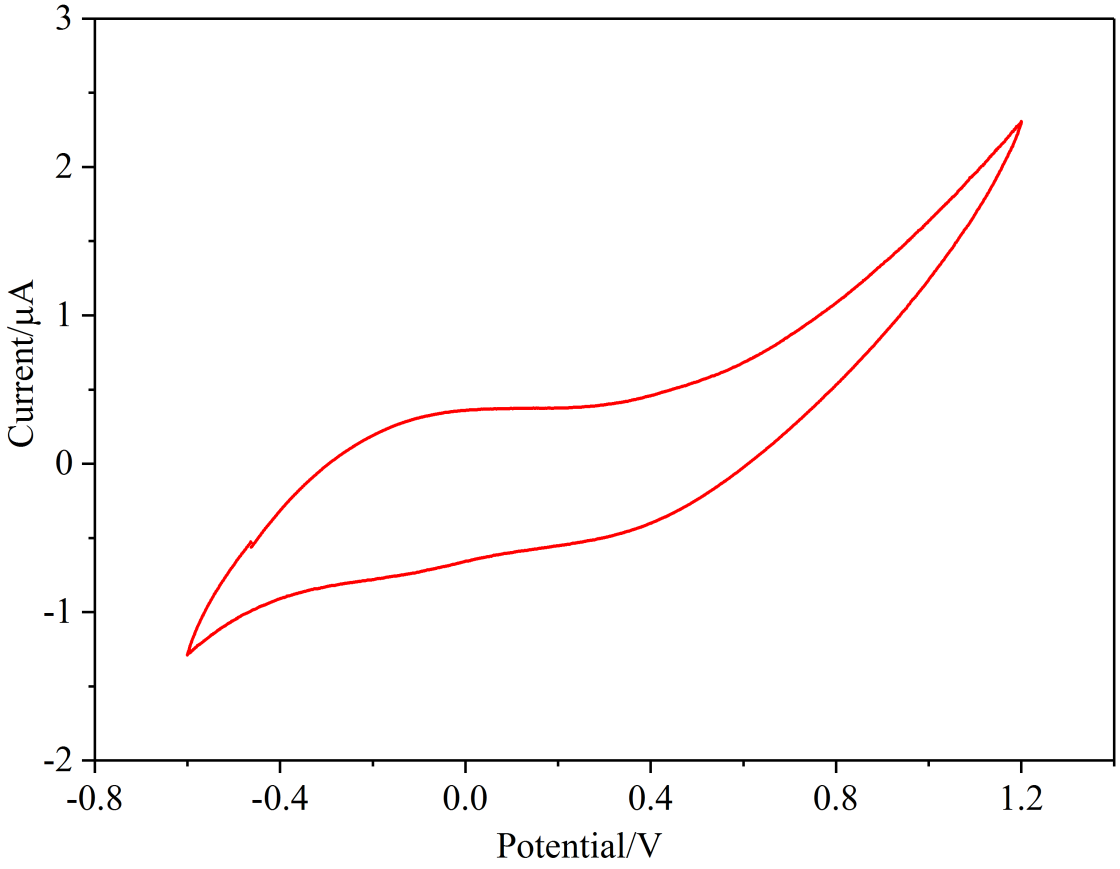

Figure 4.15: CV curve of 1 mM toluene in 0.1 M $BuNF_4$ in acetonitrile.

Three repeated transients were recorded. The first was used for calibration, the other two to ensure that equilibrium was established. The current at the end of the 50-s illumination period was plotted as a function of the concentration in Figure 4.16 (b) and (d).

The current I was fitted as a double logarithmic function of the concentration C for low concentrations ($0 < C \leq 2.08\ \mu M$) : $\log I = A \log C + B$, and resulted in A=0.156 and B=0.352. For high concentrations above 2.08 μM a linear function, $I = D{*}C{+}E$, was fitted and resulted in D=0.216 and E=2.12. The same procedure applied to the photocurrent measurements of toluene yielded A=0.168 and B=0.06067 below 5μM, and D=0.00933 and E=1.4492 above 5 μM. The transition from exponential to linear relationship between I and C at different concentration ranges confirms that heterogeneous photo-catalysis is established successfully and the photocurrent is only related to the concentration of model molecules rather than the efficiency of catalyst. To our knowledge, this catalysis process can be explained by the Langmuir-Hinshelwood mechanism for toluene and acetic acid. Langmuir-Hinshelwood mechanism for heterogeneous photo-catalysis involves target molecule specific adsorption, hole-electron separation of photocatalytic semiconductors, and desorption of products[150]. At low concentration of the analyte, the interface concentration is considered very small and the reaction rate is limited by the bulk concentration, resulting in first order kinetics. At high concentration of analyte, on the other hand, the reaction shows zero order kinetics and the reaction rate is a constant limited only by the constant number of reaction sites on the surface.

The photo-electrochemical degradation of toluene and acetic acid shows again that the synthesized tree-like hetero-nanostructures with exposed CuO branches combine efficient charge separation due to the p-n heterojunction with the photocatalytic activity of CuO.

For comparison, transient photo-current measured with non-treelike randomly oriented ZnO/CuO composites that were grown without the seeding step is shown in Figure 4.17. The average photo currents of non-tree samples are 50% smaller in aqueous

solution and 30% smaller in acetonitrile solution, respectively, to tree-like samples.

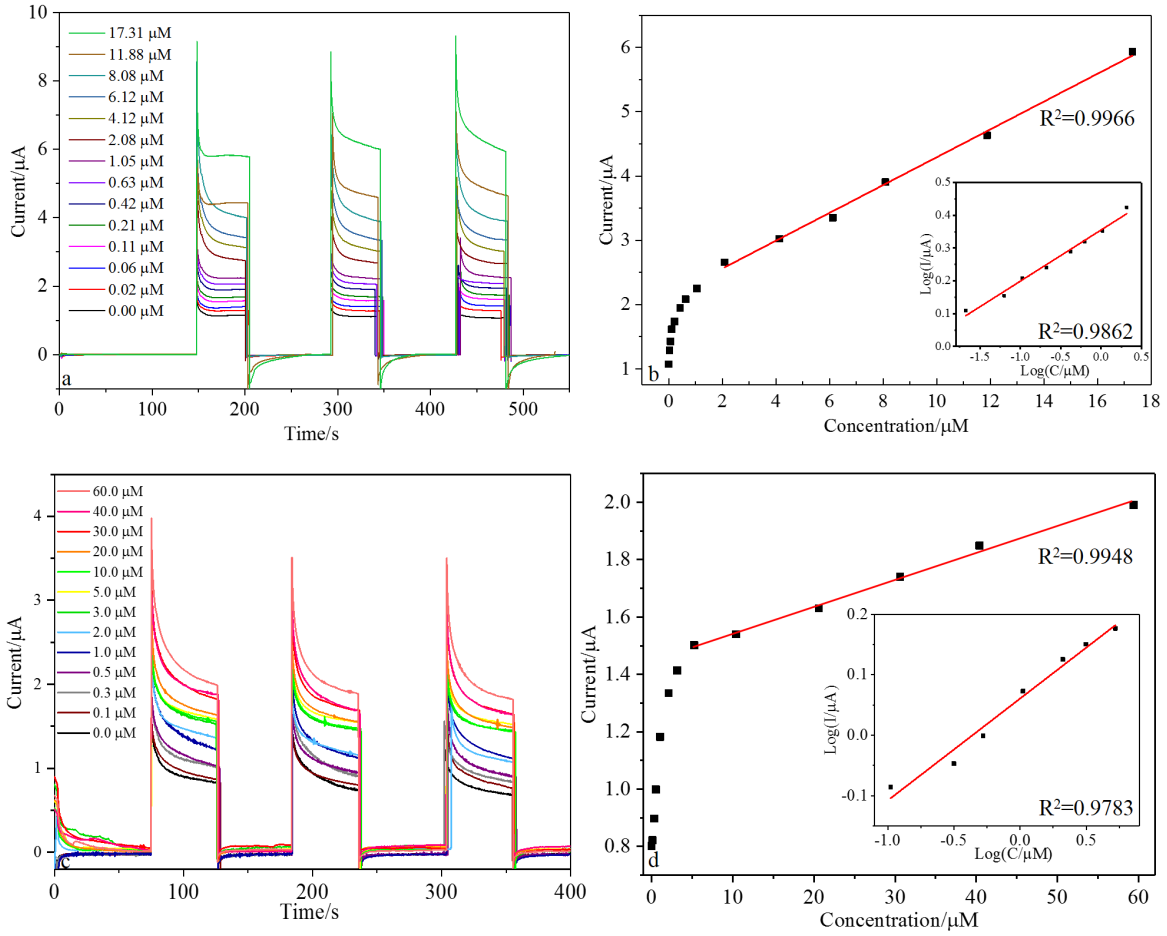

Figure 4.16: Transient photocurrents of acetic acid in 0.1 M KCl aqueous solution in (a). I vs. C curve for (a) in (b), inset: fit curve in the concentration range from 0 to 2.08 μM. Transient photocurrents of toluene in 0.1 M $BuNF_4$in acetonitrile in (c). I vs. C curve for (c) in (d), inset: fit curve in the concentration range from 0 to 5 μM.

4.7 Conclusion

A new synthetic route was developed for the fabrication of novel tree-like nanostructures with ZnO nanowires as stems and CuO nanorods as branches. The morphology of the structure was characterized with SEM, XRD, and XPS, and compared to nanostructure obtained by an established growth method. The electrochemical and photoelectrochemical properties were investigated in acetonitrile and water solutions. For both systems, nanotrees show high conductivity, fast carrier transport and effective electron-hole separation. Therefore, ZnO/CuO nanotrees are a promising semiconductor material for future applications in solar energy conversion devices, photo-catalysis and photocatalytic sensors.

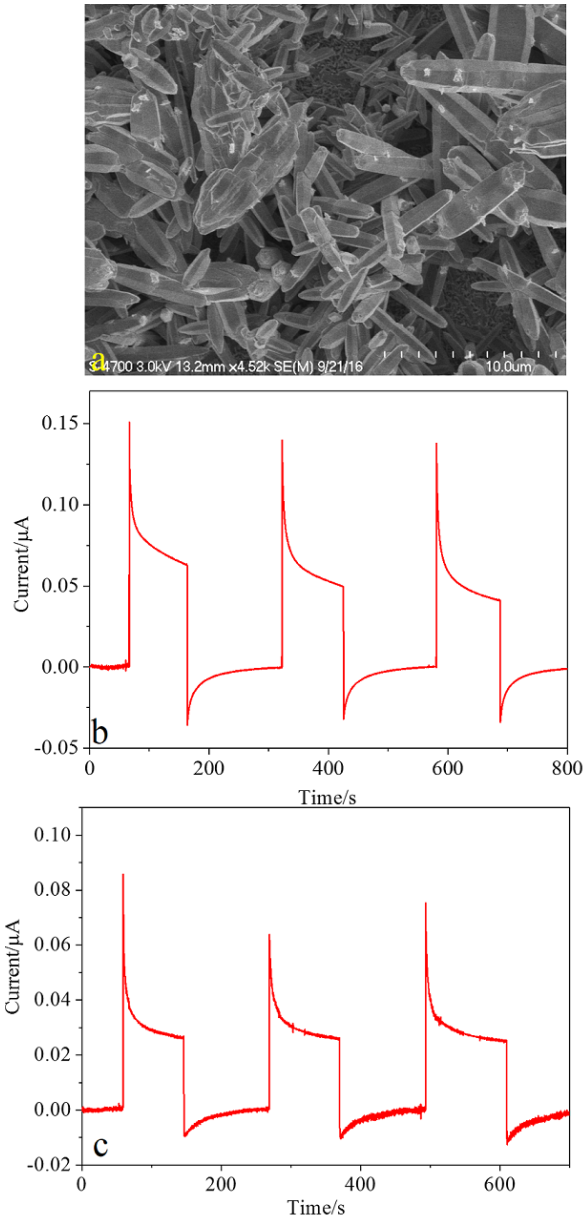

Figure 4.17: a: SEM image of nontree structure of ZnO/CuO prepared without seeding process; b: transient photocurrent in 0.1 M KCl aqueous solution; and c:transient photocurrent in 0.1 M $BuNF_4$ in acetonitrile.

Chapter 5

ENERGY BAND ARCHITECTURE OF HIERARCHICAL ZNO/AU/CU_XO NANOFOREST BY MIMICKING NATURAL SUPERHYDROPHOBIC SURFACES

5.1 Introduction

As mentioned in Chapter 1, superhydrophobic surface may have self-cleaning capability[24]. Devices based on non-toxic "green" materials are promising in solar cells and other devices in real environment since device leftover will not cause potential pollution[31]. Similarly to ZnO, Cu_2O is also considered as an abundant eco-friendly semiconductor so it would be proper building blocks for hierarchical structure in photoelectrochemical catalysis.

Cu_2O is a p-type direct-band-gap semiconductor[12]. It shows potential high photovoltaic conversion and photocatalytic properties. Cu has electron configuration as $[Ar]3d^{10}4s^1$. Like ZnO, Cu^+ has $[Ar]3d^{10}$ configuration, but Cu^{2+} has $[Ar]3d^9$. This $3d^{10}$ orbital structure means that Cu_2O has VB involving only d orbitals and CB involving sp hybridized orbitals. This dissimilarity between VB and CB leads to a d to sp orbital transition while electrons and holes are recombining, leading to low probability of recombination and long lifetime of excitons[43, 44, 151]. This is the reason why Cu_2O is not as stable as CuO in wet air, but it still causes much attention.

ZnO/Cu_2O has been investigated deeply because the pn heterojunction between ZnO and Cu_2O shows dramatic enhancement on photoelectrochemical catalysis[152, 153, 154, 155] and photovoltaic conversion which is predicted as 18% [156].

However, the lattice mismatch between ZnO and Cu_2O is estimated as 25% according to a=3.2495 Å of ZnO wurtzite structure and a=4.2696 Å of Cu_2O cubic structure. The large lattice mismatch between ZnO and Cu_2O results in high resistance

and poor electron mobility across the heterojunction ZnO/Cu_2O, which limits the performance of ZnO/Cu_2O devices[157, 158].

Therefore, the main challenges for improving the performance of ZnO and Cu_2O heterojunction are reduction of the lattice mismatch and enhancement of electron transfer.

The first factor effecting lattice mismatch is deposition sequence. Akimoto et al. found that the device fabricated by depositing ZnO first and then coating Cu_2O shows better crystallization and performance than the reversed one[159]. This is because that [0001]-oriented ZnO guides the growth of the (111) in Cu_2O. The similar stacking between (002) and (111) encourages lattice matching and decreases the defect formation[157].

On the basis of this fact, when designing hierarchically structured ZnO/Cu_2O, we should have ZnO as first-prepared stems and Cu_2O as branches. With the assistance of vertically-aligned structure, electron transfer pathways can be improved by removing electrons fast.

The second strategy to decrease the lattice mismatch is to induce another material to help move charge carriers. CuO is proved to reduce lattice mismatch between ZnO and Cu_2O[122] and improve photocatalysis performance compared to bare CuO or Cu_2O[160, 161, 153, 146]. Au has been evidenced as the best material for creating the best contact to Cu_2O without reducing it to Cu[162, 163]. In addition, noble metals have been confirmed to improve electron transfer across the heterojunction and enhancing photocatalytic performance[164, 165, 166].

In this chapter, ZnO/Au/Cu_xO is synthesized in hierarchical nanoforest, with ZnO vertically-aligned array as nanostems and Cu_xO as nanobranches. Since the hierarchical structure may have superhydrophobic property, which features self-cleaning function, Cu_2O may be more stable against water-assisted oxidation and ZnO/Au/Cu_xO nanoforest may show better stability.

5.2 Nanogold-catalyzed Electrodeposition of Cu_xO Nanobranches

The fabrication and growth mechanism of vertically-aligned ZnO nanowires were discussed in chapters 2 and 3[69]. The schematic diagram of the experimental set-up for the synthesis and the cyclic voltammogram of electrodeposition are shown in Figure 5.1 (a) and (b), respectively. The dimensions of two levels of structuring are observed from SEM images of ZnO/Au/Cu_2O nanoforest with different resolutions and angles shown in Figure 5.1 (c-f). ZnO nanowires are 5 μm long and 100 nm thick and Cu_xO nanobranches are 100-200 nm long and 10-20 nm thick. 5-nm gold cannot be resolved via this SEM.

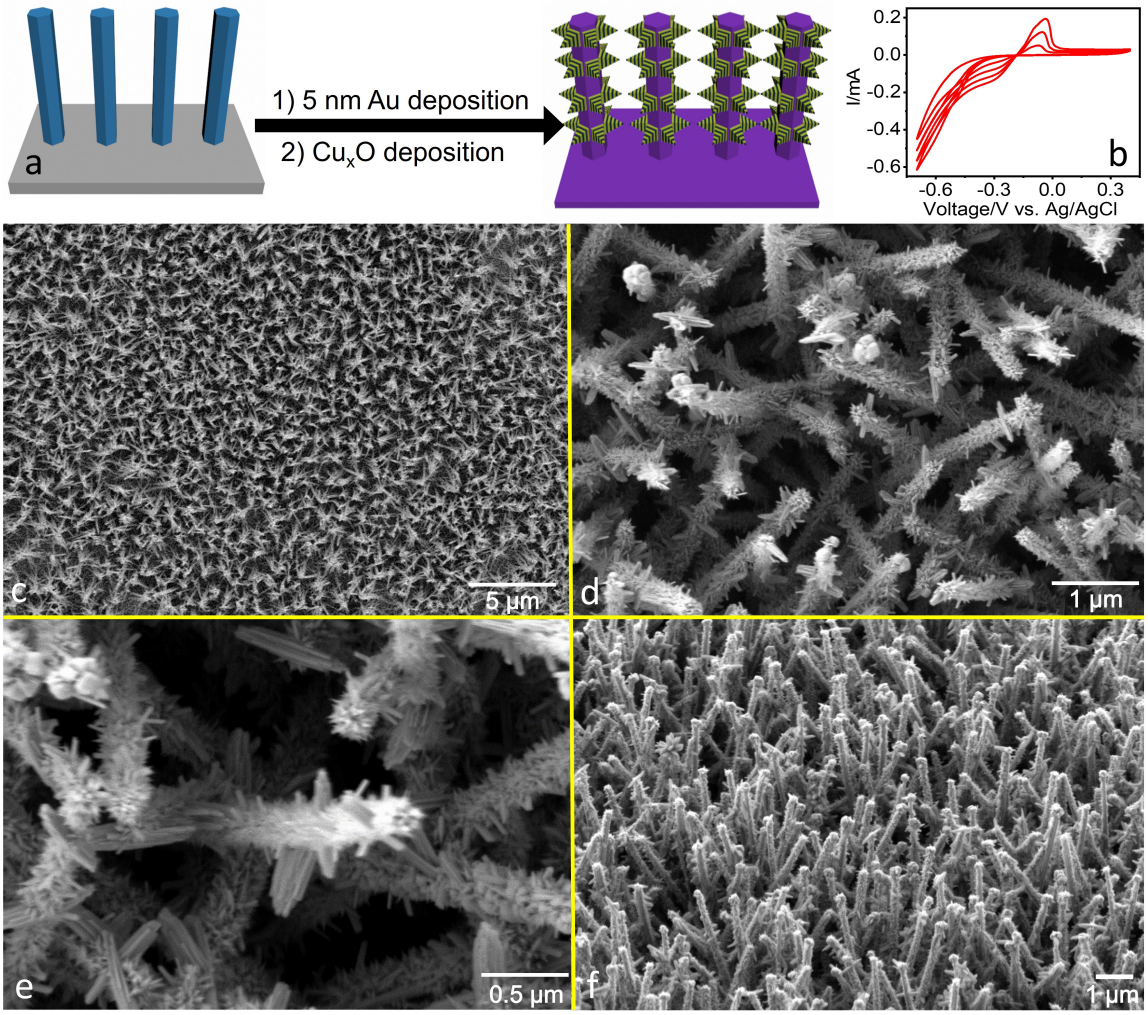

Figure 5.1: Scheme of synthesis of ZnO/Au/Cu_xO nanoforest in (a) and the CV curves of electrodeposition of Cu_xO in (b). SEM images of top view (c-e) and 54° angle view (f) of ZnO/Au/Cu_xO nanoforest.

Alkaline Cu(II) lactate was used as the precursor for electrodeposition, since ZnO dissolves in acids easily and Cu_2O may exist as n-type semiconductor deposited at acidic solutions[167]. The growth mechanism of Cu_2O in alkaline Cu(II) lactate solution has been investigated previously[167, 168, 169]. The cyclic voltammetric deposition should start from the reverse potential sweep, so that deposition of Cu_2O occurs first followed by its oxidation. In negative direction scan, Cu^{2+} is reduced to Cu^{+}, which leads to cathodic peaks at around -0.3 V (eq. 5.1). Because of excess OH^{-} groups at high pH, Cu^{+} would be precipitated as CuOH (eq. 5.2) instead of being reduced to Cu(0) further. CuOH is hydrolyzed immediately to Cu_2O on the electrode (eq. 5.3). In positive potential sweep direction, Cu_2O is partly oxidized to CuO with the assistance of OH^{-}[170].

$$Cu^{2+}(\text{in complex form of } \mathrm{CuL}_2^{2+}) + 2\ e^- \rightarrow Cu^+ \tag{5.1}$$

$$Cu^+ + OH^- \rightarrow CuOH \tag{5.2}$$

$$2\ CuOH \rightarrow Cu_2O + H_2O \tag{5.3}$$

$$Cu_2O + 2\ OH^- \rightarrow 2\ CuO + H_2O + 2\ e^- \tag{5.4}$$

In this process, the concentration of lactic acid and the pH of the solution are the key parameters. Lactic acid is the complexing agent for Cu^{2+} to prevent Cu^{2+} from forming $Cu(OH)_2$ at high pH. In terms of pH, both reduction and oxidation consume OH^- groups so excess OH^- groups guarantee that Cu^+ deposits at the electrode immediately instead of being reduced to photoelectrochemically inert Cu. In addition, the morphology of Cu_2O can be affected by the pH value. In Golden's article[171], at pH of 9, Cu_2O grows along the [100] orientation to form cubic pyramids, while at extremely high pH around 12, it grows along the [111] orientation, which is the triangular planar phase of octahedral structure [77] and has the ability to grow vertically on ZnO. To look into the pH effect, SEM images of ZnO/Cu_xO prepared at pH of 8, 9, and 10 are shown in Figure 5.2. At pH of 8, Cu is the major product while at pH of 9 Cu_xO can hardly reach the desired length of about 100 to 200 nm, however, at pH of 10, ZnO is damaged while Cu_xO is still formed in large cubes. This is because ZnO will dissolve in strong alkaline solutions to form $Zn(OH)_4^{2-}$ at high temperature. As a result, even if higher pH condition could result in better quality of Cu_xO nanowires, it would be hard to maintain ZnO morphology, so most Cu_2O electrodeposition was reported at lower pH[172, 173] or with OH-free organic solvents like DMSO[174].

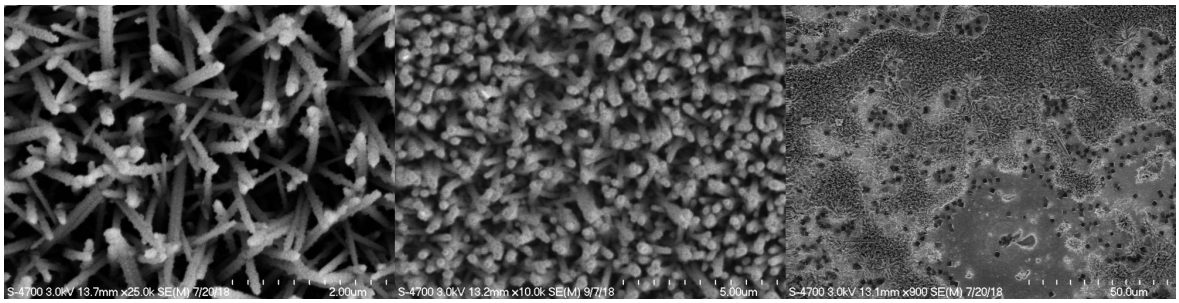

Figure 5.2: SEM images of ZnO/Cu_xO prepared at pH=8 (left), pH=9 (middle), and pH=10 (right).

Another concern is the controlled epitaxial growth of Cu_xO crystal. Generally, Cu_2O tends to develop into extensive cubic structure rather than in one dimensional-oriented nanobranches in electrodeposition[167, 168, 170]. The diameter of ZnO nanowires is around 100 nm (in Figure 5.1). This means that given ZnO could survive in solutions with pH of 10, the ZnO nanowires might be fully covered by Cu_xO nanocubes which have larger diameter than that of ZnO nanowires.

In order to synthesize (111)-oriented Cu_xO nanorods at pH of 11 instead of nanocubes at low pH values, the ZnO was coated with 5 nm thick gold via evaporator. It can be seen that the morphology of ZnO nanowires was still maintained at pH of 11 in KCl solution, shown in Figure 5.3 (a). The diameter of gold nanoparticles was confirmed as 5 - 10 nm with TEM shown in Figure 5.3 (b).

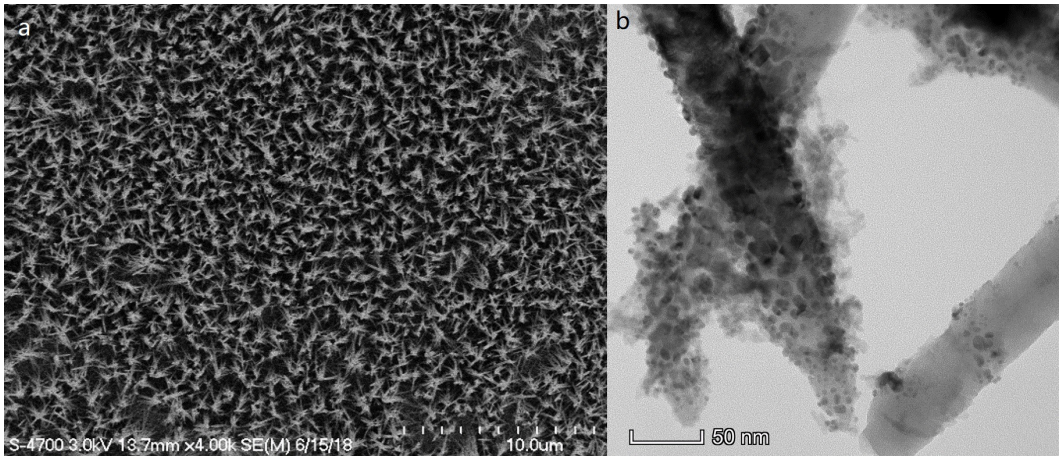

Figure 5.3: SEM image of gold-coated ZnO (a) and TEM image of ZnO/Au/Cu_xO (b).

SEM images of ZnO/Au/Cu_xO prepared at pH of 10 and 11 are shown in Figure 5.4. At pH of 10, Cu_xO are in cubic structure (Figure 5.4) with length of around 50 nm while at pH of 11, Cu_xO are in nanobranch structure with length of around 100 nm and diameter of around 10 - 20 nm (Figure 5.4, and Figure 5.1).

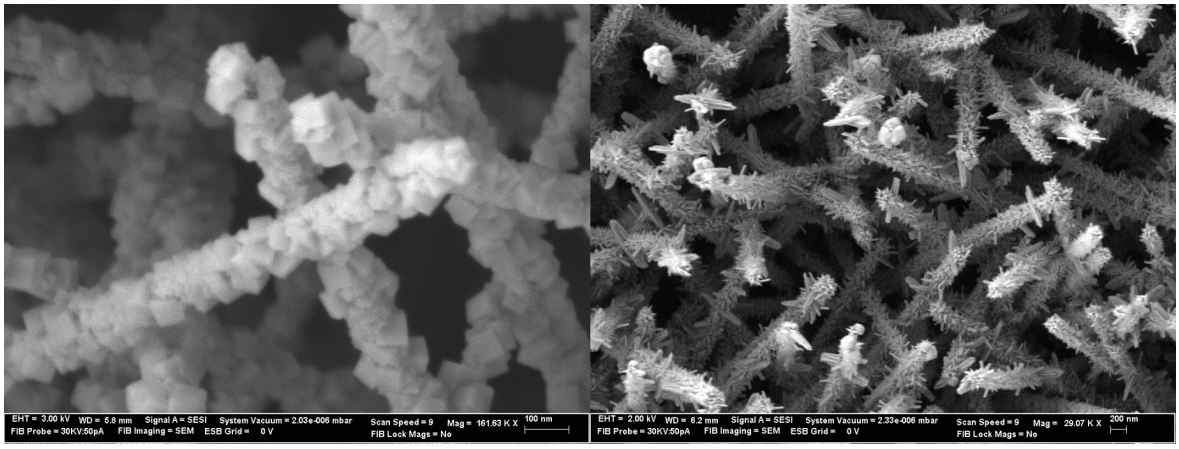

Figure 5.4: SEM images of ZnO/Au/Cu_xO prepared at a pH of 10 (left) and of 11 (right).

To determine if gold affects the crystallization of Cu_xO in Cu_xO electrodeposition, a ITO glass was covered to one half by a tape when doing gold deposition. It was used as a substrate for electrodeposition of Cu_xO deposited at a pH of 11. SEM images are shown in Figure 5.5. Gold results in a Cu_xO crystal size of less than 100 nm and octahedral structure in Figure 5.5 (b), much smaller compared to the size of Cu_xO on the ITO surface that is about 200 nm in Figure 5.5 (a). Gold may catalyze the growth of (111) in Cu_xO electrochemical deposition. This catalysis is attributed to the lattice match between Cu_2O (111) and the Au (111) phases [175, 176], which is also confirmed with XRD data discussed in next section.

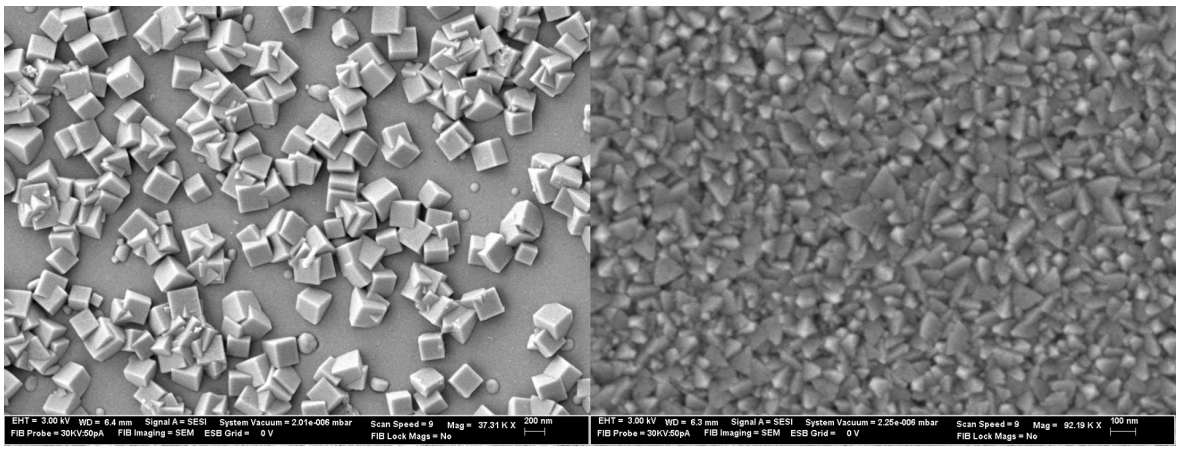

Figure 5.5: SEM images of Cu_xO without Au coating (left) and with Au coating (right).

5.3 Crystal Structure and Composition of ZnO/Au/Cu_xO Nanoforest

XRD in Thin-film lynxEye 0D mode was used to identify the crystal structure, since the ZnO/Au/Cu_xO nanoforest is about several μm thick and scattering signal from amorphous glass substrate is disruptive. The XRD spectra of ZnO, Cu_xO, Cu_2O, and ZnO/Au/Cu_xO nanoforest are shown in Figure 5.6. Generally, no metallic Cu signal shows up, so the electrodeposition technique above controlled the composition of Cu_xO successfully and metallic Cu formation was avoided. Wurtzite ZnO was identified by the presence of (100), (002), (101), and (102) peaks [JCPDS file No.36-1451] and the strong (002) peak represents vertically-aligned hexagonal nanorod array along the [0001] growth orientation, shown in Figure 5.6 (a). To get a better resolution of the gold signal, A ZnO/Au/Cu_xO nanoforest with 20 nm gold coating and 2 cycles of CV deposition was measured. Gold cubic crystal structure was determined by the (111) and (200) peaks [JCPDS file: 04-0784] shown in Figure 5.7. In the TEM image ZnO/Au/Cu_xO nanoforest in Figure 5.3, Au quasi-spherical particles were imaged in darker contrast with the diameter of 5-10 nm, and ZnO stem and Cu_xO branches are in lighter contrast. In bright field TEM imaging, diffraction contrast of heavy metal shows much darker color than that of light atoms[177]. This is because that scattering is stronger for heavier atoms[178] and electron transmission through heavier atoms is reduced to image in bright field.

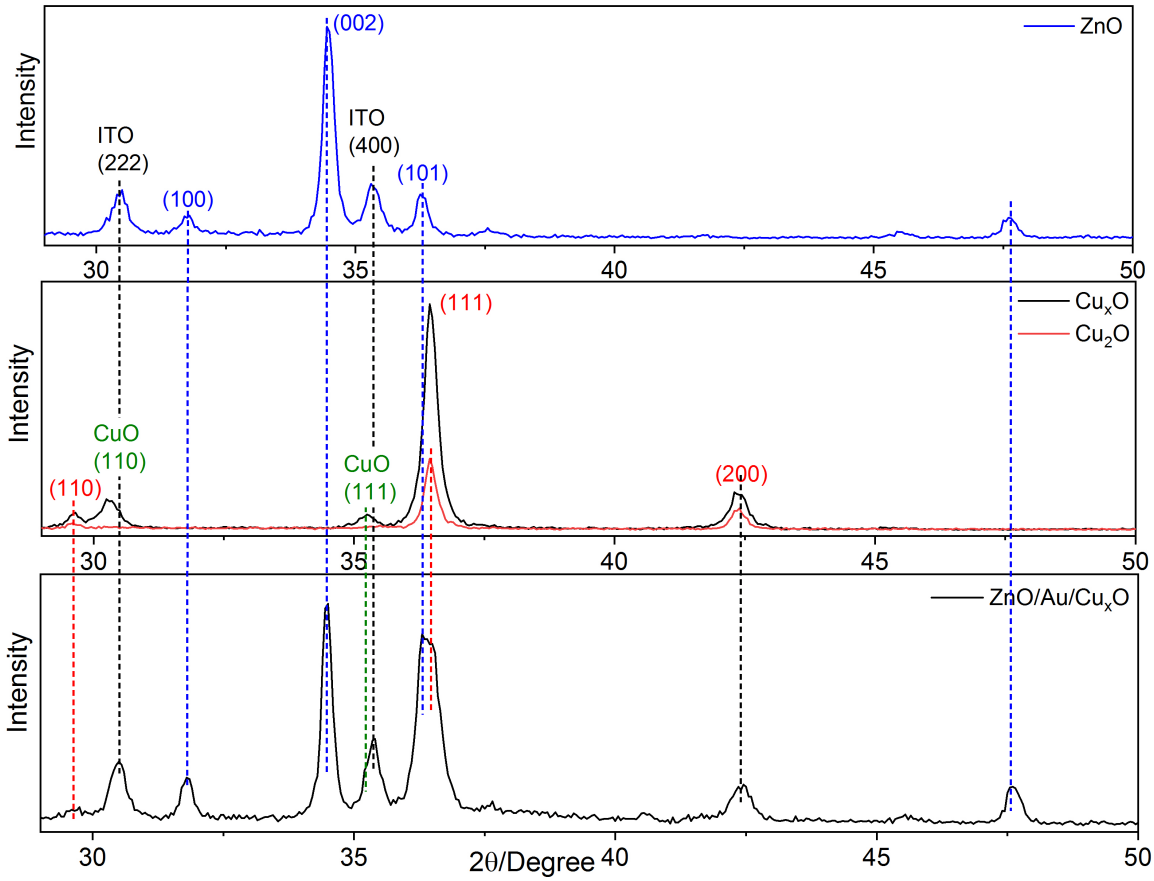

Figure 5.6: XRD spectrum of ZnO/Au/Cu_xO nanoforest in LynxEye 0D mode.

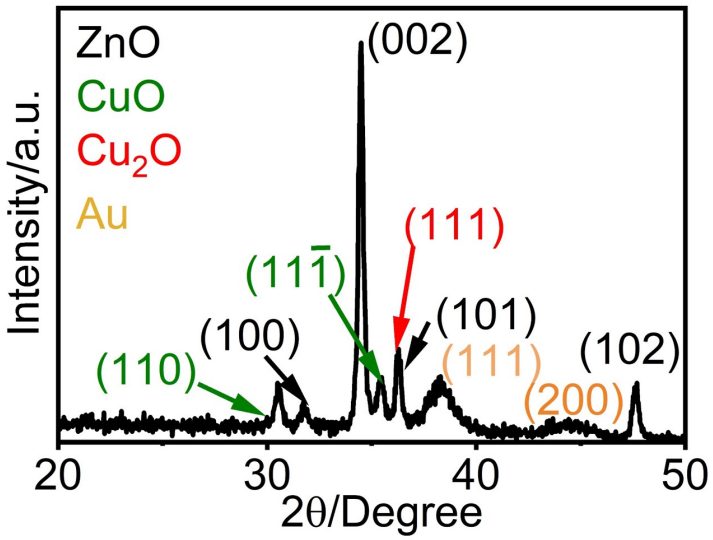

Figure 5.7: XRD spectrum of ZnO/Au/Cu_xO with 20-nm gold coating.

In Figure 5.6 (b), Cu_xO consists of monoclinic CuO involving (110) and $(11\bar{1})$ peaks [JCPDS file No. 45-0937] and Cu_2O involving (110), (111), and (202) peaks [JCPDS file: 05-0667]. In Figure 5.6 (c), The peaks of ZnO (101) and Cu_2O are overlapped but they can still be distinguished by comparing the peaks to pristine ZnO and Cu_xO. It is seen that Cu_2O in Cu_xO is in [111] oriented[167]. Cu_2O is primitive cubic with space group Pn3m, with the lattice constant (a) of 4.2830 Å in (111) while gold (111) has the lattice constant (a) of 4.0672 Å with space group Fm3m[179, 180]. The lattice mismatch between Cu_2O and gold is calculated as 4.8% with eq. 5.5, which is considered as lattice-matched (<5%) for epitaxial growth[181, 182]. This result supports the catalytic behavior of gold in Cu_2O deposition.

$$\text{Lattice mismatch} = \frac{\text{lattice constant}_{film} - \text{lattice constant}_{substrate}}{\text{lattice constant}_{substrate}} \times 100\% \qquad (5.5)$$

The XPS measurements of $ZnO/Au/Cu_xO$ nanoforest shown in Figure 5.8 were calibrated with with C 1s (C-C binding) (285.0 eV)[129] as charge correction reference. Zn^{2+} in the wurtzite ZnO structure was identified by peaks at Zn $2p_{1/2}$, 1044.67 eV and Zn $2p_{3/2}$, 1021.69 eV, shown in Figure 5.8 (a). The peak splitting and fitting of O 1s is controversial in hydrothermal multi-semiconductor materials because the contributions may come from the components, defects[132], or hydroxyl groups that cannot be removed completely[130]. In $ZnO/Au/Cu_xO$, oxygen source should be attributed to hydroxyl groups attached to metal oxides, O^{2-} in ZnO, and O^{2-} in Cu_xO, so the O 1s peak was fitted by three Gaussian peaks shown in Figure 5.8 (b).

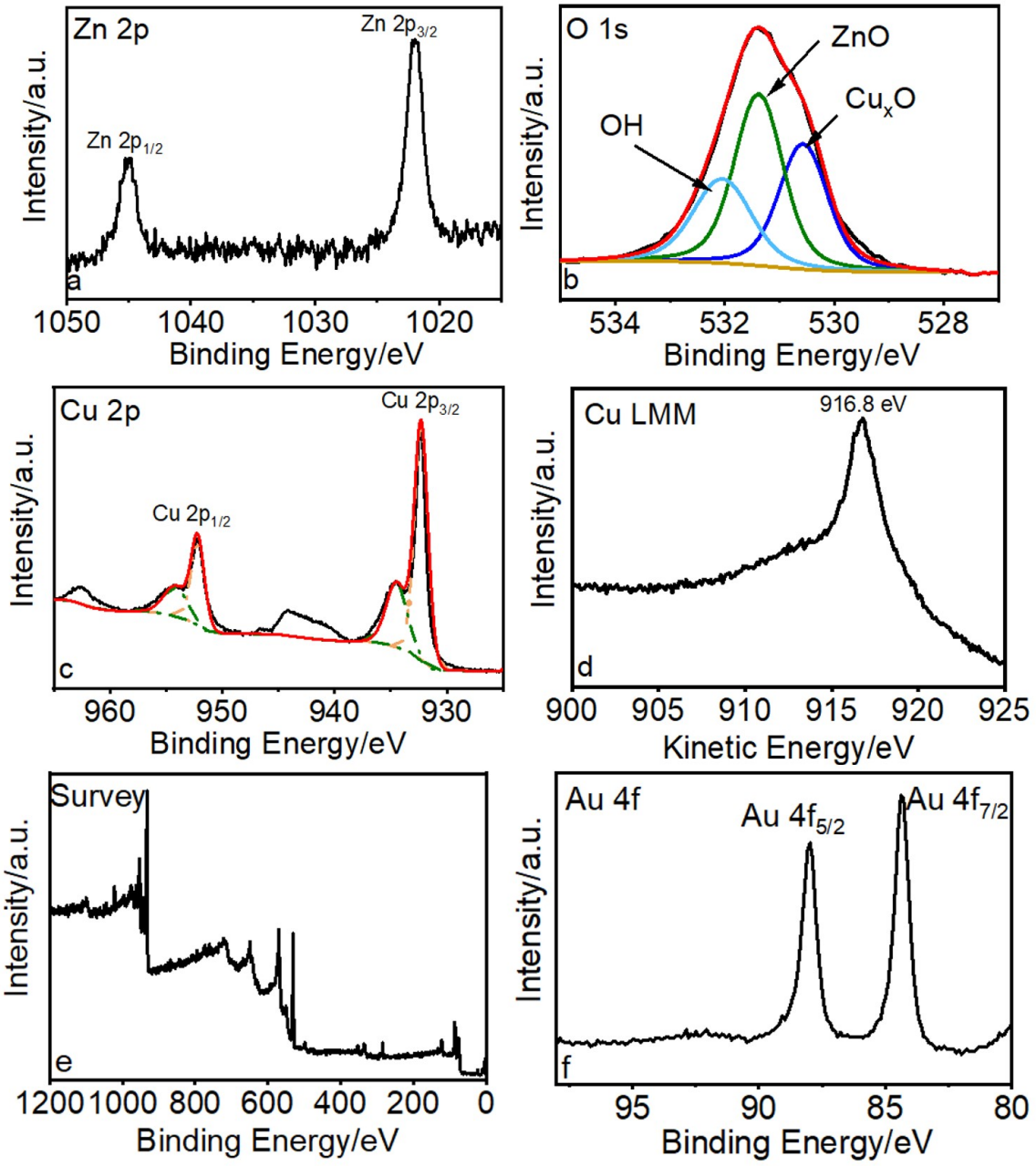

Figure 5.8: XPS spectrum of ZnO/Au/Cu_2O nanoforest (f) and high-resolution spectra of Zn 2p, O 1s, Cu 2p, Cu LMM, and Au 4f peaks, respectively(a-e).

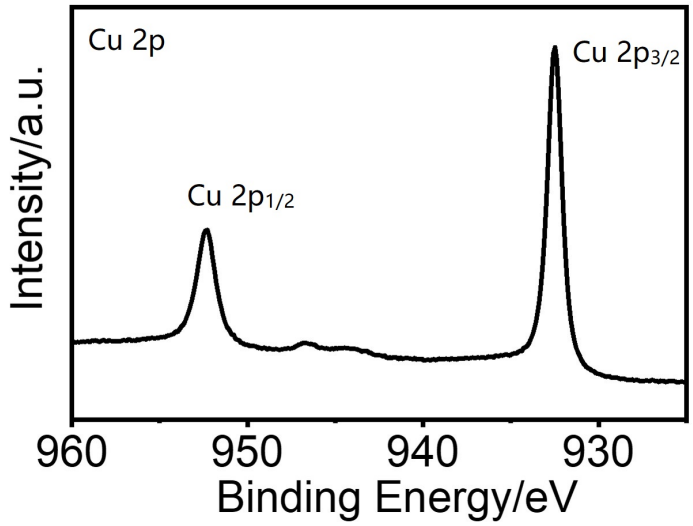

Figure 5.9: Cu 2p XPS spectra of Cu_2O nanocubes.

The Cu 2p region is shown in Figure 5.8 (c). Cu^{2+} is more positively charged compared to Cu^{+} so Cu(II) in CuO shows peaks of Cu $2p_{1/2}$ (954.11 eV) and Cu $2p_{3/2}$ (934.42 eV) at higher binding energy region while Cu_2O displays Cu $2p_{1/2}$ (952.12 eV) and Cu $2p_{3/2}$ (932.10 eV)[129]. Peaks at 962.69 eV and 943.87 eV are satellite peaks from CuO, which are not observed in potentiostatically-electrodeposited Cu_2O shown in Figure 5.9.

Since the peak positions of Cu_2O are close to peaks of metallic copper, Cu LMM was measured (Figure 5.8 (d)) and the absence of metallic copper was confirmed. Cu 2p area scan of the whole slide was done and the uniformity of Cu_xO coating was verified shown in Figure 5.10.

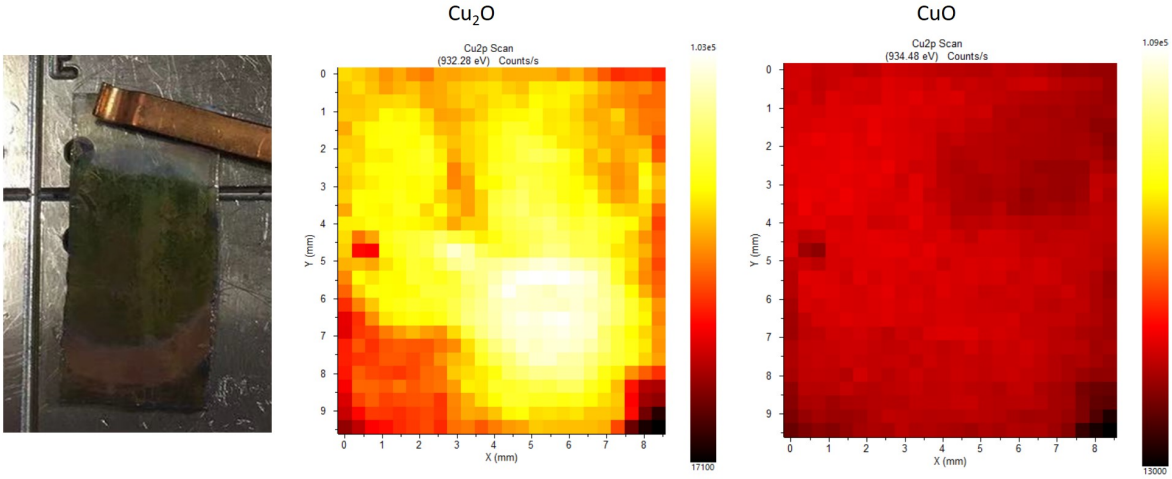

Figure 5.10: XPS Cu 2p area scan of Cu_2O of ZnO/Au/Cu_xO with photo of the selected area (left), Cu $2p_{3/2}$ of Cu_2O (middle) and CuO (right).

5.4 Energy Band Diagram

The energy band alignment at the p-n junction significantly affects electron transfer efficiency and photovoltaic conversion performance. The band alignments of ZnO/Cu_2O and ZnO/CuO have been discussed [183, 184, 154, 185], however, the band diagram of $ZnO/Au/Cu_xO$ is still not clear. Therefore, it is substantial to figure out the interface band alignments based on experimental data.

To draw the entire band diagram, the valence band maximum (VBM) values for individual semiconductors can be achieved precisely with XPS shown in Figure 5.11 and valence band offset (VBO) and conduction band offset (CBO) can be calculated from XPS data of the $ZnO/Au/Cu_xO$ nanoforest[186, 187, 188, 189]. Band gap values of semiconductors can be estimated from UV-Vis spectra and PL spectra shown in Figure 5.12.

In VBM calculation, Fermi level (E_F) is set at the binding energy as 0 eV and the valence band edges with fitted linearly as well as the horizontal background, so the intersection is the approximate VBM value shown in figure 5.11. The VBM values of pure Cu_xO and ZnO synthesized under the same conditions are 0.43 eV and 2.61 eV, respectively, which corresponds well with literature values[183, 190, 191, 188].

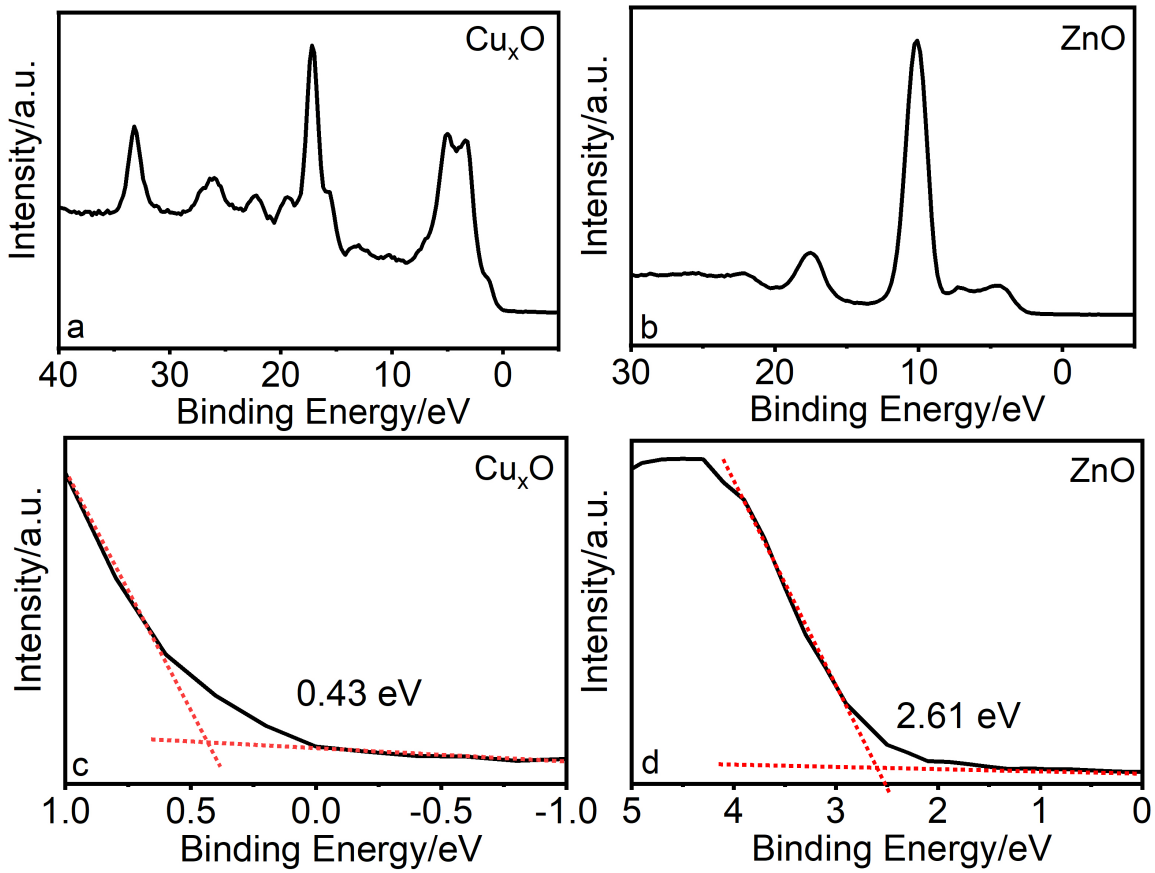

Figure 5.11: XPS spectra of Cu VBM in Cu_xO (a and c), and Zn VBM in pure ZnO(b and d).

VBO consists of three terms shown in eq. 5.6. The first term on the right side in eq. 5.6 represents the energy difference between Zn $2p_{3/2}$ and Cu $2p_{3/2}$, which was obtained from XPS data in Figure 5.8. The second term is the energy difference between Cu$2p_{3/2}$ and Cu VBM in pure Cu_xO while the third term is that in pure ZnO. It is noteworthy that Cu_xO is an alloy semiconductor with Cu_2O as majority component, the overall contribution of Cu 2p is mainly considered from Cu $2p_{3/2}$ from Cu_2O according to previous papers[192, 193]. The VBO is calculated as 2.23 eV with detailed steps shown in eq. 5.6.

$$\begin{aligned}\Delta E_V^i &= \left(E_{Zn2p}^{ZnO}(i) - E_{Cu2p}^{Cu_xO}(i)\right) + \left(E_{Cu2p}^{Cu_xO} - E_{VBM}^{Cu_xO}\right) - \left(E_{Zn2p}^{ZnO} - E_{VBM}^{ZnO}\right) \\ &= 1021.69 - 932.10 + 932.69 - 0.43 - 1021.60 + 2.61 \\ &= 2.23\ eV\end{aligned} \tag{5.6}$$

$$\Delta E_C = E_g^{ZnO} - E_g^{Cu_xO} - \Delta E_V \tag{5.7}$$

Calculation of CBO requires the knowledge of the band gap values so UV-Vis spectroscopy was conducted. UV-Vis transmittance spectra of Au, pristine Cu_xO, pristine ZnO, and ZnO/Au/Cu_xO nanoforest on ITO substrates are shown in Figure 5.12 and band gap values are retrieved with K-M method and detailed calculation has already been described in chapters 3 and 4[101, 69, 68]. ZnO/Au/Cu_xO nanoforest consists of the band gap of ZnO at 3.37 eV and the overall band gap of Cu_xO at 2.15 eV. These two values are applied in CBO calculation in eq. 5.7, so CBO is calculated as -1.01 eV. Combining all information, the band diagram after contact was drawn shown in Figure 5.13. This diagram was used in estimating electron transfer patterns in later section.

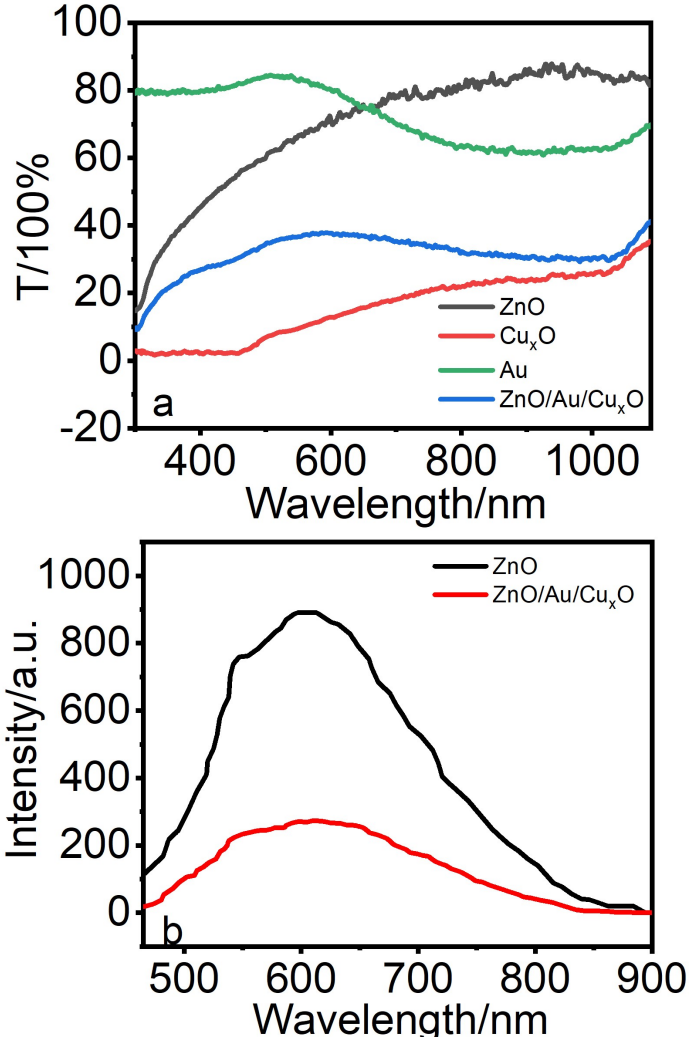

Figure 5.12: (a): UV-Vis transmittance spectra of Au, pristine Cu_xO, pristine ZnO, and ZnO/Au/Cu_xO nanoforest on ITO substrates and (b): PL spectra of ZnO and ZnO/Au/Cu_xO nanoforest with UV excitation.

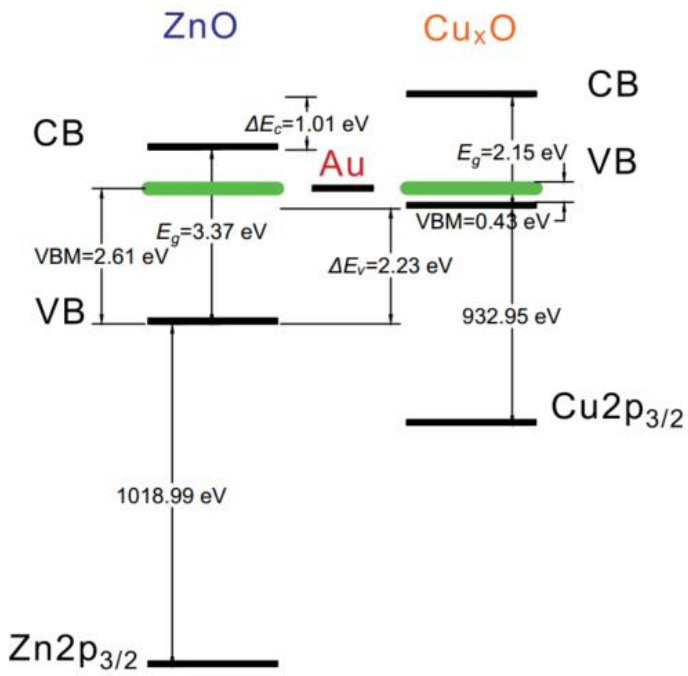

Figure 5.13: Band diagram of ZnO/Au/Cu_xO nanoforest after contact based on XPS and UV-Vis data.

5.5 The Role of Au Nanoparticles in ZnO/Au/Cu_xO Nanoforest

The role of noble metal in p-n heterojunction is still debated. It has been reported that gold nanoparticles enhanced the electron-hole separation of Cu_2O by localized surface plasmon resonance (LSPR) and electrons in CB of Cu_2O transferred directly to the CB of ZnO [194]. Other studies confirmed Z-scheme tunneling transfer of electrons from n-type semiconductor to Cu_xO through Au[195, 196]. In Figure 5.12, PL spectra of ZnO and ZnO/Au/Cu_xO nanoforest with UV excitation were measured and the obvious decrease of fluorescence was noticed. This is in contrast to regular p-n heterojunctions that should improve the population of excitons by separating holes and electrons more efficiently. The possible reason is that the excitons in CB of ZnO trapped by Au, resulting in smaller exciton population and less fluorescence radiation.

To explore the effect of Au nanoparticles in ZnO/Au/Cu_xO nanoforest, transient absorption measurements of ZnO, 5-nm thick Au, Cu_xO, Au/Cu_xO, and ZnO/Au/Cu_xO nanoforest on ITO substrates, shown in Figure 5.14, were taken with 400-nm pump laser and 450-720 nm white light as probe.

ZnO was not excited by 400-nm pump and the signal shown in Figure 5.14 (a) is the coherent artifact. In Figure 5.14 (b), Au shows weak signals, a positive excitation peak from d to sp band of gold in nanoscale at 552 nm corresponding to the spectrum of 5-nm gold[197, 198] and a negative plasmon depletion peak due to hot electrons relaxation via electron-phonon coupling at 700 nm, which correspond to the UV-Vis peak and literature[199, 200].

The maximum absorption peak of Cu_xO, Au/Cu_xO, ZnO/Cu_xO and ZnO/Au/Cu_xO nanoforest are at 491 nm, 497 nm, 498 nm, and 502 nm, respectively in Figure 5.14 (c-f).

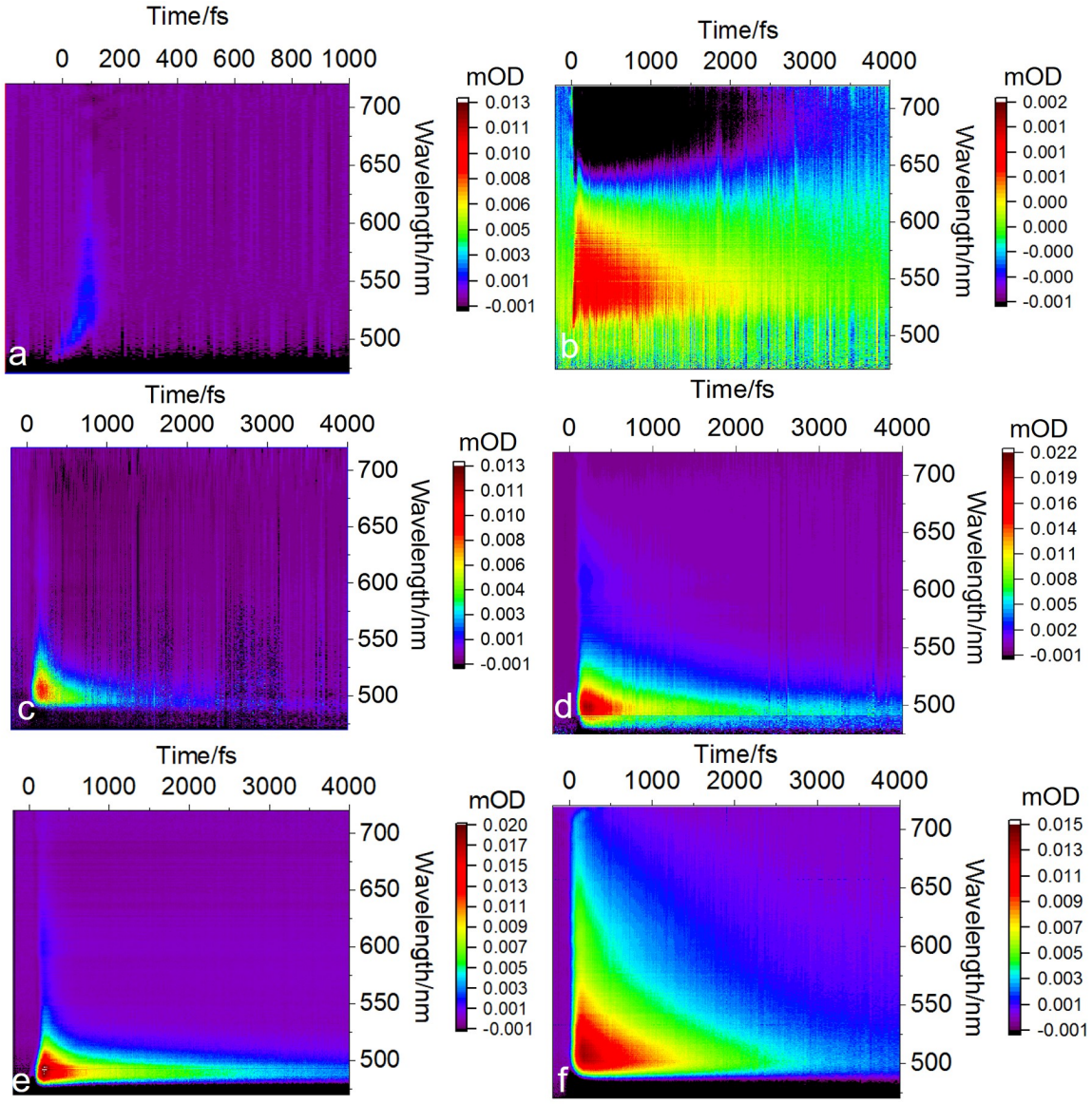

Figure 5.14: Transient absorption spectra with 440-nm pump and 450 nm-720 nm white light probe of ZnO (a), 5-nm thick Au (b), Cu_xO (c), Au/Cu_xO (d), ZnO/Cu_xO nanoforest (e), and ZnO/Au/Cu_xO nanoforest (f).

The decay curves at these λ_{max} were fitted with single exponential decay, eq. 5.8, except ZnO/Cu_xO which was fitted with double exponential decay, eq. 5.9, shown in Figure 5.15. The lifetime of Cu_xO, Au/Cu_xO, and ZnO/Au/Cu_xO nanoforest at λ_{max} are 516 fs for Cu_xO, 672 fs for Au/Cu_xO, and 1610 fs, respectively and the average lifetime calculated with eq. 5.10 [201] of ZnO/Cu_xO is 946 fs.

$$y = y_0 + A \times e^{-x/t} \tag{5.8}$$

$$y = y_0 + A_1 \times e^{-x/t_1} + A_2 \times e^{-x/t_2} \tag{5.9}$$

$$t_{Average} = (A_1 \times t_1 + A_2 \times t_2)/(A_1 + A_2) \tag{5.10}$$

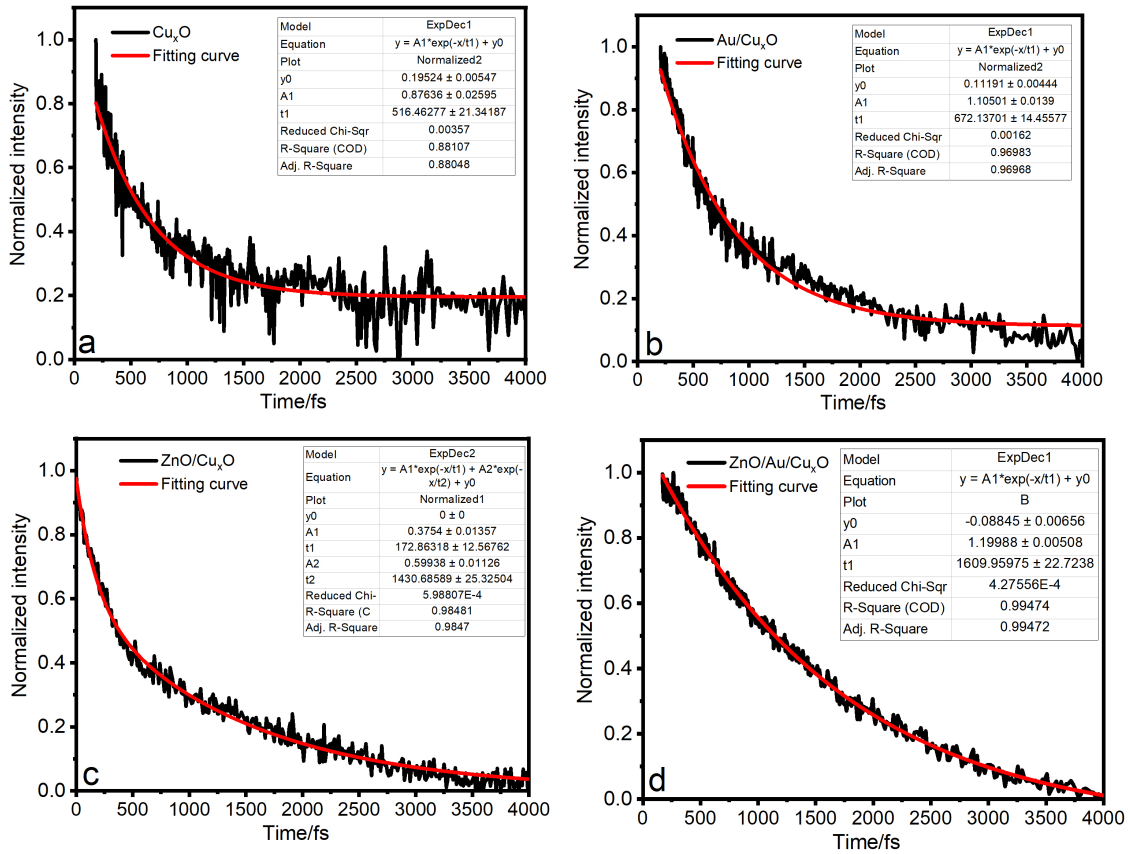

Figure 5.15: Fitting curves of transient absorption spectra with 440-nm pump and 450 nm-720 nm white light probe of Cu_xO (a), Au/Cu_xO (b), ZnO/Cu_xO nanoforest (c) and ZnO/Au/Cu_xO nanoforest (d) at λ_{max}. All decay curves were fitted with single exponential decay except ZnO/Cu_xO nanoforest (c) that was with double exponential decay.

On the basis of transient absorption data, the electron transfer pattern is determined shown in Figure 5.16. Generally, in pump-probe transient absorption measurements, the probe is a weaker laser compared to the pump. With 440 nm pump, ZnO is not excited. Electrons in ground states of Cu_xO were excited by 440 nm which equals 2.82 eV in energy unit, higher than the band gap, 2.15 eV, thereby leaving behind holes in VB. Excitons absorb photons further from the probe to give rise to absorption signal in transient absorption measurements, which is called excited state absorption (ESA)[202]. The instrument recorded the difference (ΔA) of absorption of the probe between with (A_t) and without pump (A_0). ESA shows positive ΔA because excitons absorb probe photons, which is positive A_t and small A_0, because no excitons are available for absorbing probe photons without the pump excitation. Recombination between excitons and holes leads to a decay in lower population of excitons, resulting in a decaying signal.

The decay curve in Figure 5.15 refers to the relaxation of ESA due to charge recombination in Cu_xO. Figure 5.16 (a) shows the decaying of excitons in pure Cu_xO, and the lifetime of excitons is the shortest of the materials. In Figure 5.16 (b), the lifetime is 1.3 times in Au/Cu_xO of that in Cu_xO. This indicates that electron-hole separation of Cu_xO was improved slightly by Au sacrificing electrons. LSPR is specifically size and wavelength dependent property. In this setup, 440 nm pump cannot excited 5-nm Au to LSPR state[203], so LSPR is not the main reason why the lifetime of excitons in Cu_xO changed.

According to literature, Schottky contact is hardly present between Cu_xO and Au so Ohmic contact without Schottky barrier should be probably formed like Cu_xO and ITO[162]. In this case, the holes in the VB of Cu_xO are continuously refilled by Au so recombination between excitons and holes is decreased, which makes the lifetime longer[204, 198].

In Figure 5.16 (c), with the assistance of ZnO, the lifetime of excitons in Cu_xO is lengthened further, to 1.8 times of that of Cu_xO. This may be because the holes in CB of Cu_xO would be filled by electrons from ZnO defects and the recombination is

reduced. In addition, electrons in CB of Cu_xO might move to the empty CB of ZnO[194] and absorbed photons in probe further and gave rise to longer lifetime. However, this process may be hard because the ZnO/Cu_xO lattice mismatch decreases electron transfer rate across the interface. Double exponential decay fitting may indicate there exists a slow process, which may correspond to it.

In Figure 5.16 (d), the band diagram of ZnO/Au/Cu_xO nanoforest, the lifetime is the longest that is 3.1 times of that of Cu_xO. This is contributed by both Au and ZnO. Au acts as electron donor for refilling holes in Cu_xO through hole transfer and ZnO assists in removing excitons from Cu_xO. Furthermore, ZnO/Au/Cu_xO nanoforest shows broad absorption spectrum. This may be because multiple-channel electron transfer patterns are involved in the process.

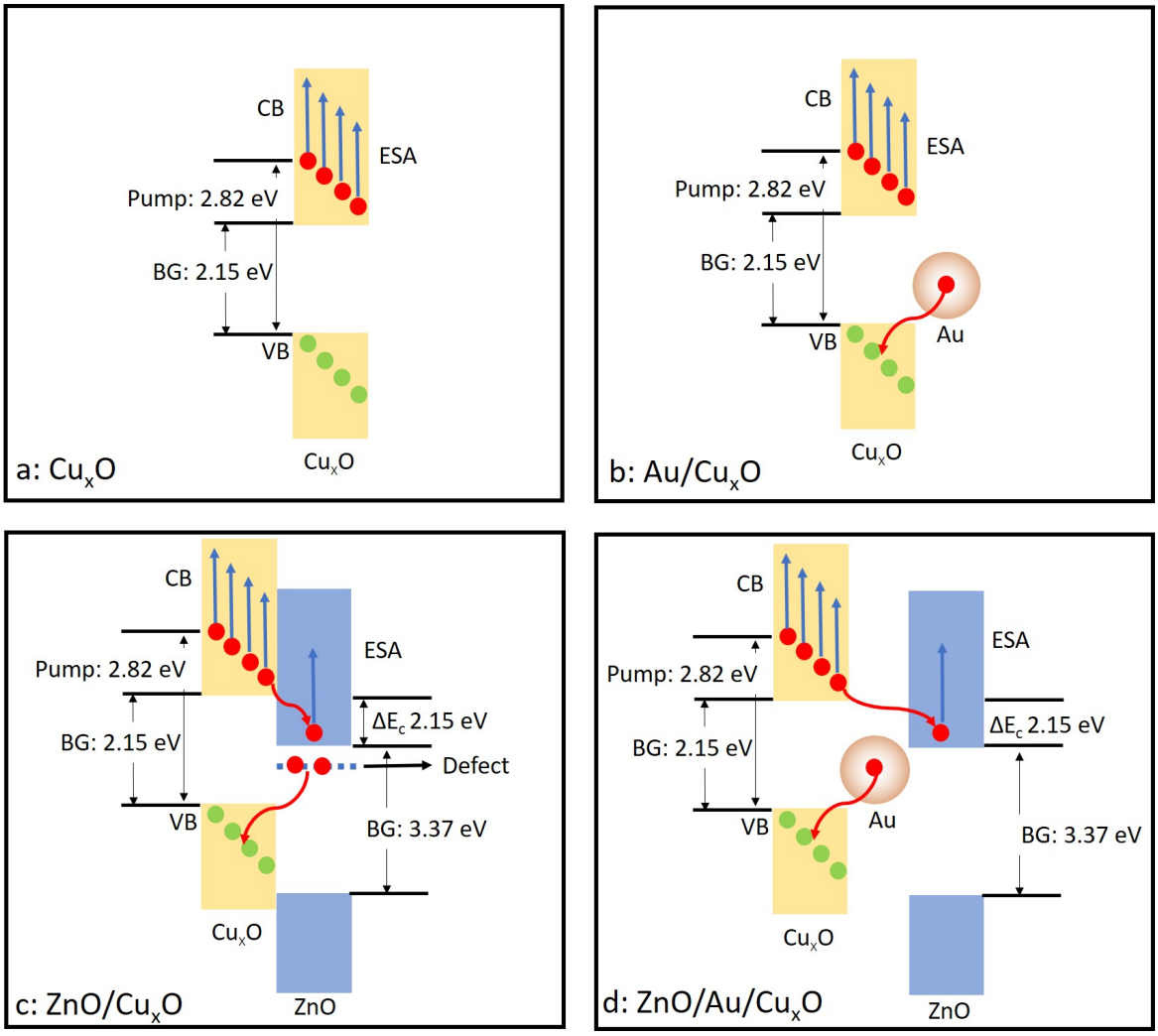

Figure 5.16: Band gap diagram of Cu_xO (a), Au/Cu_xO (b), ZnO/Cu_xO nanoforest (c) and ZnO/Au/Cu_xO nanoforest (d). Energy bands are not scaled.

5.6 Superhydrophobic and Photovoltaic Behavior in Photoelectrochemistry

Enlightened by the micro/nano-textured corrugations of ZnO/Au/Cu_xO nanoforest in Figure 5.1, we think the wettability on the surface is worth of further investigation. Contact angle measurements are shown in Figure 5.17. As-prepared ZnO has a contact angle with water of 89°, but after deposition of Cu_xO, the surface turned superhydrophobic with a contact angle of 163°. This is due to the wettability conversion from Wenzel to Cassie-Baxter after hierarchical rough surface construction [13, 2, 205]. As mentioned in Chapter 1, in Cassie-Baxter mode, water does not penetrate into the hollows of the hierarchical surface so the water drop line just follows the topography of the surface. In the Wenzel state, water gets into the hollows contacting the exposed substrate. They both can provide hydrophobic properties but only Cassie-Baxter surface may have a low roll-off angle and low contact angle hysteresis that means the difference of advancing angle(θ_α) and receding contact angle(θ_r) due to minimized adhesion[206, 2, 207]. The relationship between α, r, and roll-off angle (or sliding angle,a) is shown in eq. 5.11 with $\omega\gamma$/mg as a positive constant for certain surface and liquid drop[208]. This means the value of contact angle hysteresis or roll-off angle is a good sign to tell whether the surface is in Cassie-Baxter or Wenzel mode. The roll-off angle of ZnO/Au/Cu_xO nanoforest was measured as 3.8° by tilting the flat substrate of the instrument until the water droplet rolled off as well as the contact angle hysteresis calculated as 2.5°. Since the definition of superhydrophobicity is the surface with static contact angle $> 150°$ and roll-off angle $< 5°$ [3, 7], ZnO/Au/Cu_xO nanoforest is qualified.

$$sina = \omega\gamma/mg(cos\theta_r - cos\theta_\alpha) \tag{5.11}$$

where

m is the mass of the drop;

g is the acceleration of gravity;

ω is the width of the drop;

a is roll-off angle;

L is the surface tension of the liquid drop.

So $\omega\gamma$/mg is a constant for certain surface and liquid drop.

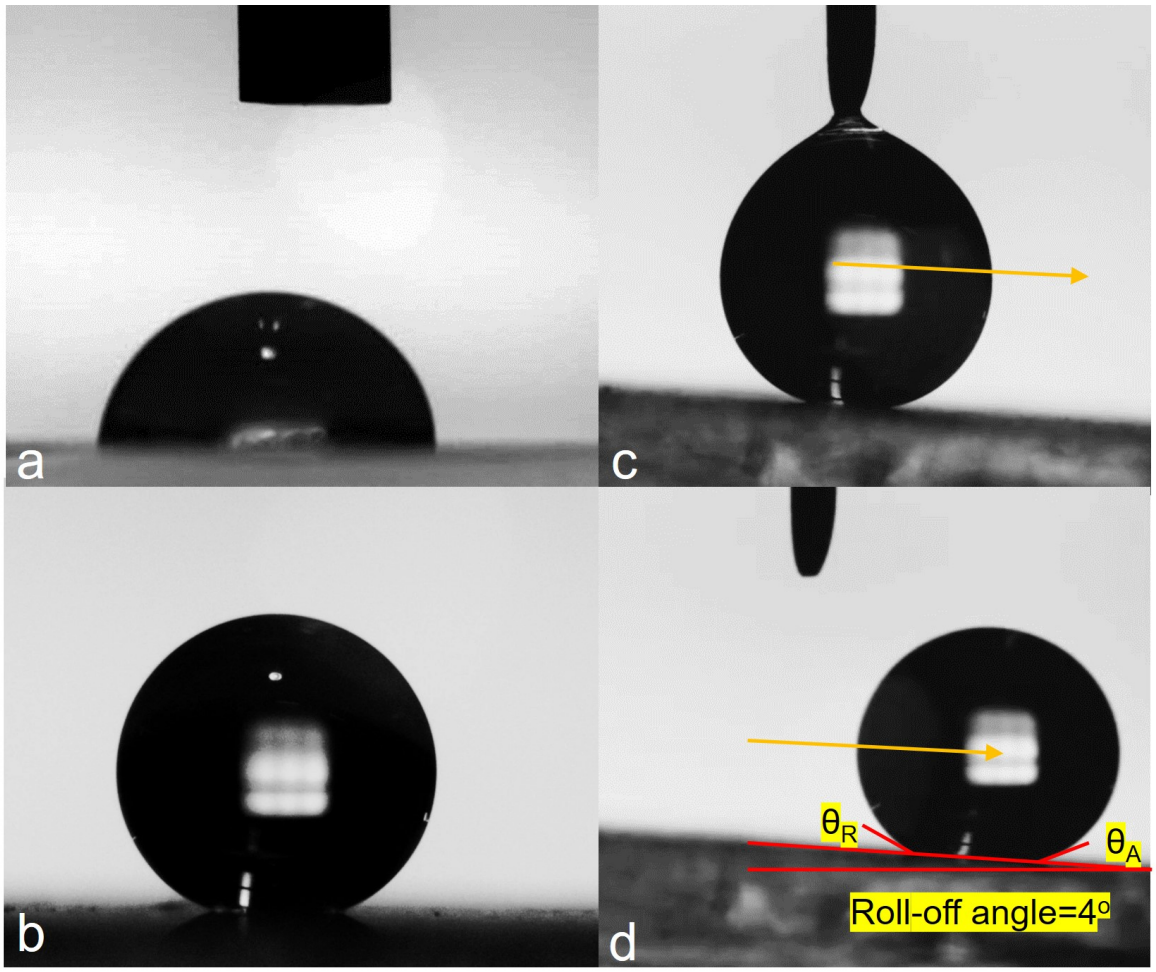

Figure 5.17: Static contact angle measurements with water of ZnO (a) and ZnO/Au/Cu_xO nanoforest (b) and roll-off angle measurement with water of ZnO/Au/Cu_xO nanoforest (c) and (d).

The most important benefit from superhydrophobicity is self-cleaning function. Self-cleaning of semiconductor nanomaterials may be due to two reasons, photocatalytic wettability conversion like TiO_2[209] and/or superhydrophobic surface[30]. In photocatalytic wettability conversion, the semiconductor surface is hydrophobic as prepared but after UV irradiation, semiconductor with oxygen vacancies adsorbed OH groups from water that makes the surface hydrophilic, so in this way of self-cleaning, UV irradiation is required. Hierarchical morphology allows water droplets to roll off dust and prevents dust accumulation on the solar-cell or other device surface, which maintains the performance of devices without the need of light irradiation[30, 24]. Cu_2O is a p-type semiconductor without oxygen vacancies, so this UV-assisted cleaning mode is not feasible. Cu_2O will be oxidized easily in liquid environment[210], so superhydrophobic morphology is the most possible strategy for Cu_2O self-cleaning[211, 31]. To determine if the superhydrophobicity helps prevent the surface from being degraded, transient photocurrents of ZnO/Au/Cu_xO nanoforest that stayed in air for 6 months in 0.1 M KCl and Cu 2p XPS data of Cu_2O and ZnO/Au/Cu_xO nanoforest after 6 months are shown in Figure 5.18 and it can be seen that the photocurrent only decrease 5% shown in Figure 5.18 (a) and oxidization states of the same spot on Cu ZnO/Au/Cu_xO nanoforest in show a slight change with Cu(I):Cu(II) area ratio from 5:2 to 5:2.3 shown in Figure 5.18 (b). A pure Cu_2O nanocube sample was compared after 6 months in air and the XPS showed that Cu(I):Cu(II) area ratio was changed from 1:0 to 1:1.4, shown in Figure 5.18 (c). Certainly the ratio could be affected by the detection point and different fitting, however compared to Cu_2O without hierarchical morphology, the Cu ZnO/Au/Cu_xO nanoforest shows no obvious degradation.

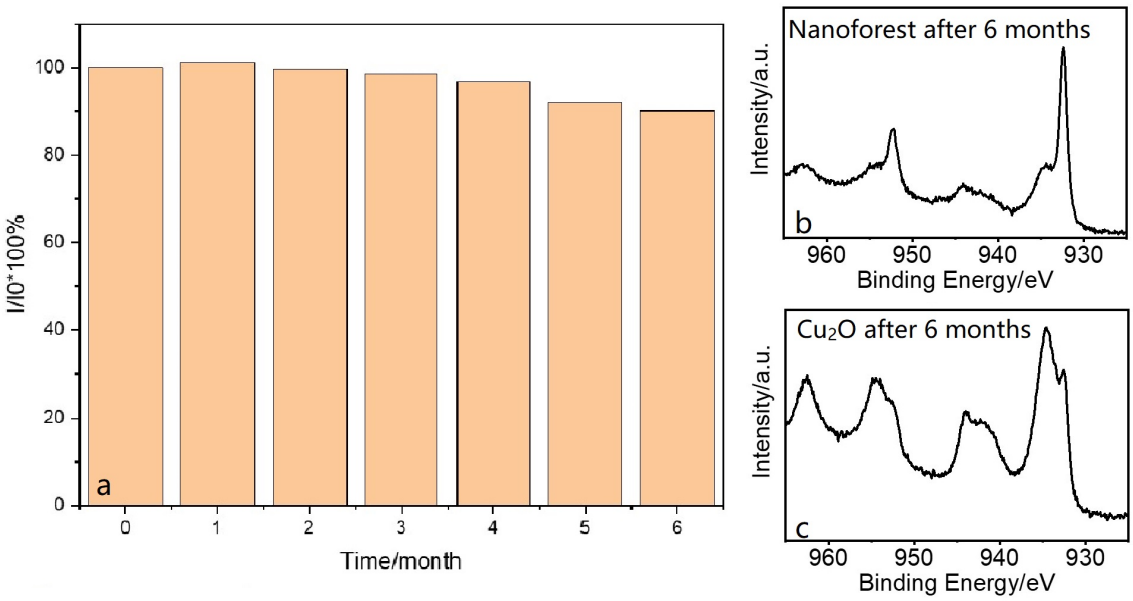

Figure 5.18: Transient photocurrents in continuous 6 months of ZnO/Au/Cu_xO (a) and Cu 2p XPS data of ZnO/Au/Cu_xO (b) and Cu_2O (c) after 6 months.

Transient photocurrents of ZnO, Cu_xO, ZnO/Cu_xO prepared at pH of 9 and ZnO/Au/Cu_xO nanoforest in 0.1 M KCl under xenon illumination at 0 V bias potential are shown in Figure 5.21 (a). ZnO is a n-type semiconductor so the photocurrent is positive while Cu_xO is p-type so it shows a negative photocurrent. ZnO/Cu_xO shows a positive current as well due to p-n junction. Electrons move from the CB in Cu_xO to the CB of ZnO, then to ITO and holes transfer from VB of ZnO to VB of Cu_xO that is the opposite way of electron transfer, so the overall photocurrent is positive, which agrees with literature[212, 143, 213, 214]. However, the photocurrent of ZnO/Au/Cu_2O nanoforest is much more negative than that of Cu_xO. This is because the electrons in CB of ZnO moved in the opposite way to Au layer and then moved to VB of Cu_xO via hole transfer between Au and Cu_xO[195, 157], and the holes in ZnO are filled by electrons from the external circuit instead of being filled by electrons from Cu_xO in ZnO/Cu_xO heterojunction, shown in Figure 5.19.

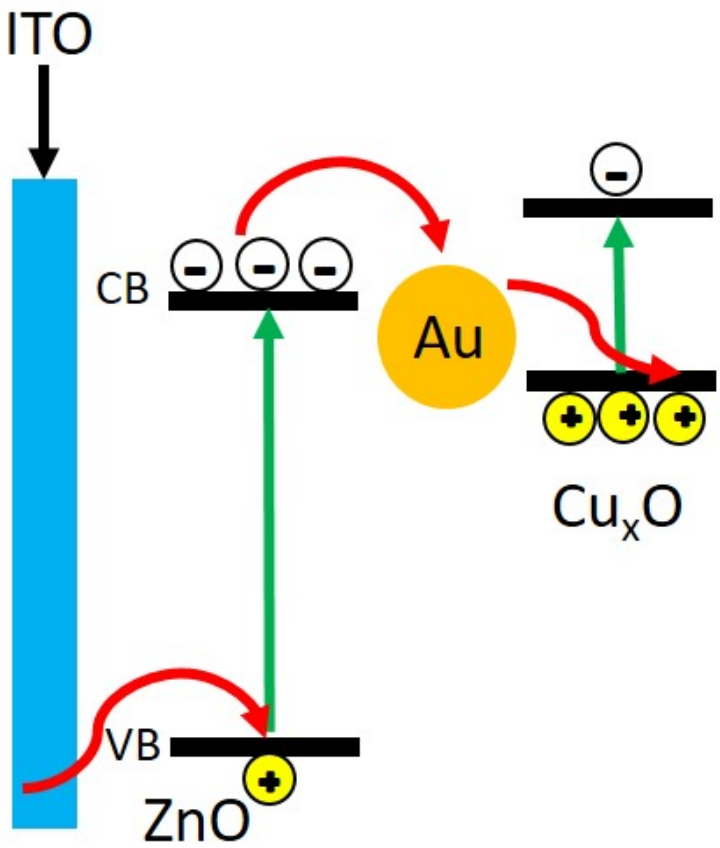

Figure 5.19: Scheme of electron transfer across the ZnO/Au/Cu_xO nanoforest with red arrows as charging current driven by majority carriers (j_G) under xenon illumination.

The photocurrent generation and decay dynamics in the heterojunction were further investigated based on the model in the literature [215]. Given that the electron transfer and hole recombination is only related to the concentration of carriers, the reaction follows pseudo-first-ordered dynamics. The overall photo-induced current consists of charging current driven by majority carriers (j_G) predicted by the Gärtner for p-n junction[216], electron-hole recombination over the band gap (j_{rec}) with first order rate constant as k_{rec} in s^{-1}, and electron transfer across the interface of electrode and electrolyte (j_{tr}) with first-order rate constant marked as k_{tr} in s^{-1}.

At the first moment under irradiation, minority carriers move across the interface and generated an instantaneous current (j_0) which is equal to the charging current driven by majority carriers (j_G), shown in red arrows in Figure 5.19. Charge recombination current, j_{rec}, is still 0 due to the fact that recombination does not happen yet at this point. Electron transfer across the interface of electrode and electrolyte (j_{tr}) is also assumed as 0 for the same reason. As more photons are absorbed and generated more excitons, electron transfer current (j_{tr}) from electrolyte contributes negatively to the overall photocurrent because of the hole consumption by the electrolyte, and j_{rec} would increase proportionately and compete with majority carrier generation as well, leading to the exponential decrease of the overall photocurrent and eventually the equilibrium is established and the photocurrent decayed to a plateau (j_s). After the light was off, the charging current vanished instantaneously and the residual carriers were released slowly and the photocurrent would decay in the opposite way and the final equilibrium was established to the dark current as it is before irradiation. Since a pseudo first order dynamics model is applied and two major dynamics happen at the same time, all decay curves are fitted with double exponential decay after normalization to (0,1), shown in Figure 5.20.

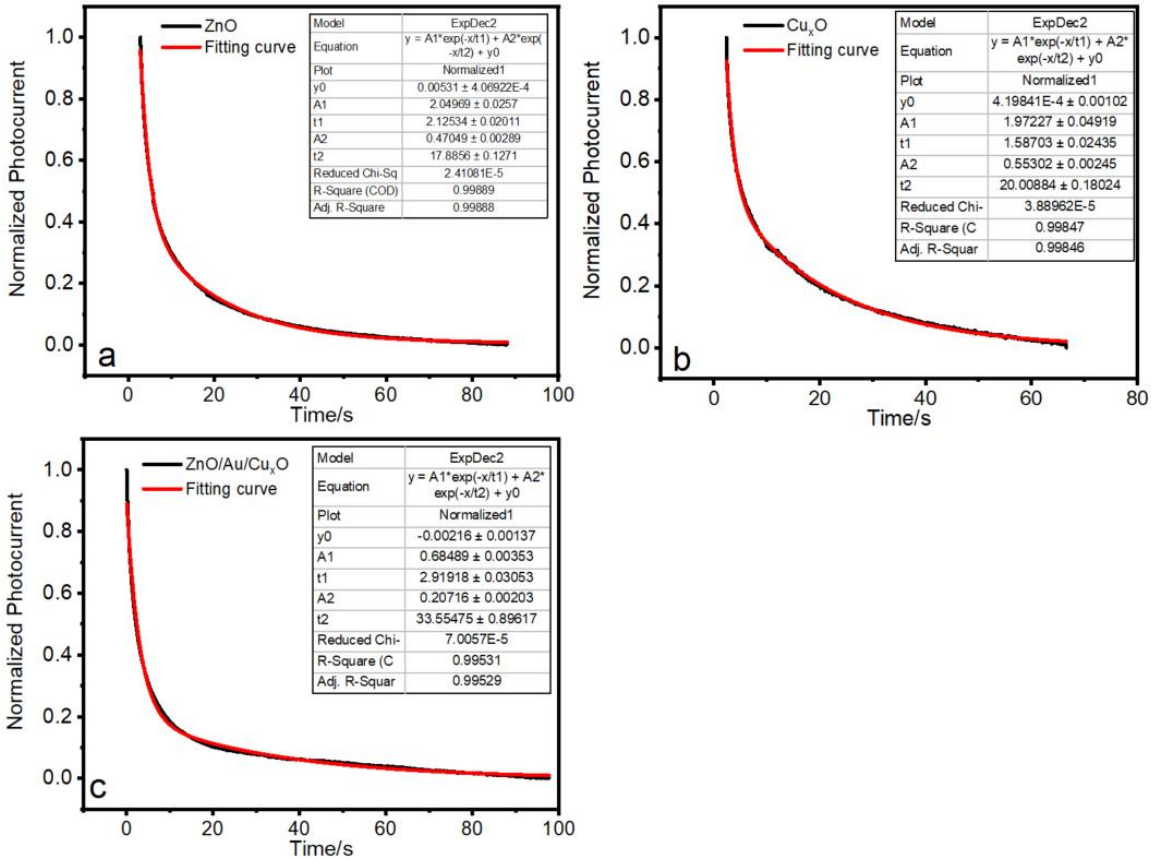

Figure 5.20: Fitting curves of normalized transient photocurrents of ZnO (a), Cu_xO (b), and ZnO/Au/Cu_xO (c).

In the model[215], the time constant t values which made larger contribution to fitting curves were used to calculate k_{tr} and k_{rec} with eq. 5.12 and 5.13.

$$t = (k_{tr} + k_{rec})^{-1} \tag{5.12}$$

$$j_s/j_0 = k_{tr}/(k_{tr} + k_{rec}) \tag{5.13}$$

From these results, it can be seen that the reaction constant of recombination (k_{rec}) of ZnO/Au/Cu_xO nanoforest is 0.0493 s^{-1}, much smaller compared to ZnO (0.1854 s^{-1}) or Cu_xO (0.1731 s^{-1}) but the reaction constant of electron transfer across the

heterojunction is 0.0493 s^{-1}, higher than that of ZnO (0.0118 s^{-1}) or Cu_xO (0.0054 s^{-1}). This confirms that ZnO/Au/Cu_xO nanoforest has lower recombination rate and higher electron transfer rate between electrode and electrolyte compare to the pristine semiconductors.

In order to determine the interaction between water and ZnO/Au/Cu_xO nanoforest electrode in KCl solutions under xenon illumination, scavenger test of ZnO/Au/Cu_xO nanoforest was applied by adding reagents to sacrifice potential free radical groups and the photocurrent afterward was measured under xenon illumination shown in Figure 5.21 (b). The scavengers of electrons (e^-), holes (h^+), e^--induced $\cdot O_2^-$, and h^+-induced OH· are H_2O_2, triethanolamine (TEOA), p-benzoquinone (BQ), and isopropyl alcohol (IPA), respectively. It can be seen that p-benzoquinone (BQ) and isopropyl alcohol (IPA) did not affect photocurrent, but TEOA caused 100 % decrease of negative photocurrent. H_2O_2 triggered 100% increase of positive photocurrent. Since H_2O_2 may be dissociated simultaneously under xenon illumination, this result was calculated by subtracting the photocurrents measured in the same concentration of H_2O_2 with a bare ITO glass as electrode. This sensing behavior corresponds to literature[161, 217]. This means water splitting-induced photocurrent is not the contribution to the overall photocurrent, which is attributed to the superhydrophobic property of ZnO/Au/Cu_xO nanoforest.

Comparison of EIS Nyquist plots of ZnO/Au/Cu_xO nanoforest measured at open circuit voltage in 0.1 M KCl solution in the dark and under illumination is shown in Figure 5.21 (c). The small arch at the beginning was not fully displayed due to the frequency limit of the potentiostats. This was attributed to the contact between gold and substrate that did not change after irradiation[218]. The second semicircle means the charge transfer at the interface between electrode and electrolyte and the straight line afterward means mass transfer of diffusion in bulk solution, which follows the regular Randles model. After irradiation, hole-electron separation caused the charge transfer faster and the second semicircle decreased.

MS analysis in the dark at 1 kHz with 0.1 M KCl water solution was performed shown in Figure 5.21 (d) to verify the p-n junction semiconducting behavior of ZnO/Au/Cu_xO nanoforest[145]. As discussed in Chapter 4, ZnO is a n-type semiconductor so the MS plot shows a positive slope with a flat potential of -0.708 V vs. NHE. while the MS plot of Cu_xO represents negative slope with flat potential of +0.402 V for Cu_xO vs. NHE. The peak contributed to the positive slopped curve from ZnO and negative slopped curve from Cu_xO is the evidence of p-n junction formation.

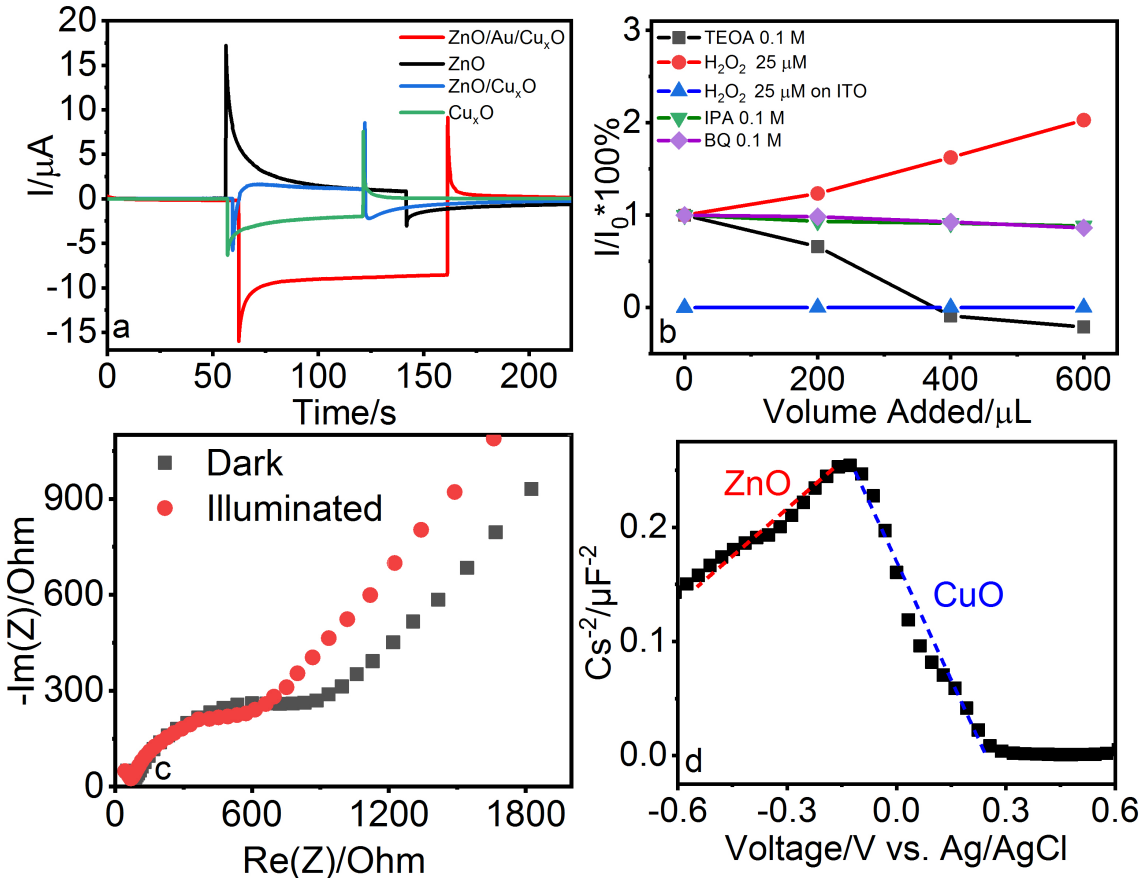

Figure 5.21: Transient photocurrents (a), and scavenger test (b) in 0.1 M KCl aqueous solution at 0 V under xenon illumination, EIS spectra under dark and xenon illumination conditions in 0.1 M KCl aqueous solution (c), and MS plots measured under dark condition in 0.1 M KCl aqueous solution at 1 kHz (d).

5.7 Conclusion

It has been confirmed that ZnO/Cu_2O P-N heterojunction shows high photovoltaic conversion but the lattice mismatch between ZnO and Cu_2O leads to slow electron transfer and high resistivity. In addition, the large band gap of Cu_2O (2.2-2.5 eV) limits its utilization of sunlight. Stability in liquid environment is still challenging. In this work, ZnO/Cu_xO P-N heterojunction was constructed in vertically-aligned tree-like array and a 5-nm thick gold film was deposited between ZnO and Cu_xO with PVD. The hierarchical morphology makes the surface water-repellant and self-cleaning. Gold is proved to protect ZnO morphology in the subsequent electrodeposition of Cu_xO, enhance the electron transfer, decrease the lattice match across ZnO and Cu_xO heterojunction, and eventually improve photocurrent response dramatically. This unique structure features higher negative photocurrent compare to bare Cu_xO, superhydrophobicity and good stability. The band diagram and the role of Au in the p-n heterojunction is further investigated with XPS and pump-probe transient absorption spectroscopy. With the assistance of Au, the material is able to absorb larger range of visible light and the lifetime of excitons in Cu_xO has been increased.

Chapter 6

SUMMARY

ZnO is an attractive semiconductor because of its natural n-type doping, high exciton binding energy, high thermal and chemical stability, morphological diversity, high abundance, low cost, and environmental compatibility. It is considered as a good alternative of TiO_2. In this dissertation, multi-layer hierarchical nanotrees were designed and synthesized with vertically-aligned [0001]-oriented ZnO nanowire array as stems and narrow-band-gap semiconductors, CdSSe, CuO, and Cu_xO, as branches via (002)-(111) lattice match.

Vertically-aligned ZnO nanowires were prepared with CVD or hydrothermal technique based on different applications. CVD provides solvent-free crystallization environment, longer nanowires and strong green luminescence while hydrothermal method can synthesize shorter and thinner ZnO nanowires on conductive glass, which can be utilized in cells and electronic devices.

Firstly, the ZnO/CdSSe nanotree with n-n heterojunction evinces its application in photoluminescence. ZnO/CdSSe nanowires were prepared via two-step chemical vapor deposition. The nanotrees are vertically-aligned on a sapphire substrate. Wurtzite ZnO and wurtzite CdSSe have large lattice mismatch but a transition crystal phase was found in XRD, which is considered as (111) of zincblende or imperfect (002) that matches (002) of ZnO. Since (111) and (002) have identical stacking arrangement, the lattice match problem is solved. ZnO and CdSSe have high exciton binding energies, larger than 25 meV, which is kT at room temperature. The CdSSe branches result in strong visible light absorption and form a type-II heterojunction with the ZnO stem that facilitates efficient electron transfer. Since when both n-type semiconductors are

excited, majority carriers will occupy CB and repel electron transfer across the heterojunction and give rise to larger population of excitons for fluorescence radiation. Vertically-aligned branched ZnO nanowires can provide direct electron transport pathways to substrates and allow for efficient charge separation. A combination of PL spectroscopy and lifetime measurements indicates that Z-scheme charge transfer mechanism exists in nanotree electron transfer. These advantages of nanoscale hierarchical heterostructures make ZnO/CdSSe nanotrees a promising semiconductor material for solar cells, and other opto-electronic devices.

Secondly, ZnO/CuO nanotree structure features p-n heterojunction. It was synthesized based on a multi-step seed-mediated hydrothermal approach. CuO has a narrow band gap (1.2 eV) and low lattice mismatch with ZnO through (002) and (111), great stability and the ability of epitaxial growth via monoclinic crystal packing. The nanotrees form a p-n junction at the branch/stem interface that facilitates charge separation upon illumination. Photo-electrochemical measurements in different solvents show that ZnO/CuO hierarchical nanostructures have enhanced photocatalytic activity compared to non-hierarchical structure of ZnO/CuO, pure ZnO and pure CuO nanoparticles. The combination of ZnO and CuO in tree-like nanostructures provides opportunities for the design of photo-electrochemical sensors, photocatalytic synthesis, and solar energy conversion.

However, Cu^{2+} in CuO has $3d^9$ electron configuration. The similarity of HOMO and LUMO leads to a high recombination rate and low photovoltaic efficiency. Cu^{+} in Cu_2O has $3d^{10}$ electron configuration, whose excitons are supposed to have longer lifetime and provide higher photovoltaic efficiency. Cu_2O has vital drawbacks in deposition onto ZnO-based nanotrees due to large lattice mismatch with ZnO.

Therefore, in the last part, ZnO/Au/Cu_xO was prepared to overcome all the problems above. Electron transfer patterns at heterojunctions and photovoltaic conversion were confirmed with ultrafast laser spectroscopy and photoelectrochemistry. Cu_xO alloy semiconductor has a tunable band gap and its lattice mismatch with ZnO

was reduced by inducing CuO. 5-nm-thick Au film plays a critical role in the configuration. Au has very low lattice mismatch with Cu_2O so it can guide (111) oriented growth of Cu_xO. As a noble metal, it can assist in electron transfer across the interface between ZnO and Cu_xO. Most importantly, it is inert enough compare to Ag, Cu and many other metals so that it can protect ZnO at high pH in Cu_xO growth from dissolving.

This work investigated (002)-(111) crystal match in self-assembling of ZnO-based hierarchical structures and may guide future architecture of hierarchical semiconductors and their applications.

BIBLIOGRAPHY

[1] Bharat Bhushan. Biomimetics: Lessons from nature–an overview. *Philosophical Transactions of the Royal Society A: Mathematical, Physical and Engineering Sciences*, 367(1893):1445–1486, apr 2009.

[2] Alberto Giacomello, Simone Meloni, Mauro Chinappi, and Carlo Massimo Casciola. Cassie–Baxter and Wenzel states on a nanostructured surface: Phase diagram, metastabilities, and transition mechanism by atomistic free energy calculations. *Langmuir*, 28(29):10764–10772, jul 2012.

[3] Abraham Marmur. The lotus effect: Superhydrophobicity and metastability. *Langmuir*, 20(9):3517–3519, apr 2004.

[4] Bruce Alberts, Alexander Johnson, Peter Walter, Julian Lewis, and Martin Raff. *Molecular Biology of the Cell*. Norton & Company, 2014.

[5] K.L. Mittal, editor. *Advances in Contact Angle, Wettability and Adhesion*. John Wiley & Sons, Inc., sep 2015.

[6] Akira Fujishima, Tata N. Rao, and Donald A. Tryk. Titanium dioxide photocatalysis. *Journal of Photochemistry and Photobiology C: Photochemistry Reviews*, 1(1):1–21, jun 2000.

[7] John T Simpson, Scott R Hunter, and Tolga Aytug. Superhydrophobic materials and coatings: a review. *Reports on Progress in Physics*, 78(8):086501, jul 2015.

[8] Xin Li, Jiaguo Yu, and Mietek Jaroniec. Hierarchical photocatalysts. *Chem. Soc. Rev.*, 45:2603–2636, 2016.

[9] Jiaguo Yu, Lijuan Zhang, Bei Cheng, and Yaorong Su. Hydrothermal preparation and photocatalytic activity of hierarchically sponge-like macro-/mesoporous titania. *The Journal of Physical Chemistry C*, 111(28):10582–10589, jul 2007.

[10] P. Yang, T. Deng, D. Zhao, P. Feng, D. Pine, B. F. Chmelka, G. M. Whitesides, and G. D. Stucky. Hierarchically ordered oxides. *Science*, 282(5397):2244–2246, dec 1998.

[11] Jaehyun Kim, Wooseok Kim, and Kijung Yong. CuO/ZnO heterostructured nanorods: Photochemical synthesis and the mechanism of h_2s gas sensing. *J. Phys. Chem. C*, 116(29):15682–15691, 2012.

[12] Meenal Deo, Deodatta Shinde, Ashish Yengantiwar, Jyoti Jog, Beatrice Hannoyer, Xavier Sauvage, Mahendra More, and Satishchandra Ogale. Cu_2o/ZnO hetero-nanobrush: hierarchical assembly, field emission and photocatalytic properties. *Journal of Materials Chemistry*, 22(33):17055, 2012.

[13] Zheng Guo, Xing Chen, Jie Li, Jin-Huai Liu, and Xing-Jiu Huang. ZnO/CuO hetero-hierarchical nanotrees array: Hydrothermal preparation and self-cleaning properties. *Langmuir*, 27(10):6193–6200, may 2011.

[14] In Sun Cho, Zhebo Chen, Arnold J. Forman, Dong Rip Kim, Pratap M. Rao, Thomas F. Jaramillo, and Xiaolin Zheng. Branched TiO_2 nanorods for photoelectrochemical hydrogen production. *Nano Lett.*, 11(11):4978–4984, 2011.

[15] Young wook Jun, Sang-Min Lee, Nam-Jung Kang, and Jinwoo Cheon. Controlled synthesis of multi-armed CdS nanorod architectures using monosurfactant system. *Journal of the American Chemical Society*, 123(21):5150–5151, may 2001.

[16] Wei-Tang Yao, Shu-Hong Yu, Shu-Juan Liu, Jun-Peng Chen, Xian-Ming Liu, and Fan-Qing Li. Architectural control syntheses of CdS and CdSe nanoflowers, branched nanowires, and nanotrees via a solvothermal approach in a mixed solution and their photocatalytic property. *The Journal of Physical Chemistry B*, 110(24):11704–11710, jun 2006.

[17] Yeonwoong Jung, Dong-Kyun Ko, and Ritesh Agarwal. Synthesis and structural characterization of single-crystalline branched nanowire heterostructures. *Nano Letters*, 7(2):264–268, feb 2007.

[18] Deli Wang, Fang Qian, Chen Yang, Zhaohui Zhong, and Charles M. Lieber. Rational growth of branched and hyperbranched nanowire structures. *Nano Letters*, 4(5):871–874, may 2004.

[19] Alexander Kelrich, Ofir Sorias, Yonatan Calahorra, Yaron Kauffmann, Ran Gladstone, Shimon Cohen, Meir Orenstein, and Dan Ritter. InP nanoflag growth from a nanowire template by in situ catalyst manipulation. *Nano Letters*, 16(4):2837–2844, mar 2016.

[20] Xinchen Wang, Jimmy C. Yu, Chunman Ho, Yidong Hou, and Xianzhi Fu. Photocatalytic activity of a hierarchically macro/mesoporous titania. *Langmuir*, 21(6):2552–2559, mar 2005.

[21] Z.-Y. Yuan, T.-Z. Ren, and B.-L. Su. Hierarchically mesostructured titania materials with an unusual interior macroporous structure. *Advanced Materials*, 15(17):1462–1465, sep 2003.

[22] Irene Gonzalez-Valls and Monica Lira-Cantu. Vertically-aligned nanostructures of ZnO for excitonic solar cells: a review. *Energy Environ. Sci.*, 2(1):19–34, 2009.

[23] Jun Wu, Jun Xia, Wei Lei, and Baoping Wang. Superhydrophobic surface based on a coral-like hierarchical structure of ZnO. *PLoS ONE*, 5(12):e14475, dec 2010.

[24] Jia Zhu, Ching-Mei Hsu, Zongfu Yu, Shanhui Fan, and Yi Cui. Nanodome solar cells with efficient light management and self-cleaning. *Nano Letters*, 10(6):1979–1984, jun 2010.

[25] Jiaguo Yu, Jimmy C. Yu, Lizhi Zhang, Xinchen Wang, and Ling Wu. Facile fabrication and characterization of hierarchically porous calcium carbonate microspheres. *Chemical Communications*, (21):2414, 2004.

[26] Wingkei Ho, Jimmy C. Yu, and Shuncheng Lee. Synthesis of hierarchical nanoporous f-doped TiO2 spheres with visible light photocatalytic activity. *Chemical Communications*, (10):1115, 2006.

[27] Jimmy C. Yu, Xinchen Wang, and Xianzhi Fu. Pore-wall chemistry and photocatalytic activity of mesoporous titania molecular sieve films. *Chemistry of Materials*, 16(8):1523–1530, apr 2004.

[28] Quanjun Xiang, Kangle Lv, and Jiaguo Yu. Pivotal role of fluorine in enhanced photocatalytic activity of anatase TiO2 nanosheets with dominant (001) facets for the photocatalytic degradation of acetone in air. *Applied Catalysis B: Environmental*, 96(3-4):557–564, jun 2010.

[29] Rongfu Wen, Shanshan Xu, Dongliang Zhao, Yung-Cheng Lee, Xuehu Ma, and Ronggui Yang. Hierarchical superhydrophobic surfaces with micropatterned nanowire arrays for high-efficiency jumping droplet condensation. *ACS Applied Materials & Interfaces*, 9(51):44911–44921, dec 2017.

[30] Yan Liu, Arnab Das, Sheng Xu, Ziyin Lin, Chen Xu, Zhong Lin Wang, Ajeet Rohatgi, and Ching Ping Wong. Hybridizing ZnO nanowires with micropyramid silicon wafers as superhydrophobic high-efficiency solar cells. *Advanced Energy Materials*, 2(1):47–51, nov 2011.

[31] Kaichen Xu, Huangping Yan, Chuan Fu Tan, Yuyao Lu, Yang Li, Ghim Wei Ho, Rong Ji, and Minghui Hong. Hedgehog inspired CuO nanowires/Cu_2O composites for broadband visible-light-driven recyclable surface enhanced raman scattering. *Advanced Optical Materials*, 6(7):1701167, feb 2018.

[32] D. C. Reynolds, D. C. Look, B. Jogai, C. W. Litton, T. C. Collins, W. Harsch, and G. Cantwell. Neutral−donor−bound−exciton complexes in ZnO crystals. *Phys. Rev. B*, 57:12151–12155, 1998.

[33] D. M. Bagnall, Y. F. Chen, Z. Zhu, T. Yao, S. Koyama, M. Y. Shen, and T. Goto. Optically pumped lasing of ZnO at room temperature. *Appl. Phys. Lett.*, 70(17):2230–2232, 1997.

[34] Yu Hsun Chou, Bo Tsun Chou, Chih Kai Chiang, Ying Yu Lai, Chun Ting Yang, Heng Li, Tzy Rong Lin, Chien Chung Lin, Hao Chung Kuo, Shing Chung Wang, and Tien Chang Lu. Ultrastrong mode confinement in ZnO surface plasmon nanolasers. *ACS Nano*, 9(4):3978–3983, 2015.

[35] Zhong Lin Wang and Jinhui Song. Piezoelectric nanogenerators based on zinc oxide nanowire arrays. *Science*, 312(5771):242–246, 2006.

[36] Hao Ming Chen, Chih Kai Chen, Yu Chuan Chang, Chi Wen Tsai, Ru Shi Liu, Shu Fen Hu, Wen Sheng Chang, and Kuei Hsien Chen. Quantum dot monolayer sensitized ZnO nanowire−array photoelectrodes: True efficiency for water splitting. *Angew. Chem. Int. Ed.*, 49(34):5966–5969, 2010.

[37] Min Lai and D. Jason Riley. Templated electrosynthesis of zinc oxide nanorods. *Chem. Mater.*, 18(9):2233–2237, 2006.

[38] Pu Xian Gao, Yong Ding, Wenjie Mai, William L. Hughes, Changshi Lao, and Zhong Lin Wang. Conversion of zinc oxide nanobelts into superlattice−structured nanohelices. *Science*, 309(5741):1700–1704, 2005.

[39] Y. H. Yang, Y. Zhang, N. W. Wang, C. X. Wang, B. J. Li, and G. W. Yang. ZnO nanocone: Application in fabrication of the smallest whispering gallery optical resonator. *Nanoscale*, 3:592–597, 2011.

[40] Bing Yin, Yu Qiu, Heqiu Zhang, Jixue Lei, Yue Chang, Jiuyu Ji, Yingmin Luo, Yu Zhao, and Lizhong Hu. Piezoelectric effect of 3−D ZnO nanotetrapods. *RSC Adv.*, 5:11469–11474, 2015.

[41] Fang-Xing Xiao, Jianwei Miao, Hua Bing Tao, Sung-Fu Hung, Hsin-Yi Wang, Hong Bin Yang, Jiazang Chen, Rong Chen, and Bin Liu. One-dimensional hybrid nanostructures for heterogeneous photocatalysis and photoelectrocatalysis. *Small*, 11(18):2115–2131, 2015.

[42] Sangam Banerjee, Judy Gopal, P Muraleedharan, AK Tyagi, and Baldev Raj. Physics and chemistry of photocatalytic titanium dioxide: Visualization of bactericidal activity using atomic force microscopy. *Current Science*, 90:10, 06 2006.

[43] Hsuan-Liang Liu and Thomas C.-K. Yang. Photocatalytic inactivation of escherichia coli and lactobacillus helveticus by ZnO and TiO_2 activated with ultraviolet light. *Process Biochemistry*, 39(4):475–481, dec 2003.

[44] Katarina S. Wissiak, Boris Šket, and Margareta Vrtačnik. Heterogeneous photocatalytic decomposition of halosubstituted benzyl alcohols on semiconductor particles in aqueous media. *Chemosphere*, 41(9):1451–1455, nov 2000.

[45] J. Font A. Fabregat A Fortuny, C. Bengoa. Bimetallic catalysts for continuous catalytic wet air oxidation of phenol. *Journal of Hazardous Materials*, 64(2):181–193, jan 1999.

[46] J.C. Fan, K.M. Sreekanth, Z. Xie, S.L. Chang, and K.V. Rao. p-type ZnO materials: Theory, growth, properties and devices. *Progress in Materials Science*, 58(6):874–985, jul 2013.

[47] C. H. Park, S. B. Zhang, and Su-Huai Wei. Origin ofp-type doping difficulty in ZnO: the impurity perspective. *Physical Review B*, 66(7), aug 2002.

[48] Zhaoke Zheng, Wen Xie, Zhi Shiuh Lim, Lu You, and Junling Wang. CdS sensitized 3D hierarchical TiO_2/ZnO heterostructure for efficient solar energy conversion. *Sci. Rep.*, 4:5721, 2014.

[49] Juan A. Anta, Elena Guillén, and Ramón Tena-Zaera. ZnO-based dye-sensitized solar cells. *J. Phys. Chem. C*, 116(21):11413–11425, 2012.

[50] Candice I. Pelligra, Pawel W. Majewski, and Chinedum O. Osuji. Large area vertical alignment of ZnO nanowires in semiconducting polymer thin films directed by magnetic fields. *Nanoscale*, 5(21):10511–10517, 2013.

[51] Chunyan Luan, Tai Lun Wong, and Juan Antonio Zapien. Vertically aligned ZnO nanorods/CdS nanowires branched heterostructures: Cathodoluminescence properties and photovoltaic application. *Journal of Crystal Growth*, 374:65–70, jul 2013.

[52] Zhiming Bai, Xiaoqin Yan, Yong Li, Zhuo Kang, Shiyao Cao, and Yue Zhang. 3d-branched ZnO/CdS nanowire arrays for solar water splitting and the service safety research. *Advanced Energy Materials*, 6(3):1501459, dec 2015.

[53] Venkata Thulasivarma Chebrolu and Hee-Je Kim. Recent progress in quantum dot sensitized solar cells: an inclusive review of photoanode, sensitizer, electrolyte, and the counter electrode. *Journal of Materials Chemistry C*, 7(17):4911–4933, 2019.

[54] Sheng-Bo Wang, Chih-Hung Hsiao, Shoou-Jinn Chang, Z. Y. Jiao, Sheng-Joue Young, Shang-Chao Hung, and Bohr-Ran Huang. ZnO branched nanowires and the p-CuO/n-ZnO heterojunction nanostructured photodetector. *IEEE Transactions on Nanotechnology*, 12(2):263–269, mar 2013.

[55] Nguyen Minh Vuong, Nguyen Duc Chinh, Bui The Huy, and Yong-Ill Lee. CuO-decorated ZnO hierarchical nanostructures as efficient and established sensing materials for h_2s gas sensors. *Scientific Reports*, 6(26736), 2016.

[56] Pai-Chun Chang, Zhiyong Fan, Dawei Wang, Wei-Yu Tseng, Wen-An Chiou, Juan Hong, and Jia G. Lu. ZnO nanowires synthesized by vapor trapping CVD method. *Chemistry of Materials*, 16(24):5133–5137, nov 2004.

[57] Seung Chul Lyu, Ye Zhang, Cheol Jin Lee, Hyun Ruh, and Hwack Joo Lee. Low-temperature growth of ZnO nanowire array by a simple physical vapor-deposition method. *Chemistry of Materials*, 15(17):3294–3299, aug 2003.

[58] Davide Barreca, Elisabetta Comini, Angelo P. Ferrucci, Alberto Gasparotto, Chiara Maccato, Cinzia Maragno, Giorgio Sberveglieri, and Eugenio Tondello. First example of $ZnO-TiO_2$ nanocomposites by chemical vapor deposition: structure, morphology, composition, and gas sensing performances. *Chemistry of Materials*, 19(23):5642–5649, nov 2007.

[59] Chen-Hao Ku, Hung-Hsien Yang, Guan-Ren Chen, and Jih-Jen Wu. Wet-chemical route to ZnO nanowire-layered basic zinc acetate/ZnO nanoparticle composite film. *Crystal Growth & Design*, 8(1):283–290, jan 2008.

[60] Jian Zhu and Da Deng. Ammonia-assisted wet-chemical synthesis of ZnO microrod arrays on substrates for microdroplet transfer. *Langmuir*, 33(24):6143–6150, jun 2017.

[61] Cheng Li, Guosong Hong, Pengwei Wang, Dapeng Yu, and Limin Qi. Wet chemical approaches to patterned arrays of well-aligned ZnO nanopillars assisted by monolayer colloidal crystals. *Chemistry of Materials*, 21(5):891–897, mar 2009.

[62] Jeong-Seok Na, Bo Gong, Giovanna Scarel, and Gregory N. Parsons. Surface polarity shielding and hierarchical ZnO nano-architectures produced using sequential hydrothermal crystal synthesis and thin film atomic layer deposition. *ACS Nano*, 3(10):3191–3199, sep 2009.

[63] Masao Miyake, Makoto Suginohara, Naoto Narahara, Tetsuji Hirato, and Paul V. Braun. Low-temperature hydrothermal synthesis of colloidal crystal templated nanostructured single-crystalline ZnO. *Chemistry of Materials*, 29(22):9734–9741, nov 2017.

[64] Chuanwei Cheng, Bo Liu, Huiying Yang, Weiwei Zhou, Li Sun, Rui Chen, Siu Fung Yu, Jixuan Zhang, Hao Gong, Handong Sun, and Hong Jin Fan. Hierarchical assembly of ZnO nanostructures on SnO_2 backbone nanowires: Low-temperature hydrothermal preparation and optical properties. *ACS Nano*, 3(10):3069–3076, sep 2009.

[65] Lidia Armelao, Gregorio Bottaro, Michele Pascolini, Michele Sessolo, Eugenio Tondello, Marco Bettinelli, and Adolfo Speghini. Structure-luminescence correlations in europium-doped sol-gel ZnO nanopowders. *The Journal of Physical Chemistry C*, 112(11):4049–4054, feb 2008.

[66] Quan Liu, Paola Mantilla-Perez, Miguel Montes Bajo, Pablo Romero-Gomez, and Jordi Martorell. UV-induced oxygen removal for photostable, high-efficiency PTB7-th:PC71bm photovoltaic cells. *ACS Applied Materials & Interfaces*, 8(42):28750–28756, oct 2016.

[67] Michael Krumm, Carlos Lizandara Pueyo, and Sebastian Polarz. Monolithic zinc oxide aerogels from organometallic sol-gel precursors. *Chemistry of Materials*, 22(18):5129–5136, sep 2010.

[68] Zhengxin Li, Jesus Nieto-Pescador, Alexander J Carson, Jolie C Blake, and Lars Gundlach. Efficient Z-scheme charge separation in novel vertically aligned ZnO/CdSSe nanotrees. *Nanotechnology*, 27(13):135401, feb 2016.

[69] Zhengxin Li, Meng Jia, Baxter Abraham, Jolie C. Blake, Daniel Bodine, John T. Newberg, and Lars Gundlach. Synthesis and characterization of ZnO/CuO vertically aligned hierarchical tree-like nanostructure. *Langmuir*, 34(3):961–969, oct 2017.

[70] Lionel Vayssieres, Karin Keis, Sten-Eric Lindquist, and Anders Hagfeldt. Purpose-built anisotropic metal oxide material: 3D highly oriented microrod array of ZnO. *The Journal of Physical Chemistry B*, 105(17):3350–3352, may 2001.

[71] Sunandan Baruah and Joydeep Dutta. Hydrothermal growth of ZnO nanostructures. *Sci. Tech. Adv. Mater*, 10(1):013001, 2009.

[72] Romain Parize, Jérôme Garnier, Odette Chaix-Pluchery, Claire Verrier, Estelle Appert, and Vincent Consonni. Effects of hexamethylenetetramine on the nucleation and radial growth of ZnO nanowires by chemical bath deposition. *J. Phys. Chem. C*, 120(9):5242–5250, 2016.

[73] Lukas Schmidt-Mende and Judith L. MacManus-Driscoll. ZnO – nanostructures, defects, and devices. *Materials Today*, 10(5):40–48, may 2007.

[74] Zafar Ibupoto, Kimleang Khun, Martin Eriksson, Mohammad AlSalhi, Muhammad Atif, Anees Ansari, and Magnus Willander. Hydrothermal growth of vertically aligned ZnO nanorods using a biocomposite seed layer of ZnO nanoparticles. *Materials*, 6(8):3584–3597, aug 2013.

[75] Baek Hyun Kim and Jae W. Kwon. Metal catalyst for low-temperature growth of controlled zinc oxide nanowires on arbitrary substrates. *Scientific Reports*, 4(1), mar 2014.

[76] Yannick Cudennec and André Lecerf. The transformation of $cu(OH)_2$ into CuO, revisited. *Solid State Sci.*, 5(11):1471 – 1474, 2003.

[77] Ya-Huei Tsai, Kaushik Chanda, Yi-Ting Chu, Chun-Ya Chiu, and Michael H. Huang. Direct formation of small Cu_2O nanocubes, octahedra, and octapods for efficient synthesis of triazoles. *Nanoscale*, 6(15):8704, jun 2014.

[78] N. Koteeswara Reddy, M. Devika, Nava Shpaisman, Moshit Ben-Ishai, and Fernando Patolsky. Synthesis and cathodoluminescence properties of CdSe/ZnO hierarchical nanostructures. *J. Mater. Chem.*, 21(11):3858–3864, 2011.

[79] Y.L. Lee, C.F. Chi, and S.Y. Liau. CdS/CdSe co-sensitized TiO_2 photoelectrode for efficient hydrogen generation in a photoelectrochemical cell. *Chem. Mater.*, 22(3):922–927, 2010.

[80] ME Rincon, M Sanchez, and J Ruiz-Garcia. Photocorrosion of coupled CdS/CdSe photoelectrodes coated with ZnO atomic force microscopy and X-Ray diffraction studies. *J. Electrochem. Soc.*, 145(10):3535–3544, 1998.

[81] Kurtis S. Leschkies, Ramachandran Divakar, Joysurya Basu, Emil Enache-Pommer, Janice E. Boercker, C. Barry Carter, Uwe R. Kortshagen, David J. Norris, and Eray S. Aydil. Photosensitization of ZnO nanowires with CdSe quantum dots for photovoltaic devices. *Nano Lett.*, 7(6):1793–1798, 2007.

[82] Peter Y. Yu and Manuel Cardona. *Fundamentals of Semiconductors*. Springer Berlin Heidelberg, 2010.

[83] Marc Dvorak, Su-Huai Wei, and Zhigang Wu. Origin of the variation of exciton binding energy in semiconductors. *Physical Review Letters*, 110(1), jan 2013.

[84] K. M. Ip, C. R. Wang, Quan Li, and S. K. Hark. Excitons and surface luminescence of CdS nanoribbons. *Applied Physics Letters*, 84(5):795–797, feb 2004.

[85] B. Liu, R. Chen, X. L. Xu, D. H. Li, Y. Y. Zhao, Z. X. Shen, Q. H. Xiong, and H. D. Sun. Exciton-related photoluminescence and lasing in CdS nanobelts. *The Journal of Physical Chemistry C*, 115(26):12826–12830, jun 2011.

[86] Robert W. Meulenberg, Jonathan R.I. Lee, Abraham Wolcott, Jin Z. Zhang, Louis J. Terminello, and Tony van Buuren. Determination of the exciton binding energy in CdSe quantum dots. *ACS Nano*, 3(2):325–330, feb 2009.

[87] E. Menéndez-Proupin and C. Trallero-Giner. Electric-field and exciton structure in CdSe nanocrystals. *Physical Review B*, 69(12), mar 2004.

[88] Li J. Zhang, Shuo Li, Bing K. Liu, De J. Wang, and Teng F. Xie. Highly efficient CdS/WO_3 photocatalysts: Z-scheme photocatalytic mechanism for their enhanced photocatalytic h2 evolution under visible light. *ACS Catalysis*, 4(10):3724–3729, 2014.

[89] Jian Jin, Jiaguo Yu, Daipeng Guo, Can Cui, and Wingkei Ho. A hierarchical Z-scheme CdS–WO_3 photocatalyst with enhanced CO_2 reduction activity. *Small*, 11:5262–5271, 2015.

[90] Zong Bao Yu, Ying Peng Xie, Gang Liu, Gao Qing (Max) Lu, Xiu Liang Ma, and Hui-Ming Cheng. Self-assembled CdS/Au/ZnO heterostructure induced by surface polar charges for efficient photocatalytic hydrogen evolution. *J. Mater. Chem. A*, 1:2773–2776, 2013.

[91] Si Qi Liu, Min Quan Yang, Zi Rong Tang, and Yi Jun Xu. A nanotree-like CdS/ZnO nanocomposite with spatially branched hierarchical structure for photocatalytic fine-chemical synthesis. *Nanoscale*, 6:7193–7198, 2014.

[92] Guang Zhu, Yusheng Zhou, Sihong Wang, Rusen Yang, Yong Ding, Xue Wang, Yoshio Bando, and Zhonglin Wang. Synthesis of vertically aligned ultra-long ZnO nanowires on heterogeneous substrates with catalyst at the root. *Nanotechnology*, 23(5):055604, 2012.

[93] PD Yang, HQ Yan, S Mao, R Russo, J Johnson, R Saykally, N Morris, J Pham, RR He, and HJ Choi. Controlled growth of ZnO nanowires and their optical properties. *Adv. Funct. Mater.*, 12(5):323–331, 2002.

[94] Baek Hyun Kim and Jae W. Kwon. Metal catalyst for low-temperature growth of controlled zinc oxide nanowires on arbitrary substrates. *Sci. Rep.*, 4:4379, 2014.

[95] Liang Yih Chen, Shu Han Wu, and Yu Tung Yin. Catalyst-free growth of vertical alignment ZnO nanowire arrays by a two-stage process. *J. Phys. Chem. C*, 113(52):21572–21576, 2009.

[96] Tamita Rakshit, Suvra P. Mondal, Indranil Manna, and Samit K. Ray. CdS-decorated ZnO nanorod heterostructures for improved hybrid photovoltaic devices. *Acs Appl. Mater. Inter.*, 4(11):6085–6095, 2012.

[97] Yoon Myung, Dong Myung Jang, Tae Kwang Sung, Yong Jei Sohn, Gyeong Bok Jung, Yong Jae Cho, Han Sung Kim, and Jeunghee Park. Composition-tuned ZnO/CdSSe core/shell nanowire arrays. *ACS Nano*, 4(7):3789–3800, 2010.

[98] Anna Laera, Vincenzo Resta, Emanuela Piscopiello, Valerio Miceli, Monica Schioppa, Anna Scalone, Francesca Di Benedetto, and Leander Tapfer. In situ growth of well-dispersed CdS nanocrystals in semiconducting polymers. *Nanoscale Research Letters*, 8(1):382, 2013.

[99] Chin-Yu Yeh, Su-Huai Wei, and Alex Zunger. Relationships between the band gaps of the zinc-blende and wurtzite modifications of semiconductors. *Phys. Rev. B*, 50:2715–2718, 1994.

[100] AL Pan, H Yang, RB Liu, RC Yu, BS Zou, and ZL Wang. Color-tunable photoluminescence of alloyed CdS_xSe_{1-x} nanobelts. *J. Am. Chem. Soc.*, 127(45):15692–15693, 2005.

[101] P. Kubelka and F. Munk. Ein beitrag zur optik der farbanstriche. *Z. Techn. Phys.*, 12:593–601, 1931.

[102] Jun Pan, Muhammad Iqbal Bakti Utama, Qing Zhang, Xinfeng Liu, Bo Peng, Lai Mun Wong, Tze Chien Sum, Shijie Wang, and Qihua Xiong. Composition-tunable vertically aligned CdS_xSe_{1-x} nanowire arrays *via* van der waals epitaxy: Investigation of optical properties and photocatalytic behavior. *Adv. Mater.*, 24(30):4151–4156, 2012.

[103] Amin Torabi and Viktor N. Staroverov. Band gap reduction in ZnO and ZnS by creating layered ZnO/ZnS heterostructures. *J. Phys. Chem. Lett.*, 6(11):2075–2080, 2015.

[104] Shinjita Acharya, D. D. Sarma, Nikhil R. Jana, and Narayan Pradhan. An alternate route to high-quality ZnSe and Mn-doped ZnSe nanocrystals. *J. Phys. Chem. Lett.*, 1(2):485–488, 2010.

[105] Xue Wen Wang, Gang Liu, Zhi Gang Chen, Feng Li, Lian Zhou Wang, Gao Qing Lu, and Hui Ming Cheng. Enhanced photocatalytic hydrogen evolution by prolonging the lifetime of carriers in ZnO/CdS heterostructures. *Chem. Commun.*, pages 3452–3454, 2009.

[106] Zhiqiang Wang, Jian Wang, Tsun Kong Sham, and Shaoguang Yang. Origin of luminescence from ZnO/CdS core/shell nanowire arrays. *Nanoscale*, 6:9783–9790, 2014.

[107] S Lettieri, L Santamaria Amato, P Maddalena, E Comini, C Baratto, and S Todros. Recombination dynamics of deep defect states in zinc oxide nanowires. *Nanotechnology*, 20(17):175706, 2009.

[108] C. Soci, A. Zhang, B. Xiang, S. A. Dayeh, D. P. R. Aplin, J. Park, X. Y. Bao, Y. H. Lo, and D. Wang. ZnO nanowire UV photodetectors with high internal gain. *Nano Lett.*, 7(4):1003–1009, 2007.

[109] Marco Cirillo, Tangi Aubert, Raquel Gomes, Rik Van Deun, Philippe Emplit, Amelie Biermann, Holger Lange, Christian Thomsen, Edouard Brainis, and Zeger Hens. "flash" synthesis of CdSe/CdS core-shell quantum dots. *Chem. Mater.*, 26(2):1154–1160, 2014.

[110] Wennuan Nan, Yuan Niu, Haiyan Qin, Fan Cui, Yu Yang, Runchen Lai, Wanzhen Lin, and Xiaogang Peng. Crystal structure control of zinc−blende CdSe/CdS core/shell nanocrystals: Synthesis and structure−dependent optical properties. *J. Am. Chem. Soc.*, 134(48):19685–19693, 2012.

[111] Issam Hemdana, Mounira Mahdouani, and Ramzi Bourguiga. Investigation of the radiative lifetime in core˘shell CdSe/ZnS and CdSe/ZnSe quantum dots. *Physica B*, 407(17):3313–3319, 2012.

[112] Junpeng Lu, Hongwei Liu, Minrui Zheng, Hongji Zhang, Sharon Xiaodai Lim, Eng Soon Tok, and Chorng Haur Sow. Laser modified ZnO/CdSSe core-shell nanowire arrays for micro-steganography and improved photoconduction. *Sci. Rep.*, 4:6350, 2014.

[113] Tridip Ranjan Chetia, Dipankar Barpuzary, and Mohammad Qureshi. Enhanced photovoltaic performance utilizing effective charge transfers and light scattering effects by the combination of mesoporous, hollow 3D−ZnO along with 1D−ZnO in cds quantum dot sensitized solar cells. *Phys. Chem. Chem. Phys.*, 16(20):9625–9633, 2014.

[114] Anusorn Kongkanand, Kevin Tvrdy, Kensuke Takechi, Masaru Kuno, and Prashant V. Kamat. Quantum dot solar cells. tuning photoresponse through size and shape control of CdSe-TiO_2 architecture. *J. Am. Chem. Soc.*, 130(12):4007–4015, 2008.

[115] Eduard Zenkevich, Aleksander Stupak, Clemens Göhler, Cornelius Krasselt, and Christian von Borczyskowski. Tuning electronic states of a CdSe/ZnS quantum dot by only one functional dye molecule. *ACS Nano*, 9(3):2886–2903, 2015.

[116] Yu Li, Zheng-Yi Fu, and Bao-Lian Su. Hierarchically structured porous materials for energy conversion and storage. *Adv. Funct. Mater.*, 22(22):4634–4667, 2012.

[117] Alireza Kargar, Yi Jing, Sung Joo Kim, Conor T. Riley, Xiaoqing Pan, and Deli Wang. ZnO/CuO heterojunction branched nanowires for photoelectrochemical hydrogen generation. *ACS Nano*, 7(12):11112–11120, 2013.

[118] Zachary S. Fishman, Benjamin Rudshteyn, Yulian He, Bolun Liu, Subhajyoti Chaudhuri, Mikhail Askerka, Gary L. Haller, Victor S. Batista, and Lisa D. Pfefferle. Fundamental role of oxygen stoichiometry in controlling the band gap and reactivity of cupric oxide nanosheets. *J. Am. Chem. Soc*, 138(34):10978–10985, 2016.

[119] Xiao Liu, Baosheng Du, Ye Sun, Miao Yu, Yongqi Yin, Wei Tang, Chong Chen, Lei Sun, Bin Yang, Wenwu Cao, and Michael N. R. Ashfold. Sensitive room temperature photoluminescence-based sensing of H_2S with novel CuO-ZnO nanorods. *ACS Appl. Mater. Interfaces*, 8(25):16379–16385, 2016.

[120] Susmita Das and Vimal Chandra Srivastava. Synthesis and characterization of ZnO/CuO nanocomposite by electrochemical method. *Mater. Sci. Semicond. Process.*, 57:173 – 177, 2017.

[121] Sanggon Kim, Younghyo Lee, Ayeong Gu, Chanseok You, Kwangjoong Oh, Sanghyun Lee, and Yeonho Im. Synthesis of vertically conformal ZnO/CuO core-shell nanowire arrays by electrophoresis-assisted electroless deposition. *J. Phys. Chem. C*, 118(14):7377–7385, 2014.

[122] A. E. Gunnæs, S. Gorantla, O. M. Løvvik, J. Gan, P. A. Carvalho, B. G. Svensson, E. V. Monakhov, K. Bergum, I. T. Jensen, and S. Diplas. Epitaxial strain-induced growth of CuO at Cu_2O/ZnO interfaces. *The Journal of Physical Chemistry C*, 120(41):23552–23558, oct 2016.

[123] Ang Li, Huaihe Song, Jisheng Zhou, Xiaohong Chen, and Siyuan Liu. CuO nanowire growth on Cu_2O by in situ thermal oxidation in air. *CrystEngComm*, 15:8559–8564, 2013.

[124] Dawei Su, Xiuqiang Xie, Shixue Dou, and Guoxiu Wang. CuO single crystal with exposed 001 facets - a highly efficient material for gas sensing and Li-ion battery applications. *Sci. Rep.*, 4:5753, 2014.

[125] Abhishek Kumar Mishra, Alberto Roldan, and Nora H. de Leeuw. CuO surfaces and CO_2 activation: A dispersion-corrected DFT+U study. *J. Phys. Chem. C*, 120(4):2198–2214, 2016.

[126] Yu Chang and Hua Chun Zeng. Controlled synthesis and self-assembly of single-crystalline CuO nanorods and nanoribbons. *Cryst. Growth Des.*, 4(2):397–402, 2004.

[127] Matt Law, Lori E. Greene, Justin Johnson, Richard C. Saykally, and Peidong Yang. Nanowire dye-sensitized solar cells. *Nat. Mater.*, 4:455–459, 2005.

[128] Mohammad Vaseem, Ahmad Umar, Sang Hoon Kim, and Yoon-Bong Hahn. Low-temperature synthesis of flower-shaped CuO nanostructures by solution process: Formation mechanism and structural properties. *J. Phys. Chem. C*, 112(15):5729–5735, 2008.

[129] John F. Moulder, William F. Stickle, Peter E. Sobol, and Kenneth D. Bomben. *Handbook of X-ray Photoelectron Spectroscopy: A Reference Book of Standard Spectra for Identification and Interpretation of XPS Data.* Physical Electronics, Inc., 1992.

[130] M Chen, X Wang, Y.H Yu, Z.L Pei, X.D Bai, C Sun, R.F Huang, and L.S Wen. X-ray photoelectron spectroscopy and Auger electron spectroscopy studies of Al-doped ZnO films. *Appl. Surf. Sci.*, 158:134 – 140, 2000.

[131] Huihu Wang and Changsheng Xie. The effects of oxygen partial pressure on the microstructures and photocatalytic property of ZnO nanoparticles. *Physica E Low Dimens Syst Nanostruct*, 40(8):2724 – 2729, 2008.

[132] Xi-Guang Han, Hui-Zhong He, Qin Kuang, Xi Zhou, Xian-Hua Zhang, Tao Xu, Zhao-Xiong Xie, and Lan-Sun Zheng. Controlling morphologies and tuning the related properties of nano/microstructured ZnO crystallites. *The Journal of Physical Chemistry C*, 113(2):584–589, 2009.

[133] Fang-Xing Xiao. Construction of highly ordered ZnO-TiO_2 nanotube arrays (ZnO/TNTs) heterostructure for photocatalytic application. *ACS Appl. Mater. Interfaces*, 4(12):7055–7063, 2012.

[134] Numan Salah, A. Hameed, M. Aslam, Saeed S. Babkair, and F.S. Bahabri. Photocatalytic activity of V doped ZnO nanoparticles thin films for the removal of 2-chlorophenol from the aquatic environment under natural sunlight exposure. *Journal of Environmental Economics and Management*, 177:53–64, 2016.

[135] Sambhaji M. Pawar, Jongmin Kim, Akbar. I Inamdar, Hyeonseok Woo, Yongcheol Jo, Bharati S. Pawar, Sangeun Cho, Hyungsang Kim, and Hyunsik Im. Multi-functional reactively-sputtered copper oxide electrodes for supercapacitor and electro-catalyst in direct methanol fuel cell applications. *Sci. Rep.*, 6(21310), 2016.

[136] Fei Wu, Sriya Banerjee, Huafang Li, Yoon Myung, and Parag Banerjee. Indirect phase transformation of CuO to Cu_2O on a nanowire surface. *Langmuir*, 32(18):4485–4493, 2016.

[137] V. Srikant and D. R. Clarke. On the optical band gap of zinc oxide. *J. Appl. Phys.*, 83(10):5447–5451, 1998.

[138] F. Marabelli, G. B. Parravicini, and F. Salghetti-Drioli. Optical gap of CuO. *Phys. Rev. B*, 52:1433–1436, Jul 1995.

[139] Talaat M. Hammad, Jamil K. Salem, Roger G. Harrison, Rolf Hempelmann, and Nasser K. Hejazy. Optical and magnetic properties of Cu-doped ZnO nanoparticles. *J. Mater. Sci. Mater. Electron.*, 24(8):2846–2852, Aug 2013.

[140] Allen J. Bard and Larry R. Faulkner. *Electrochemical Methods: Fundamentals and Applications.* John Wiley and Sons, Inc., 2000.

[141] Noel Nesakumar, Kavitha Thandavan, Swaminathan Sethuraman, Uma Maheswari Krishnan, and John Bosco Balaguru Rayappan. An electrochemical biosensor with nanointerface for lactate detection based on lactate dehydrogenase immobilized on zinc oxide nanorods. *J. Colloid Interface Sci*, 414:90 – 96, 2014.

[142] Neha Batra, Monika Tomar, and Vinay Gupta. Realization of an efficient cholesterol biosensor using ZnO nanostructured thin film. *Analyst*, 137:5854–5859, 2012.

[143] Zhuo Kang, Xiaoqin Yan, Yunfei Wang, Zhiming Bai, Yichong Liu, Zheng Zhang, Pei Lin, Xiaohui Zhang, Haoge Yuan, Xueji Zhang, and Yue Zhang. Electronic structure engineering of Cu_2O film/ZnO nanorods array all-oxide p-n heterostructure for enhanced photoelectrochemical property and self-powered biosensing application. *Scientific Reports*, 5(7882), 2015.

[144] Min Seok Koo, Kangwoo Cho, Jeyong Yoon, and Wonyong Choi. Photoelectrochemical degradation of organic compounds coupled with molecular hydrogen generation using electrochromic TiO_2 nanotube arrays. *Environ. Sci. Technol.*, 51(11):6590–6598, 2017.

[145] K. Gelderman, L. Lee, and S. W. Donne. Flat-band potential of a semiconductor: Using the Mott−Schottky equation. *J. Chem. Educ.*, 84(4):685, 2007.

[146] Yang Yang, Di Xu, Qingyong Wu, and Peng. Diao. Cu_2ocuo.

[147] Paul B. Merkel, Pu Luo, Joseph P. Dinnocenzo, and Samir Farid. Accurate oxidation potentials of benzene and biphenyl derivatives via electron-transfer equilibria and transient kinetics. *The Journal of Organic Chemistry*, 74(15):5163–5173, 2009. PMID: 19588891.

[148] Juanjuan Sun, Xinyong Li, Qidong Zhao, Jun Ke, and Dongke Zhang. Novel $V_2O_5/BiVO_4/TiO_2$ nanocomposites with high visible-light-induced photocatalytic activity for the degradation of toluene. *J. Phys. Chem. C*, 118(19):10113–10121, 2014.

[149] A.M. Ferrari-Lima, R.P. de Souza, S.S. Mendes, R.G. Marques, M.L. Gimenes, and N.R.C. Fernandes-Machado. Photodegradation of benzene, toluene and xylenes under visible light applying n-doped mixed TiO_2 and ZnO catalysts. *Catal. Today*, 241:40 – 46, 2015.

[150] Hussain Al-Ekabi and Paul De Mayo. Surface photochemistry: on the mechanism of the semiconductor photoinduced valence isomerization of hexamethyl dewar benzene to hexamethylbenzene. *J. Phys. Chem.*, 90(17):4075–4080, 1986.

[151] Richard M. Lambert and Gianfranco Pacchioni, editors. *Chemisorption and Reactivity on Supported Clusters and Thin Films*. Springer Netherlands, 1997.

[152] Xiang Chen, Pei Lin, Xiaoqin Yan, Zhiming Bai, Haoge Yuan, Yanwei Shen, Yichong Liu, Guangjie Zhang, Zheng Zhang, and Yue Zhang. Three-dimensional ordered ZnO/Cu_2O nanoheterojunctions for efficient metal–oxide solar cells. *ACS Applied Materials & Interfaces*, 7(5):3216–3223, jan 2015.

[153] Siddarth Jain, Suryakant Mishra, and Tridib K. Sarma. Zn^{2+} induced self-assembled growth of octapodal Cu_xO–ZnO microcrystals: Multifunctional applications in reductive degradation of organic pollutants and nonenzymatic electrochemical sensing of glucose. *ACS Sustainable Chemistry & Engineering*, 6(8):9771–9783, jun 2018.

[154] B. Kramm, A. Laufer, D. Reppin, A. Kronenberger, P. Hering, A. Polity, and B. K. Meyer. The band alignment of Cu_2O/ZnO and Cu_2O/GaN heterostructures. *Applied Physics Letters*, 100(9):094102, feb 2012.

[155] Jing Bai, Yunpo Li, Rui Wang, Ke Huang, Qingyi Zeng, Jinhua Li, and Baoxue Zhou. A novel 3D ZnO/Cu_2O nanowire photocathode material with highly efficient photoelectrocatalytic performance. *Journal of Materials Chemistry A*, 3(45):22996–23002, 2015.

[156] Joseph J. Loferski. Theoretical considerations governing the choice of the optimum semiconductor for photovoltaic solar energy conversion. *Journal of Applied Physics*, 27(7):777–784, jul 1956.

[157] Ellen Caroline Jacobsen. Analysis of the ZnO/Cu_2O thin film heterojunction for intermediate band solar cell applications. Master's thesis, 2015.

[158] Alberto Mittiga, Enrico Salza, Francesca Sarto, Mario Tucci, and Rajaraman Vasanthi. Heterojunction solar cell with 2% efficiency based on a Cu_2O substrate. *Applied Physics Letters*, 88(16):163502, apr 2006.

[159] K. Akimoto, S. Ishizuka, M. Yanagita, Y. Nawa, Goutam K. Paul, and T. Sakurai. Thin film deposition of Cu_2O and application for solar cells. *Solar Energy*, 80(6):715–722, jun 2006.

[160] Gang Zhou, Xiaoyong Xu, Tao Ding, Bing Feng, Zhijia Bao, and Jingguo Hu. Well–steered charge–carrier transfer in 3D branched Cu_xO/ZnO@Au heterostructures for efficient photocatalytic hydrogen evolution. *ACS Applied Materials & Interfaces*, 7(48):26819–26827, nov 2015.

[161] Daniela Chirizzi, Maria Rachele Guascito, Emanuela Filippo, Cosimino Malitesta, and Antonio Tepore. A novel nonenzymatic amperometric hydrogen peroxide sensor based on CuO@Cu_2O nanowires embedded into poly(vinyl alcohol). *Talanta*, 147:124–131, jan 2016.

[162] B. K. Meyer, A. Polity, D. Reppin, M. Becker, P. Hering, P. J. Klar, Th. Sander, C. Reindl, J. Benz, M. Eickhoff, C. Heiliger, M. Heinemann, J. Bläsing, A. Krost, S. Shokovets, C. Müller, and C. Ronning. Binary copper oxide semiconductors: From materials towards devices. *Physica Status Solidi (b)*, 249(8):1487–1509, jun 2012.

[163] L. C. Olsen, R. C. Bohara, and M. W. Urie. Explanation for low-efficiency cu2o schottky-barrier solar cells. *Applied Physics Letters*, 34(1):47–49, jan 1979.

[164] Dayong Jiang, Rusheng Liu, Qingchao Zhang, Rui Li, Qian Duan, Jieming Qin, Xiande Shen, Jianhua Hou, Jianxun Zhao, Qingcheng Liang, and Shang Gao. High-performance ultraviolet photodetectors based on ZnO/Au/ZnO sandwich structure. *Journal of Physics D: Applied Physics*, 48(27):275104, jun 2015.

[165] Cheng Li, Xiuting Zhu, Haifeng Zhang, Zhichao Zhu, Bo Liu, and Chuanwei Cheng. 3D ZnO/Au/CdS sandwich structured inverse opal as photoelectrochemical anode with improved performance. *Advanced Materials Interfaces*, 2(18):1500428, oct 2015.

[166] S. Sultana, S. Mansingh, M. Scurrell, and K. M. Parida. Controlled synthesis of CeO_2NS-Au-CdS QDs ternary nanoheterostructure: A promising visible light responsive photocatalyst for h2 evolution. *Inorganic Chemistry*, 56(20):12297–12307, oct 2017.

[167] Adriana Paracchino, Jan Cornelius Brauer, Jacques-Edouard Moser, Elijah Thimsen, and Michael Graetzel. Synthesis and characterization of high-photoactivity electrodeposited Cu_2O solar absorber by photoelectrochemistry and ultrafast spectroscopy. *The Journal of Physical Chemistry C*, 116(13):7341–7350, mar 2012.

[168] P. E. de Jongh, D. Vanmaekelbergh, and J. J. Kelly. Cu_2O: electrodeposition and characterization. *Chemistry of Materials*, 11(12):3512–3517, dec 1999.

[169] Q. T. Du, J. S. Tan, Q. T. Wang, C. Y. Li, X. H. Liu, R. S. Cai, Y. H. Ding, and Y. Q. Wang. Electrochemical deposition and formation mechanism of single-crystalline Cu_2O octahedra on aluminum. *Journal of Analytical Methods in Chemistry*, 2012:1–8, 2012.

[170] Chaoqun Dong, Yan Wang, Junling Xu, Guanhua Cheng, Wanfeng Yang, Tianyi Kou, Zhonghua Zhang, and Yi Ding. 3D binder-free Cu_2O@Cu nanoneedle arrays for high-performance asymmetric supercapacitors. *Journal of Materials Chemistry A*, 2(43):18229–18235, sep 2014.

[171] Teresa D. Golden, Mark G. Shumsky, Yanchun Zhou, Rachel A. VanderWerf, Robert A. Van Leeuwen, and Jay A. Switzer. Electrochemical deposition of copper(I) oxide films. *Chemistry of Materials*, 8(10):2499–2504, jan 1996.

[172] S. T. Ren, G. H. Fan, M. L. Liang, Q. Wang, and G. L. Zhao. Electrodeposition of fierarchical ZnO/Cu_2O nanorod films for highly efficient visible-light-driven photocatalytic applications. *Journal of Applied Physics*, 115(6):064301, feb 2014.

[173] O. Messaoudi, H. Makhlouf, A. Souissi, I. Ben assaker, G. Amiri, A. Bardaoui, M. Oueslati, M. Bechelany, and R. Chtourou. Synthesis and characterization of ZnO/Cu_2O core–shell nanowires grown by two-step electrodeposition method. *Applied Surface Science*, 343:148–152, jul 2015.

[174] Xinwei Zou, Huiqing Fan, Yuming Tian, and Shijian Yan. Synthesis of Cu_2O/ZnO hetero-nanorod arrays with enhanced visible light-driven photocatalytic activity. *CrystEngComm*, 16(6):1149–1156, 2014.

[175] Tsutomu Shinagawa, Masanori Onoda, Binti Mohamad Fariza, Junji Sasano, and Masanobu Izaki. Annealing effects and photoelectric properties of single-oriented Cu_2O films electrodeposited on Au(111)/Si(100) substrates. *Journal of Materials Chemistry A*, 1(32):9182–9188, 2013.

[176] Chun-Hong Kuo, Tzu-En Hua, and Michael H. Huang. Au nanocrystal-directed growth of Au-Cu_2O core-shell heterostructures with precise morphological control. *Journal of the American Chemical Society*, 131(49):17871–17878, dec 2009.

[177] Nadav Elad, Giuliano Bellapadrona, Lothar Houben, Irit Sagi, and Michael Elbaum. Detection of isolated protein-bound metal ions by single-particle cryo-STEM. *Proceedings of the National Academy of Sciences*, 114(42):11139–11144, oct 2017.

[178] R.G. Pratt and B.K. Ridley. The capture of thermal electrons by gold centres in n-type germanium at 20°K. *Journal of Physics and Chemistry of Solids*, 26(1):11–20, jan 1965.

[179] Eric W. Bohannan, Mark G. Shumsky, and Jay A. Switzer. Epitaxial electrodeposition of copper(i) oxide on single-crystal gold(100). *Chemistry of Materials*, 11(9):2289–2291, sep 1999.

[180] Hendrik Sträter, Hanna Fedderwitz, Boris Groß, and Niklas Nilius. Growth and surface properties of cuprous oxide films on Au(111). *The Journal of Physical Chemistry C*, 119(11):5975–5981, mar 2015.

[181] Li Zhang, Hao Jing, Geoffrey Boisvert, John Z. He, and Hui Wang. Geometry control and optical tunability of metal–cuprous oxide core–shell nanoparticles. *ACS Nano*, 6(4):3514–3527, apr 2012.

[182] Biao Lu, Aiping Liu, Huaping Wu, Qiuping Shen, Tingyu Zhao, and Jianshan Wang. Hollow Au–Cu_2O core–shell nanoparticles with geometry-dependent optical properties as efficient plasmonic photocatalysts under visible light. *Langmuir*, 32(12):3085–3094, mar 2016.

[183] Meijia Yang, Liping Zhu, Yaguang Li, Ling Cao, and Yanmin Guo. Asymmetric interface band alignments of Cu_2O/ZnO and ZnO/Cu_2O heterojunctions. *Journal of Alloys and Compounds*, 578:143–147, nov 2013.

[184] Abdulaziz Bagabas, Mohamed F. A. Aboud, Reda M. Mohamed, Zeid AL-Othman, Ahmad S. Alshammari, and Emad S. Addurihem. Synthesis, characterization, and cyanide photodegradation over cupric oxide-doped zinc oxide nanoparticles. In *ACS Symposium Series*, pages 327–338. American Chemical Society, jan 2013.

[185] Muhammad Arif Khan, Yussof Wahab, Rosnita Muhammad, Muhammad Tahir, and Samsudi Sakrani. Catalyst-free fabrication of novel ZnO/CuO core-shell nanowires heterojunction: Controlled growth, structural and optoelectronic properties. *Applied Surface Science*, 435:718–732, mar 2018.

[186] Ming-Hui Chiu, Chendong Zhang, Hung-Wei Shiu, Chih-Piao Chuu, Chang-Hsiao Chen, Chih-Yuan S. Chang, Chia-Hao Chen, Mei-Yin Chou, Chih-Kang Shih, and Lain-Jong Li. Determination of band alignment in the single-layer MoS_2/WSe_2 heterojunction. *Nature Communications*, 6(1), jul 2015.

[187] A FRANCIOSI. Heterojunction band offset engineering. *Surface Science Reports*, 25(1-4):1–140, 1996.

[188] Penghui Guo, Jiangang Jiang, Shaohua Shen, and Liejin Guo. ZnS/ZnO heterojunction as photoelectrode: Type II band alignment towards enhanced photoelectrochemical performance. *International Journal of Hydrogen Energy*, 38(29):13097–13103, sep 2013.

[189] Na Zhang, Wei Tang, Ping Wang, Xitian Zhang, and Zhenyu Zhao. In situ enhancement of NBE emission of au–ZnO composite nanowires by SPR. *CrystEngComm*, 15(17):3301, 2013.

[190] Amish G. Joshi, Sonal Sahai, Namita Gandhi, Y. G. Radha Krishna, and D. Haranath. Valence band and core-level analysis of highly luminescent ZnO nanocrystals for designing ultrafast optical sensors. *Applied Physics Letters*, 96(12):123102, mar 2010.

[191] J.P.B. Silva, M. Vorokhta, F. Dvořák, K.C. Sekhar, V. Matolín, J. Agostinho Moreira, M. Pereira, and M.J.M. Gomes. Unraveling the resistive switching effect in $ZnO_{0.5}Ba(Zr_{0.2}Ti_{0.8})O_3$-$0.5(Ba_{0.7}Ca_{0.3})TiO_3$ heterostructures. *Applied Surface Science*, 400:453–460, apr 2017.

[192] Sandra Dias and S. B. Krupanidhi. Determination of band offsets at the Al:ZnO/cu_2sns_3 interface using X-ray photoelectron spectroscopy. *AIP Advances*, 5(4):047137, apr 2015.

[193] M. Akazawa, B. Gao, T. Hashizume, M. Hiroki, S. Yamahata, and N. Shigekawa. Measurement of valence-band offsets of InAlN/GaN heterostructures grown by metal-organic vapor phase epitaxy. *Journal of Applied Physics*, 109(1):013703, jan 2011.

[194] Shoutian Ren, Benyang Wang, Hui Zhang, Peng Ding, and Qiang Wang. Sandwiched ZnO@Au@Cu_2O nanorod films as efficient visible-light-driven plasmonic photocatalysts. *ACS Applied Materials & Interfaces*, 7(7):4066–4074, feb 2015.

[195] Jing-Mei Li, Chun-Wen Tsao, Mei-Jing Fang, Chun-Chi Chen, Chen-Wei Liu, and Yung-Jung Hsu. TiO_2-Au-Cu_2O photocathodes: Au-mediated Z-scheme charge transfer for efficient solar-driven photoelectrochemical reduction. *ACS Applied Nano Materials*, 1(12):6843–6853, nov 2018.

[196] Manuela Jakob, Haim Levanon, and Prashant V. Kamat. Charge distribution between UV-irradiated TiO_2 and gold nanoparticles: Determination of shift in the fermi level. *Nano Letters*, 3(3):353–358, mar 2003.

[197] Vaidyanathan Subramanian, Eduardo E. Wolf, and Prashant V. Kamat. Catalysis with TiO_2/gold nanocomposites. effect of metal particle size on the Fermi level equilibration. *Journal of the American Chemical Society*, 126(15):4943–4950, apr 2004.

[198] Jiangtian Li, Scott K. Cushing, Peng Zheng, Tess Senty, Fanke Meng, Alan D. Bristow, Ayyakkannu Manivannan, and Nianqiang Wu. Solar hydrogen generation by a CdS-Au-TiO_2 sandwich nanorod array enhanced with au nanoparticle as electron relay and plasmonic photosensitizer. *Journal of the American Chemical Society*, 136(23):8438–8449, may 2014.

[199] Akihiro Furube and Shuichi Hashimoto. Insight into plasmonic hot-electron transfer and plasmon molecular drive: new dimensions in energy conversion and nanofabrication. *NPG Asia Materials*, 9(12):e454, dec 2017.

[200] Temer S. Ahmadi, Stephan L. Logunov, and Mostafa A. El-Sayed. Picosecond dynamics of colloidal gold nanoparticles. *The Journal of Physical Chemistry*, 100(20):8053–8056, jan 1996.

[201] Joseph R. Lakowicz, editor. *Principles of Fluorescence Spectroscopy*. Springer US, 2006.

[202] Shayne Sorenson, Eric Driscoll, Shima Haghighat, and Jahan M. Dawlaty. Ultrafast carrier dynamics in hematite films: The role of photoexcited electrons in the transient optical response. *The Journal of Physical Chemistry C*, 118(41):23621–23626, oct 2014.

[203] Qingyong Tian, Weijing Yao, Wei Wu, Jun Liu, Zhaohui Wu, Li Liu, Zhigao Dai, and Changzhong Jiang. Efficient UV–Vis-NIR responsive upconversion and plasmonic-enhanced photocatalyst based on lanthanide-doped $NaYF_4$/SnO_2/Ag. *ACS Sustainable Chemistry & Engineering*, 5(11):10889–10899, oct 2017.

[204] Mahmoud A. Mahmoud, Wei Qian, and Mostafa A. El-Sayed. Following charge separation on the nanoscale in Cu_2O–Au nanoframe hollow nanoparticles. *Nano Letters*, 11(8):3285–3289, aug 2011.

[205] Edward Bormashenko, Yelena Bormashenko, Tamir Stein, Gene Whyman, and Ester Bormashenko. Why do pigeon feathers repel water? hydrophobicity of pennae, Cassie–Baxter wetting hypothesis and Cassie–Wenzel capillarity-induced wetting transition. *Journal of Colloid and Interface Science*, 311(1):212–216, jul 2007.

[206] G. McHale, N. J. Shirtcliffe, and M. I. Newton. Contact-angle hysteresis on super-hydrophobic surfaces. *Langmuir*, 20(23):10146–10149, nov 2004.

[207] Periklis Papadopoulos, Lena Mammen, Xu Deng, Doris Vollmer, and Hans-Jürgen Butt. How superhydrophobicity breaks down. *Proceedings of the National Academy of Sciences*, 110(9):3254–3258, feb 2013.

[208] C.G.L Furmidge. Studies at phase interfaces. i. the sliding of liquid drops on solid surfaces and a theory for spray retention. *Journal of Colloid Science*, 17(4):309–324, apr 1962.

[209] Takashi Kamegawa, Yuki Shimizu, and Hiromi Yamashita. Superhydrophobic surfaces with photocatalytic self-cleaning properties by nanocomposite coating of TiO_2 and polytetrafluoroethylene. *Advanced Materials*, 24(27):3697–3700, jun 2012.

[210] S. Poulston, P. M. Parlett, P. Stone, and M. Bowker. Surface oxidation and reduction of CuO and Cu_2O studied using XPS and XAES. *Surface and Interface Analysis*, 24(12):811–820, nov 1996.

[211] Mohamed M. Ibrahim, Amine Mezni, Hamdy S. El-Sheshtawy, Abeer A. Abu Zaid, Mohammed Alsawat, Nagi El-Shafi, Sameh I. Ahmed, Abdallah A. Shaltout, Mohammed A. Amin, T. Kumeria, and Tariq Altalhi. Direct Z-scheme of Cu_2O/TiO_2 enhanced self-cleaning, antibacterial activity, and UV protection of cotton fiber under sunlight. *Applied Surface Science*, 479:953–962, jun 2019.

[212] Zhigang Zang. Efficiency enhancement of ZnO/Cu_2O solar cells with well oriented and micrometer grain sized Cu_2O films. *Applied Physics Letters*, 112(4):042106, jan 2018.

[213] Jing Li, Hongbo Li, Yan Xue, Hailin Fang, and Wei Wang. Facile electrodeposition of environment-friendly Cu_2O/ZnO heterojunction for robust photoelectrochemical biosensing. *Sensors and Actuators B: Chemical*, 191:619–624, feb 2014.

[214] Sundaram Ganesh Babu, Ramalingam Vinoth, Dharani Praveen Kumar, Muthukonda V. Shankar, Hung-Lung Chou, Kizhanipuram Vinodgopal, and Bernaurdshaw Neppolian. Influence of electron storing, transferring and shuttling assets of reduced graphene oxide at the interfacial copper doped TiO_2 p–n heterojunction for increased hydrogen production. *Nanoscale*, 7(17):7849–7857, 2015.

[215] Sixto Giménez and Juan Bisquert, editors. *Photoelectrochemical Solar Fuel Production*. Springer International Publishing, 2016.

[216] Wolfgang W. Gärtner. Depletion-layer photoeffects in semiconductors. *Physical Review*, 116(1):84–87, oct 1959.

[217] Xinne Zhao, Yang Li, Yuqi Guo, Yajing Chen, Zhiqiang Su, and Panpan Zhang. Coral-like MoS_2/Cu_2O porous nanohybrid with dual-electrocatalyst performances. *Advanced Materials Interfaces*, 3(23):1600658, nov 2016.

[218] Zhihao Yin, Ronglei Fan, Guanping Huang, and Mingrong Shen. 11.5% efficiency of TiO_2 protected and Pt catalyzed n_+np_+-si photocathodes for photoelectrochemical water splitting: Manipulating the pt distribution and pt/si contact. *Chemical Communications*, 54(5):543–546, 2018.

Appendix A

FIGURE REPRINT PERMISSIONS

ACS Publications
Most Trusted. Most Cited. Most Read.

Title: Synthesis and Characterization of ZnO/CuO Vertically Aligned Hierarchical Tree-like Nanostructure

Author: Zhengxin Li, Meng Jia, Baxter Abraham, et al

Publication: Langmuir

Publisher: American Chemical Society

Date: Jan 1, 2018

PERMISSION/LICENSE IS GRANTED FOR YOUR ORDER AT NO CHARGE

This type of permission/license, instead of the standard Terms & Conditions, is sent to you because no fee is being charged for your order. Please note the following:

- Permission is granted for your request in both print and electronic formats, and translations.
- If figures and/or tables were requested, they may be adapted or used in part.
- Please print this page for your records and send a copy of it to your publisher/graduate school.
- Appropriate credit for the requested material should be given as follows: "Reprinted (adapted) with permission from (COMPLETE REFERENCE CITATION). Copyright (YEAR) American Chemical Society." Insert appropriate information in place of the capitalized words.
- One-time permission is granted only for the use specified in your request. No additional uses are granted (such as derivative works or other editions). For any other uses, please submit a new request.

BACK CLOSE WINDOW

Copyright Clearance Center RightsLink®

Account Info Help

Title:	Nanotechnology	Logged in as:
Article ID:	0957-4484	Zhengxin Li
Publication:	Publication1	Account #: 3001442082
Publisher:	CCC Republication	LOGOUT
Date:	Jan 1, 1990	

Order Completed

Thank you for your order.

This Agreement between Zhengxin Li ("You") and IOP Publishing ("IOP Publishing") consists of your order details and the terms and conditions provided by IOP Publishing and Copyright Clearance Center.

License number	Reference confirmation email for license number
License date	Apr, 24 2019
Licensed content publisher	IOP Publishing
Licensed content title	Nanotechnology
Licensed content date	Jan 1, 1990
Type of use	Thesis/Dissertation
Requestor type	Author of requested content
Format	Print, Electronic
Portion	page
Number of pages requested	9
The requesting person/organization	Zhengxin Li
Title or numeric reference of the portion(s)	Chapter 3 EFFICIENT Z-SCHEME CHARGE SEPARATION IN NOVEL VERTICALLY-ALIGNED ZNO/CDSSE NANOTREES
Title of the article or chapter the portion is from	Chapter 3 EFFICIENT Z-SCHEME CHARGE SEPARATION IN NOVEL VERTICALLY-ALIGNED ZNO/CDSSE NANOTREES
Editor of portion(s)	N/A
Author of portion(s)	N/A
Volume of serial or monograph	N/A
Page range of portion	1-9
Publication date of portion	4/24/2019
Rights for	Main product
Duration of use	Life of current and all future editions
Creation of copies for the disabled	no
With minor editing privileges	yes
For distribution to	Worldwide
In the following language(s)	Original language of publication
With incidental promotional use	no
Lifetime unit quantity of new product	Up to 499
Title	FUNCTIONALITY-DRIVEN ARCHITECTURE OF AND PHOTOVOLTAIC CONVERSION IN HIERARCHICAL TREE-LIKE SEMICONDUCTORS

Copyright Clearance Center

Note: Copyright.com supplies permissions but not the copyrighted content itself.

1 PAYMENT 2 REVIEW 3 CONFIRMATION

Step 3: Order Confirmation

Thank you for your order! A confirmation for your order will be sent to your account email address. If you have questions about your order, you can call us 24 hrs/day, M-F at +1.855.239.3415 Toll Free, or write to us at info@copyright.com. This is not an invoice.

Confirmation Number: 11810679
Order Date: 04/27/2019

If you paid by credit card, your order will be finalized and your card will be charged within 24 hours. If you choose to be invoiced, you can change or cancel your order until the invoice is generated.

Payment Information

Zhengxin Li
lizx@udel.edu
+1 (302) 559-4253
Payment Method: n/a

Order Details

Philosophical transactions. Series A, Mathematical, physical, and engineering sciences

Order detail ID:	71886790
Order License Id:	4577351088027
ISSN:	1364-503X
Publication Type:	Journal
Volume:	
Issue:	
Start page:	
Publisher:	ROYAL SOCIETY
Author/Editor:	Royal Society (Great Britain)

Permission Status: Granted

Permission type:	Republish or display content
Type of use:	Republish in a thesis/dissertation
Requestor type	Academic institution
Format	Print, Electronic
Portion	chart/graph/table/figure
Number of charts/graphs/tables/figures	1
The requesting person/organization	Zhengxin Li/University of Delaware
Title or numeric reference of the portion(s)	Figure 1.1: SEM images of lotus leaf surface(a) and a water droplet sitting on a lotus leaf(b).
Title of the article or chapter the portion is from	Biomimetics: lessons from nature – an overview

Copyright Clearance Center RightsLink®

Home Account Info Help

ACS Publications Most Trusted. Most Cited. Most Read.

Title: Cassie–Baxter and Wenzel States on a Nanostructured Surface: Phase Diagram, Metastabilities, and Transition Mechanism by Atomistic Free Energy Calculations

Author: Alberto Giacomello, Simone Meloni, Mauro Chinappi, et al

Publication: Langmuir

Publisher: American Chemical Society

Date: Jul 1, 2012

Logged in as:
Zhengxin Li
Account #:
3001442082

LOGOUT

PERMISSION/LICENSE IS GRANTED FOR YOUR ORDER AT NO CHARGE

This type of permission/license, instead of the standard Terms & Conditions, is sent to you because no fee is being charged for your order. Please note the following:

- Permission is granted for your request in both print and electronic formats, and translations.
- If figures and/or tables were requested, they may be adapted or used in part.
- Please print this page for your records and send a copy of it to your publisher/graduate school.
- Appropriate credit for the requested material should be given as follows: "Reprinted (adapted) with permission from (COMPLETE REFERENCE CITATION). Copyright (YEAR) American Chemical Society." Insert appropriate information in place of the capitalized words.
- One-time permission is granted only for the use specified in your request. No additional uses are granted (such as derivative works or other editions). For any other uses, please submit a new request.

If credit is given to another source for the material you requested, permission must be obtained from that source.

BACK CLOSE WINDOW

Appendix B

LIST OF PUBLICATIONS

1. Mahsa Konh, Chuan He, Zhengxin Li, Shi Bai, Elena Galoppini, Lars Gundlach, Andrew V Teplyakov. Comparison of ZnO surface modification with gas-phase propiolic acid at high and medium vacuum conditions.*Journal of Vacuum Science & Technology A: Vacuum, Surfaces, and Films*, 36(4):041404, 2018.

2. Chuan He, Baxter Abraham, Hao Fan, Ryan Harmer, Zhengxin Li, Elena Galoppini, Lars Gundlach, Andrew V Teplyakov. Morphology-Preserving Sensitization of ZnO Nanorod Surfaces via Click-Chemistry. *The Journal of Physical Chemistry Letters*, 9(4):768-772, 2018.

3. Zhengxin Li, Meng Jia, Baxter Abraham, Jolie C Blake, Daniel Bodine, John T Newberg, Lars Gundlach. Synthesis and Characterization of ZnO/CuO Vertically Aligned Hierarchical Tree-like Nanostructure. *Langmuir*, 34(3):961-969, 2018.

4. Zhengxin Li, Jesus Nieto-Pescador, Alexander J Carson, Jolie C Blake, Lars Gundlach. Efficient Z-scheme charge separation in novel vertically aligned ZnO/CdSSe nanotrees. *Nanotechnology*, 27(13):135401, 2016.

5. Jolie Blake, Jesus Nieto-Pescador, Zhengxin Li, Lars Gundlach. Ultraviolet Femtosecond Kerr-gated Wide-field Fluorescence Microscopy. *Optics Letters*, 2016.

6. Zhengxin Li, Jesus Nieto-Pescador, Alexander J Carson, Jolie C Blake, Lars Gundlach. Synthesis of Hierarchical ZnO/CdSSe Heterostructure Nanotrees. *Journal of Visualized Experiments*, 117:e54675, 2016.

7. Jolie Blake, Jesus Nieto-Pescador, Zhengxin Li, Lars Gundlach. Ultrafast dynamics of single ZnO nanowires using ultraviolet femtosecond Kerr-gated wide-field fluorescence microscopy. *Ultrafast Nonlinear Imaging and Spectroscopy IV*, 9956, 99560U, 2016.

8. Li, Zhengxin; Liu, Meichuan; Fan, Lifang; Ke, Hongyang; Luo, Caifang; Zhao, Guohua; A highly sensitive and wide-ranged electrochemical zinc (II) aptasensor fabricated on core–shell SiO_2-Pt@meso-SiO_2. *Biosensors and Bioelectronics*, 52: 293-297, 2014.

9. Hongyang Ke, Meichuan Liu, Lu Zhuang, Zhengxin Li, Lifang Fan, Guohua Zhao. A femtomolar level 17β-estradiol electrochemical aptasensor constructed on hierarchical dendritic gold modified boron-doped diamond electrode. *Electrochimica Acta*, 137: 146-153, 2014.

10. Lifang Fan, Guohua Zhao, Huijie Shi, Meichuan Liu, Zhengxin Li. A highly selective electrochemical impedance spectroscopy-based aptasensor for sensitive detection of acetamiprid, *Biosensors and Bioelectronics*, 43:12-18, 2013.